Benjamin Stickler, BSc

Theoretical investigation of the competition between electron-hole generation and recombination effects in organic and organic-inorganic solar cells

MASTER THESIS

Zur Erlangung des akademischen Grades
Master of Science der Studienrichtung Technische Chemie
erreicht an der
Technischen Universität Graz

Betreuer:
Univ.-Doz. Dr. Gregor Trimmel
Institut für Chemische Technologie von Materialien

Ao. Univ.-Prof. Dr. Ferdinand Schürrer
Dr. Karin Zojer
Institut für Theoretische Physik - Computational Physics

2009

Deutsche Fassung:
Beschluss der Curricula-Kommission für Bachelor-, Master- und Diplomstudien vom 10.11.2008
Genehmigung des Senates am 1.12.2008

EIDESSTATTLICHE ERKLÄRUNG

Ich erkläre an Eides statt, dass ich die vorliegende Arbeit selbstständig verfasst, andere als die angegebenen Quellen/Hilfsmittel nicht benutzt, und die den benutzten Quellen wörtlich und inhaltlich entnommene Stellen als solche kenntlich gemacht habe.

Graz, am …… ……..
(Unterschrift)

Englische Fassung:

STATUTORY DECLARATION

I declare that I have authored this thesis independently, that I have not used other than the declared sources / resources, and that I have explicitly marked all material which has been quoted either literally or by content from the used sources.

…… ……..
date (signature)

Abstract

Generation and recombination effects profoundly influence the performance of organic-organic and organic-inorganic photovoltaic devices. The aim of this thesis is to obtain a better understanding of these processes and their effects on the shape of the current-voltage characteristic. Therefore, a two-dimensional approach via drift-diffusion equations for electrons, holes and excitons has been chosen to model solar cells. The corresponding equations, i.e. the Poisson equation and the current density equations combined with the continuity equation, are solved self-consistently on a two-dimensional grid. The influence of field-assisted particle generation, field-dependent mobilities and bimolecular recombination in terms of a Langevin type form is studied. Morphology effects are primarily excluded by assuming a flat interface between the donor and the acceptor regions. The calculated electrostatic potential, electric field strength, particle densities, generation and recombination profiles as well as current-voltage characteristics finally allow interesting interpretations of the basic processes taking place within the cell.

Zusammenfassung

Das Ziel dieser Arbeit ist die Entwicklung eines Modells zur Simulation von organisch-organischen und organisch-anorganischen Solarzellen um in weiterer Folge Einfluss und Auswirkungen von Ladungsträger Generations- und Rekombinationseffekten zu verstehen. Hierzu werden die Poisson Gleichung und die Kontinuitätsgleichungen für Elektronen, Löcher und Excitonen auf einem zweidimensionalen Gitter selbstkonsistent gelöst. Weiters werden feldabhängige Mobilitäten und Exciton-Dissoziationsraten, sowie bimolekulare Rekombinationseffekte nach Langevin und Koster berücksichtigt. Die dadurch erhaltenen Ladungsträgerdichten sowie Potential-, Feld-, Generations- und Rekombinationsprofile erlauben eine eingehende Untersuchung der Auswirkungen dieser Größen auf die simulierten Strom-Spannungs-Kennlinien.

Sol omnibus lucet.

(The sun shines for everyone)

Titus Petronius

Contents

List of Figures

1 Introduction

I would like to begin this introductory chapter with three independent statements:

- Mankind is in need of alternative energy sources.
- Renewable energy sources are preferable.
- The earth receives about 1367 Wm^{-2} from the sun.

What could sound more attractive than to make use of this provided energy?

Solar technology is one of the most promising approaches on the route to alternative and renewable energy sources and, moreover, takes advantage of the power of the sun literally given to us. The big disadvantage of classical photovoltaic devices, i.e. mostly silicon based solar cells, is the high production cost. Organic or organic-inorganic solar cells address this disadvantage exactly by using alternative materials, i.e. thin plastic substrates, which lowers the production cost enormously. But in contrast to classical solar cells, efficiencies up to 20 % have not been reached yet, which is the biggest disadvantage of organic solar cells. The maximum efficiency reported is about 6 %, [1].

The aim of this thesis is to contribute to this important and rapidly proceeding development by a theoretical approach. The effects of charge carrier generation and recombination are modeled and their influence on the shape of the I-V characteristic is studied in detail. The main processes, i.e. exciton generation by an incoming photon flux, exciton diffusion, exciton recombination, field-dependent exciton dissociation and exciton separation at the organic-inorganic interface and the further diffusion and drift processes of charge carriers, including recombination effects are considered in a representative unit of the photovoltaic device. This is done by solving the Poisson equation and the continuity equations on a two-dimensional mesh under periodic- and Dirichlet boundary conditions. The equations are discretized with a finite difference approach, using an implicit time step method for the temporal evolution of the particle densities. Varying the input conditions gives us the possibility of simulating the whole I-V curve as well as particle densities, electric field and potential profile, generation and recombination profiles at each point of the I-V characteristic. Therefore, a basic understanding

of the interplay of the different processes taking place can be obtained. It must be emphasized that primarily a planar interface was considered to exclude any kind of morphological effects. A detailed study of morphological effects and their influence on the characteristics can be found in [2].

The thesis consists of four main chapters. We start by introducing the basic properties and facts about organic photovoltaics. The following two chapters deal with the theoretical aspects relevant for modeling a device and the numerical implementation of these equations. Finally, simulation results are shown and discussed in detail.

2 Nanoparticle - polymer solar cells

This introductory chapter is divided into three parts: first, general aspects concerning solar cells, especially nanoparticle - polymer solar cells, second, the origin of solar energy and the form of the solar spectrum relevant at our particular latitude, and, third, basic concepts of conjugated polymers. The section gives only a short overview of the fundamental processes and concepts. For further and more detailed information the reader is referred to several publications listed in the bibliography.

2.1 General aspects

In the first section we will give in three subsections, a short overview of general concepts of solar cells, their operating mode including characteristic parameters, and nanoparticle - polymer solar cells in particular.

2.1.1 Solar cells

A solar cell or photovoltaic cell is a device which converts light directly into electricity. The cell consists of two electrodes separated by two semiconducting layers, an organic and an inorganic region. In this particular case it is a polymer and a nanoparticle layer (see Fig. 2.1).

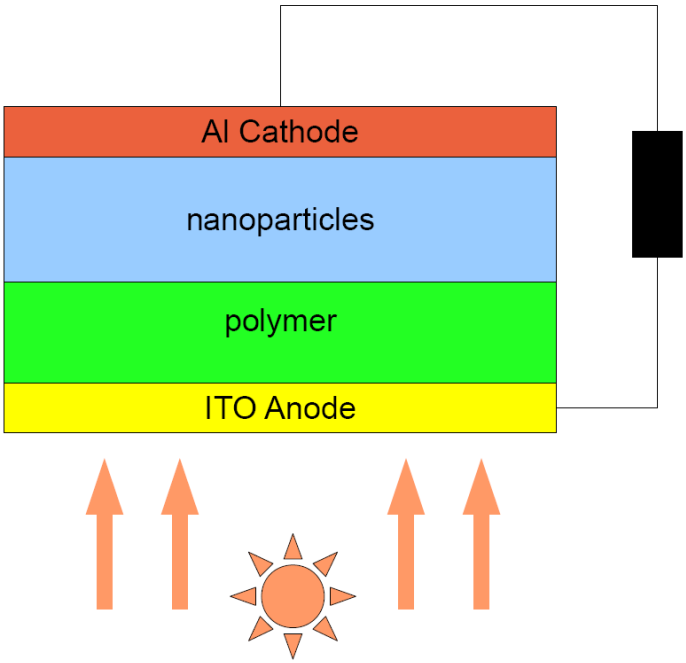

Figure 2.1: Schematic configuration of a solar cell consisting of a polymer and a nanoparticle layer.

Basically, incoming light (photons) provides the energy to generate an exciton, an electron-hole pair, which can in the further process dissociate into a free electron and hole. These charge carriers are now able to propagate to the corresponding electrode, driven by diffusion and the electric field.

Thus the basic processes are [3]:

- Exciton generation,
- Exciton dissociation - charge carrier generation,
- Transport of charge carriers to the corresponding electrode.

Exciton generation, i.e. the energy conversion from light to an excited state, is only possible if the energy of the photon is greater than or equal to the binding energy of an exciton, which is lower than the bandgap between HOMO, the highest occupied molecular orbital, and LUMO, the lowest unoccupied molecular orbital, of the semiconducting material:

$$E_b^x \leq h\nu < \Delta E = |E_{HOMO} - E_{LUMO}|. \tag{2.1}$$

If the energy is lower, the photons just pass through the material. If it is higher, the photon is absorbed and excitation to a higher state occurs. In the further process this

state relaxes thermally to the S_1 state, which relaxes to the excitonic state (Fig. 2.2). Using semiconducting polymers limits the absorption to about 30 % [3]. A way to improve light absorption is the use of low band gap polymers or using a second material with a lower bandgap, i.e. inorganic nanoparticles [3].

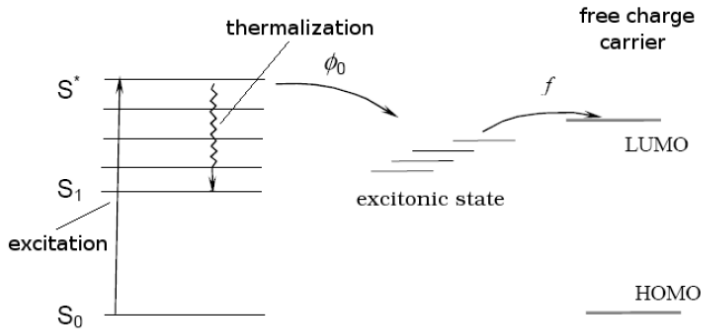

Figure 2.2: Schematic illustration of the photon absorption and exciton generation process. An absorbed photon excites the electron from the S_0 to the S^* states, from where it relaxes to the first excited state S_1. It generates an exciton with the rate ϕ_0, which can in the further process dissociate into free charge carriers with the rate f.

The generated exciton can dissociate into free charge carriers if the electron-hole binding energy is provided. In inorganic semiconducting materials this binding energy is very low and in the range of the thermal energy, about 25 meV. Thus, in inorganic solar cells exciton dissociation is driven thermodynamically and occurs immediately. In organic materials, the binding energy is very large ($0.3 - 0.5$ eV) [4] and the dissociation process is not fully understood. There are approaches to regard the dissociation effect as strongly field-dependent [5, 6, 7] but still no evidence has been found, verifying this assumption. Another assumption is that exciton separation takes place at the intrinsic interface between the two different materials used and, if it exists, within an inorganic material.

However, in both cases exciton diffusion plays a crucial role in the performance of organic photovoltaics. Besides separation into charge carriers, excitons may relax to the groundstate or recombine to triplet excitons (Fig. 2.3), because they have a finite lifetime (about 1 ms, [4], [5]).

Separated charge carriers, i.e. electrons and holes, moving to the electrodes can also recombine and decrease the efficiency of the device. This bimolecular recombination rate is highly concentration- and mobility-dependent. Because of the mobilities being

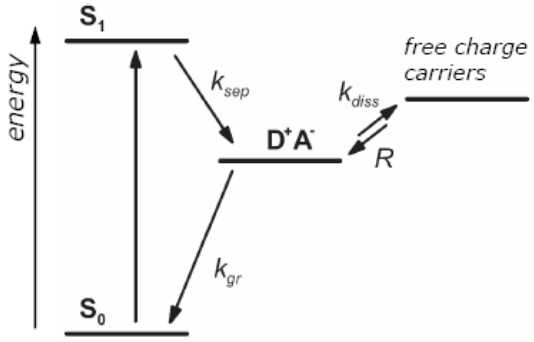

Figure 2.3: Energy scheme of exciton generation and recombination and accordingly charge carrier generation and recombination

field-dependent, the recombination rate also depends on the locally occurring electric field strengths in the cell. The interplay of these effects, finally, profoundly influences the performance of the device.

Furthermore, generated charge carriers move to the corresponding electrode under the influence of the transport levels of the material, i.e. HOMO and LUMO levels, Fig. 2.4.

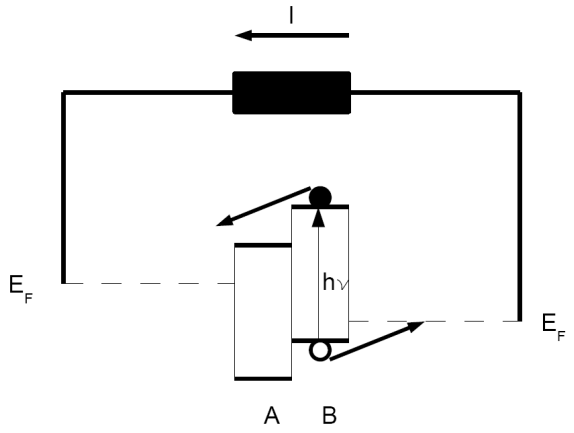

Figure 2.4: Bandgap profile of a typical solar cell based on the usage of two different materials, A and B. E_F indicates the Fermi-levels of the electrodes. $\circ \ldots h^+$, $\bullet \ldots e^-$

2.1.2 Operating mode - Characteristic parameters

The basic regions for the operation of a solar cell can be regarded as reverse bias (negative regime) and forward bias (positive regime). The characteristic points of a solar cell are the short circuit condition and open circuit condition, also called flat-band condition [3],

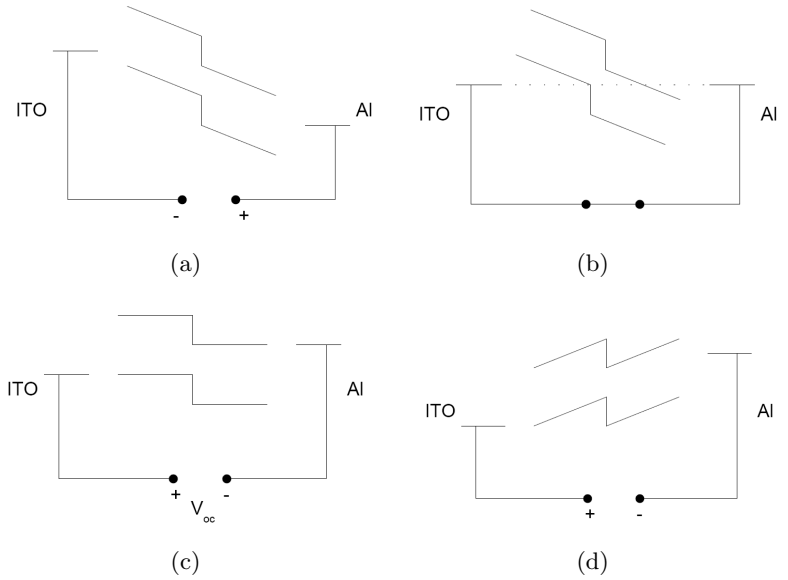

Figure 2.5: Different operation regimes of a solar cell consisting of two materials (V_a is the applied voltage): (a) reverse bias, $V_a < V_{bi}$, (b) short circuit condition, $V_a = 0$ V, (c) open circuit condition, $V_a = V_{bi}$, (d) forward bias, $V_a > V_{bi}$.

Fig. 2.5. In the operating mode of the solar cell the gained power $P = VI$ (negative) reaches a maximum at the maximum power point, *mpp*.

At this point the voltage is positive (Fig. 2.6), but electrons still flow to the opposite electrode because the energy of the electrons is not sufficient to cross the implemented bandgap between organic and inorganic layer, resulting in negative, thus gained power (Fig. 2.6, 2.5).

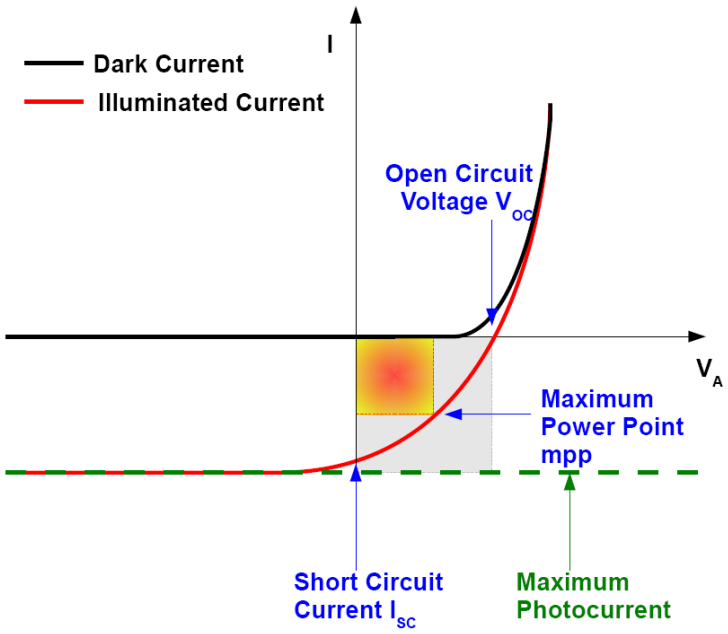

Figure 2.6: Idealized I/V curve of a solar cell with operating modes. Units are left out because the range depends on the particular materials used.

In inorganic solar cells, the built-in voltage, V_{bi}, of a solar cell is described as an upper limit to the open circuit voltage, V_{oc}. When considering ohmic contacts, it is identical to the bandgap between the two materials used (for illustration see Fig. 4.2):

$$V_{bi} \approx \Delta E_{gap}. \tag{2.2}$$

Also in organic solar cells, the built-in voltage is related to the open circuit voltage, but in a more sophisticated way. One approach was already published by Gregg [8]. The exact behavior of the open circuit voltage and the relation to the built-in voltage will be investigated in Sec. 5.1.2.

Nevertheless, narrowing the bandgap yields a smaller V_{bi}, thus smaller V_{oc} and thus limits the possible power gain. The open-circuit voltage V_{oc} is the potential necessary to compensate the internal load. The short-circuit current I_{sc} is the external measured current if no external voltage is applied (Fig.s 2.6, 2.5). Other important parameters used to describe solar cells are the fill factor, given by

$$FF = \frac{P_{max}}{I_{sc}V_{oc}} = \frac{\min(VI)}{I_{sc}V_{oc}}, \tag{2.3}$$

and the energy conversion efficiency, given by

$$\eta = \frac{P_m}{EA}, \tag{2.4}$$

where E denotes the input light irradiance under standard test conditions (STC) and A the surface area. Using this definition, the fill factor can be expressed as

$$FF = \frac{AE\eta}{I_{sc}V_{oc}}. \tag{2.5}$$

2.1.3 Organic and organic-inorganic solar cells

The most important difference between inorganic photovoltaic devices and solar cells based on organic materials is the photoconversion mechanism, i.e. the charge carrier generation mechanism. In organic photovoltaic devices a strongly bound exciton is formed which does not dissociate thermodynamically like in inorganic devices.

Organic or organic-inorganic solar cells consist of two different components which are sandwiched between two metal electrodes. One of these electrodes must be transparent, usually ITO (Indium Tin Oxide) [3, 9].

The most important types of these solar cells are characterised below according to [9].

- Organic solar cells are a mixture of two organic components on a nano-scopic scale. Such bulk heterojunction cells consist of a polymer/polymer blend or a polymer/organic molecule blend.
- Organic-inorganic solar cells are obtained if one phase of an organic solar cell is replaced by inorganic nanoparticles.
- Dye-Sensitized solar cells (DSSCs) (Grätzel cells) are based on a network of oxide particles (usually TiO_2). These particles are covered by an organic dye (absorber); the whole structure is immersed in a liquid electrolyte, which acts as hole conductor.
- Hybrid solar cells are obtained if the liquid electrolyte of a DSSC is replaced by an organic solid hole conductor like a polymer.
- Dye sensitized heterojunctions (DSHs) result from the replacement of the liquid electrolyte of DSSCs with an inorganic material.
- Extremely thin absorber cells (ETAs): In these cells the organic dye is replaced by an inorganic solid state absorber.

The scientific breakthrough of organic solar cells occurred in 1986, when Tang [10] reported the achievement of efficiencies of about 1 %, after the investigation started earlier with rather low efficiencies, using anthracene crystals as organic material [3, 11]. The most studied system nowadays is the P3HT / PCBM system, for which efficiencies even up to 6 % have been reported recently, e.g. in [1].

2.2 Solar energy

The radiative zone of the sun, i.e. the photosphere, consists mainly of hydrogen and helium and is only 300 − 400 km thick. An emitted photon, can be re-absorbed and re-emitted and needs about 10.000 - 170.000 years to reach the surface of the sun and leave the sun. After that it takes about 8 minutes to travel to earth.

The conversion from mass to energy is a very complicated process, but basically two protons collide, fuse and form a Helium core. The mass difference is converted to energy according to Einstein's relation:

$$E = mc^2. \tag{2.6}$$

In the core of the sun about 564 10^6 t hydrogen fuse to 560 10^6 t helium per second by a temperature of about 15.7 10^6 K, which is basically too small for proton fusion. The main effect regarded as responsible for fusion is quantum mechanical tunneling. About 3.8 10^{26} W are released from the sun per second, from which 1376 Wm^{-2} reach the atmosphere of the earth (solar constant), mainly consisting of IR (44 %), visible light (52 %), UV-A (3.6 %) and UV-B (0.4 %). Further, the energy reaching the surface of the earth is lowered by penetrating the atmosphere, containing larger molecules and clouds, and by the impact angle (Fig. 2.7). Atmospheric scattering and light absorption of clouds are the main reasons for lowered intensity. Therefore, a reduced sun spectrum has to be considered, *air mass 1.5* (AM 1.5) accounting for an angle of about 48° and absorption due to scattering in the atmosphere (Fig. 2.8, [12]).

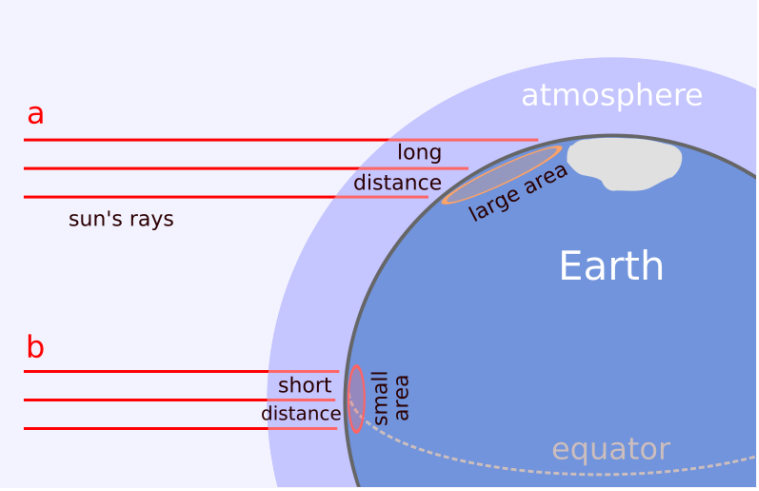

Figure 2.7: Decrease of solar power by penetration of the atmosphere of the earth at two different latitudes, (a) and (b), [13].

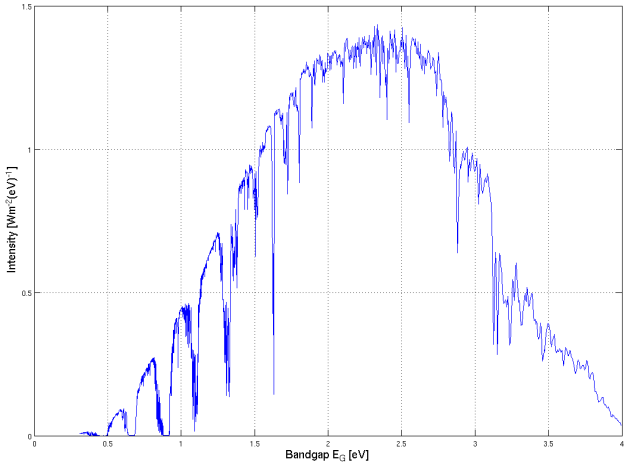

Figure 2.8: Solar spectral irradiance at air mass 1.5 [14].

2.3 Conjugated Polymers

In this section I will discuss briefly the main properties and classes of conjugated polymers. Furthermore, the theoretical approaches to describe charge transport within this type of polymers are introduced.

2.3.1 Basics

Conductivity is an effect based on freely movable charges or charge defects and especially in conjugated polymers it is referred to an extended π-electron system [3]. In classical organic polymers, i.e. organic molecules linked to a chain by σ bonds without π orbital delocalization, the property of freely movable charges is not fulfilled. In conjugated polymers the backbone molecules have alternating π and σ bonds, like polyacetylene (Fig. 2.3.1), leading to a total conjugation of the system and thus to intrinsic conductivity. In this particular polymer the conductivity is caused by sp^2 hybridization of the atoms, yielding free electrons in π orbitals. In contrast to polyacetylene there is no conductivity in polyethylene, because the atoms are sp^3 hybridized and there are no π bonds left. Polyphenylene could also be conductive, because of conjugated phenylene rings, systems consisting of 6 linked π orbitals. But this is only partially true because, if in the polymerchain two phenylene rings lie perpendicular to each other, i.e. the relative orientation of the π orbitals is perpendicular, the overlap is zero. Best conductivity is achieved if the orbitals are orientated perfectly parallel. Thus, in the polyphenylene case, it would be necessary to additionally link, and therefore fix the single parts of the polymer, which makes synthesis more difficult. These considerations are the reason for the use of polyfluorenes and ladder-type polymers [15, 16].

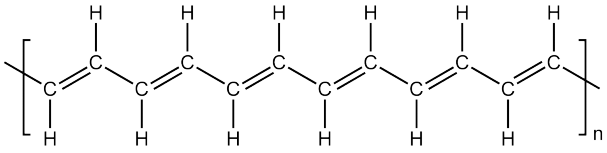

Figure 2.9: Polyacetylene. The bonds between two units are single σ bonds, while in the unit molecule it is a double bond, resulting in an alternating single-double-bonded system.

One important class of conjugated polymers used today for organic photovoltaics are based on thiophene rings, where sulfur provides additional electrons to the π system. These systems are believed to possess a band-like electronic structure. It is characterized by the LUMO level for the electron conduction band, which is in our case the empty π^* band, and HOMO level for the electronic valence band, the filled π band. By energy supply, e.g. photoinduction, an electron from the π band can be excited to the π^* band without breaking the chain, because it is held together by a σ bond. The HOMO and LUMO levels are very sensitive to the structure of the molecule, thus they are subjected to energetic disorder [5]. Therefore, in many cases the density of states, approximated with a Gaussian distribution, is used instead of absolute HOMO-LUMO levels.

The important factor leading to high conductivity σ is the charge carrier mobility μ. These two quantities are linked via the charge carrier concentration n [17]:

$$\sigma \propto n\mu. \tag{2.7}$$

Because of the large band gaps in organic polymers, n is very small, thus also the conductivity in the neutral state of polymers. But it can be made conductive by oxidation (p-doping) or reduction (n-doping) by chemical- or electrochemical means, which generates free charge carriers as described earlier in this section. This was demonstrated in 1977 by Shirakawa, MacDiarmid and Heeger [18] and in 2000 awarded with the Nobel prize.

Another very important aspect is the photoinduced electron transfer from a conjugated polymer onto an acceptor, called *"photodoping"* [19], which leads to photoconductivity.

2.3.2 Classes of materials

There are various classes of well-investigated conjugated polymers so far, including poly(acetylene)s, poly(thiophen)s, poly(pyrrol)s, polyanilines, poly(p-phenylene vinylene)s and poly(p-phenylene sulfide)s [20], Fig. 2.10).

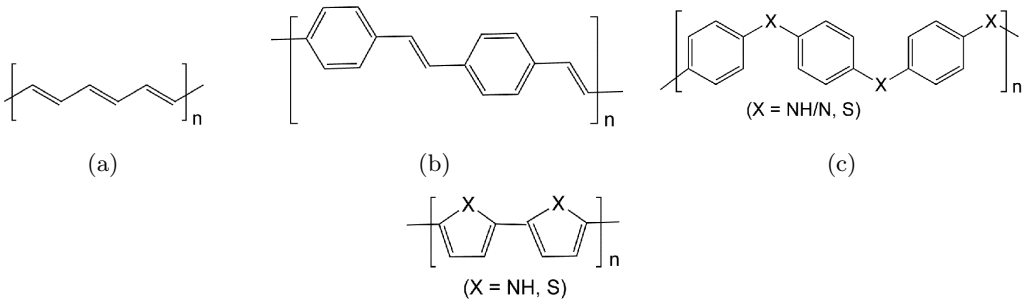

(a) (b) (c) (d)

Figure 2.10: Structures of various conductive polymers; polyacetylene (a), polyphenylenevinylene (b), polyaniline (X=NH/N) and polyphenylene sulfide (X=S) (c), polythiophene (X=S) and polypyrrole (X=N) (d)

Typical materials for organic solar cells or organic field effect transistors are poly(3-alkyltiophenes), like P3HT or P3EBT (see 2.3.3). The motivation for using this type of molecules can be found, on the one hand, in their property of generating excited states under illumination in a region useful for solar technology, and on the other hand, in their conductive behavior. For instance in [21]:

"We shall consider a molecule consisting of two parts, a long chain called the "spine" in which electrons fill the various states and may or may not form a conducting system; and secondly, a series of arms or side chains attached to the spine [...]. We will show that by appropriate choice of the molecules which constitute the side chains, the virtual oscillation of charge in these side chains can provide an interaction between the electrons moving in the spine. This can be made a sufficiently attractive interaction so that the superconducting state results."
Naturally the superconducting state is never reached in organic solar cells, because of the high temperature in the device. Nevertheless, this citation indicates that conductivity can be tuned by choosing appropriate side chains.

2.3.3 Materials considered in this thesis

The three conjugated polymers considered in this thesis are P3HT (Poly(3-hexyltiophene-2,5-diyl)), P3EBT (Poly[3-(ethyl-4-butanoate)thiophene-2,5-diyl) and F8T2 (Poly[9,9-dioctylfluorenyl-2,7-diyl]-co-(bithiophene)]), (Fig. 2.11). As inorganic layer CIS ($CuInS_2$) is used. The motivation for using these materials can be found in the fact that they are used for organic solar cell assembly in the group of Gregor Trimmel [22]. The HOMO-LUMO levels of these materials used for the simulation are shown in table 2.1, as determined by [22]. The mobilities are assumed to be 10^{-8} $mV^{-1}s^{-1}$ for the polymers as well for electrons and holes, and 10^{-6} $mV^{-1}s^{-1}$ for CIS, also for electrons and holes.

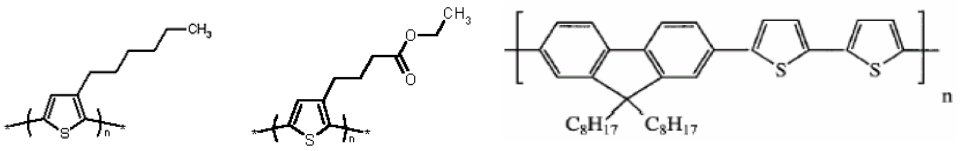

(a) P3HT (b) P3EBT (c) F8T2

Figure 2.11: The three used polymers.

Table 2.1: HOMO LUMO levels of the materials used.

	HOMO / eV	LUMO / eV
P3HT	5.2	3.5
P3EBT	5.6	3.7
F8T2	5.4	2.5
CIS	5.6	4.1

2.3.4 Transport of charge carriers in conjugated polymers

The description of transport of particles in organic polymers is quite similar to the description in inorganic crystals which is based on the random walk diffusion equation. If the particles are charge carriers, a field-dependent drift has to be considered additionally, which resembles a biased random walk. The resulting balance equation, called the Fokker-Planck equation (general form) reads

$$\frac{\partial f(x,t)}{\partial t} = -\frac{\partial}{\partial x}\left[D_1(x,t)f(x,t)\right] + \frac{\partial^2}{\partial x^2}\left[D_2(x,t)f(x,t)\right], \tag{2.8}$$

where $D_1(x,t)$ denotes the drift and $D_2(x,t)$ the diffusion tensor, as a function of space, $x \in \mathbb{R}$, and time, $t \in \mathbb{R}^+$. This equation was first used to describe the Brownian motion of a particle on a liquid surface [23]. The problem of this description is that it is based on a random walk-like model, which implies that the probability of moving in a random direction is always the same, independent of transport level effects or the particular chain-like morphology of polymers.

However, charge transport mechanism in organic polymers is not yet fully understood. As mentioned earlier, the HOMO and LUMO levels are subject to high disorder, mainly because of the weak van der Waals bonding between the molecules, resulting in very narrow valence and conduction bands with bandwidths of about 10 meV [17]. Further it was discovered that mobility of charge carriers in a polymer rises with rising temperature [24]. In contrast to inorganic crystalline materials, in which the mobility decreases with increasing temperature. Because charge carriers have to overcome energy barriers to propagate, this process is called *hopping transport*. As shown by Bässler, this mechanism leads to field-dependent mobilities of the Poole-Frenkel form [25]

$$\mu(\mathbf{E}) = \mu_0 \exp(\gamma\sqrt{|\mathbf{E}|}), \tag{2.9}$$

where γ denotes a constant, $\mathbf{E}$ the electric field and μ_0 the charge carrier mobility at zero field. There are also several alternative models for describing charge transport in organic polymers. One of these is the so-called polaron transport. A polaron is a free particle deforming the atoms in its vicinity and thus lowering the energy of the system. This stabilization results in a potential well localizing the particle, which carries the atomic deformation with it as it moves through the material. The resulting charge carrier mobility is not only field- but also temperature-dependent. It is given by [26]

$$\mu = \mu_0 \frac{2k_BT}{\alpha|\mathbf{E}|} \exp\Big[-\frac{1}{4k_BT}\left(E_r + \frac{(\alpha|\mathbf{E}|)^2}{E_r}\right)\Big] \sinh\left(\frac{\alpha|\mathbf{E}|}{2k_BT}\right), \tag{2.10}$$

where α denotes a constant, E_r the intramolecular reorganization energy of the system, T the temperature and k_B Boltzmann's constant.

3 Device Modeling

In this section all equations necessary for the simulation of the device are introduced. In the first subsection we will start with the Poisson equation, which is used to determine the electrostatic potential in order to evaluate the electric field strength. The time-evolution of charge carrier density is described by the continuity equation combined with the equation for the drift-diffusion current. The last one consists of a diffusional and a drift term, which is a function of the electric field. Before summarizing these equations, the generation and recombination terms for particles are discussed. A complete numerical scheme for solving these equations is given in Sec. 4.

3.1 Poisson equation

The Poisson equation is a second order partial differential equation in space providing a relation between a given charge distribution $\rho(\mathbf{r}) = q[p(\mathbf{r}) - n(\mathbf{r})]$, with the elementary charge $q = 1.602\ 10^{-19}$C, the hole and electron density, $p(\mathbf{r})$ and $n(\mathbf{r})$, respectively, and the potential $\psi(\mathbf{r})$ as a function of space for a given permittivity $\epsilon(\mathbf{r}) = \epsilon_0\epsilon_r(\mathbf{r})$.

$$\nabla \cdot [\epsilon(\mathbf{r})\nabla\psi(\mathbf{r})] = -\rho(\mathbf{r}), \tag{3.1}$$

with $\mathbf{r} \in \mathbb{R}^3$.

3.2 Diffusion equation

The diffusion equation can be derived in numerous ways (for instance see [27]). Here the derivation based on the random walk is preferred [23].

We consider a particle moving in one spatial dimension. Let us assume that at time $t \in \mathbb{R}$ the particle is located at position $x \in \mathbb{R}$. It moves in the next time step, Δt, over a distance Δx with probability p in one direction and with probability q in the opposite direction. It, therefore, remains at x with probability $r = 1 - p - q$. These probabilities are independent of the actual position of the particle and of the time. Hence, it is a Markovian process. The probability $P(x, t|p, q, r, \mathcal{B})$ of finding the particle at time t at

position x, where $\mathcal{B}$ is the condition complex, can be expressed by

$$\begin{aligned} P(x,t|p,q,r,\mathcal{B}) &= P(x,t-\Delta t|p,q,r,\mathcal{B})r + P(x-\Delta x,t-\Delta t|p,q,r,\mathcal{B})p \\ &\quad + P(x+\Delta x,t-\Delta t|p,q,r,\mathcal{B})q \qquad (3.2) \\ &= P(x,t-\Delta t|p,q,r,\mathcal{B})(1-p-q) + P(x-\Delta x,t-\Delta t|p,q,r,\mathcal{B})p \\ &\quad + P(x+\Delta x,t-\Delta t|p,q,r,\mathcal{B})q, \qquad (3.3) \end{aligned}$$

i.e. the probability of being at point x at time t is the same as the probability of being at time $t-\Delta t$ at point x and remaining there, or being at point $x-\Delta x$ and moving one step to the right or being at $x+\Delta x$ and moving one step to the left. Expanding now each term in a Taylor series up to order $\mathcal{O}(\Delta x^2)$ and $\mathcal{O}(\Delta t)$ respectively, and simplifying the notation by $P(x,t) := P(x,t|p,q,r,\mathcal{B})$ yields

$$\begin{aligned} P(x,t) &= (1-p-q)\Big[P(x,t) - \Delta t\frac{\partial P(x,t)}{\partial t}\Big] \\ &\quad + p\Big[P(x,t) - \Delta t\frac{\partial P(x,t)}{\partial t} - \Delta x\frac{\partial P(x,t)}{\partial x} + \frac{1}{2}\Delta x^2\frac{\partial^2 P(x,t)}{\partial x^2}\Big] \\ &\quad + q\Big[P(x,t) - \Delta t\frac{\partial P(x,t)}{\partial t} + \Delta x\frac{\partial P(x,t)}{\partial x} + \frac{1}{2}\Delta x^2\frac{\partial^2 P(x,t)}{\partial x^2}\Big]. \qquad (3.4) \end{aligned}$$

From Eq. (3.4) we obtain

$$\frac{\partial P(x,t)}{\partial t} = -\frac{(p-q)\Delta x}{\Delta t}\frac{\partial P(x,t)}{\partial x} + \frac{(p+q)\Delta x^2}{2\Delta t}\frac{\partial^2 P(x,t)}{\partial x^2}. \qquad (3.5)$$

By defining the drift constant

$$D_1 = \lim_{\substack{\Delta t\to 0\\ \Delta x\to 0}} \frac{(p-q)}{\Delta t}\Delta x, \qquad (3.6)$$

and the diffusion constant

$$D_2 = \lim_{\substack{\Delta t\to 0\\ \Delta x\to 0}} \frac{(p+q)}{2\Delta t}\Delta x^2, \qquad (3.7)$$

the one-dimensional diffusion equation with drift term can be written as

$$\frac{\partial P(x,t)}{\partial t} = -D_1\frac{\partial P(x,t)}{\partial x} + D_2\frac{\partial^2 P(x,t)}{\partial x^2}. \qquad (3.8)$$

In Eq. (3.6) and (3.7) the Δt and Δx tend torwards zero simultaneously and, therefore, cannot be regarded as a differential operator. If $p = q$ the drift constant is zero, thus we yield the classical diffusion equation.

Considering the probabilities $p,\ q,\ r$ as functions of location x and time t, $p \equiv p(x,t),\ q \equiv q(x,t),\ r \equiv r(x,t)$ the Taylor expansion takes a slightly different form, resulting in the Fokker-Planck equation

$$\frac{\partial P(x,t)}{\partial t} = -\frac{\partial}{\partial x}\left[D_1(x,t)P(x,t)\right] + \frac{\partial^2}{\partial x^2}\left[D_2(x,t)P(x,t)\right]. \tag{3.9}$$

3.3 Continuity equation

The continuity equations are local forms of global conservation laws. In their most general form they read as

$$\frac{\partial \phi(\mathbf{r},t)}{\partial t} + \nabla \cdot \mathbf{f}(\mathbf{r},t) = s(\mathbf{r},t), \tag{3.10}$$

where $\phi(\mathbf{r},t)$ is a scalar quantity depending on the position $\mathbf{r} \in \mathbb{R}^3$ and time $t \in \mathbb{R}$, $\mathbf{f}(\mathbf{r},t)$ denotes the flux of $\phi(\mathbf{r},t)$, i.e. the amount of $\phi(\mathbf{r},t)$ that flows through a unit area per unit time [28], and $s(\mathbf{r},t)$ describes the source and drain, respectively, of $\phi(\mathbf{r},t)$. In our case, $\phi(\mathbf{r},t)$ is the particle density of electrons, holes or excitons, $\mathbf{f}(\mathbf{r},t)$ is the corresponding current density and $s(\mathbf{r},t)$ stands for the generation or the recombination rate. It can be derived from Maxwell's equation. The quantity $\mathbf{H}(\mathbf{r},t)$ denotes the magnetic field, $\mathbf{J}(\mathbf{r},t)$ the electric current density, $\mathbf{D}(\mathbf{r},t)$ the electric flux density and $\rho(\mathbf{r},t)$ the charge density. In the following, arguments are left out for simplicity. Using Maxwell's extension of Ampere's law

$$\nabla \times \mathbf{H} = \mathbf{J} + \frac{\partial \mathbf{D}}{\partial t}, \tag{3.11}$$

and taking the divergence of both sides

$$\nabla \cdot [\nabla \times \mathbf{H}] \quad = \quad \nabla \cdot \mathbf{J} + \frac{\partial \nabla \cdot \mathbf{D}}{\partial t}, \tag{3.12}$$

leads to

$$\nabla \cdot \mathbf{J} + \frac{\partial \nabla \cdot \mathbf{D}}{\partial t} \quad = \quad 0, \tag{3.13}$$

by taking into account that the divergence of a curl vanishes. Making use of Gauss' law

$$\nabla \cdot \mathbf{D} = \rho, \tag{3.14}$$

one yields the continuity equation for the electromagnetic case,

$$\nabla \cdot \mathbf{J} = -\frac{\partial \rho}{\partial t}, \tag{3.15}$$

with no source-drain term consideration. Including charge carrier generation and recombination terms, summarized as $\Gamma(\mathbf{r}, t)$, and including arguments, the continuity equation takes the form

$$\frac{\partial \rho(\mathbf{r}, t)}{\partial t} = -\nabla \cdot \mathbf{J}(\mathbf{r}, t) + \Gamma(\mathbf{r}, t). \tag{3.16}$$

3.4 Drift-diffusion equation

The drift-diffusion equation can be derived from Boltzmann's equation, but this will not be discussed in detail in this work (for details see e.g. [29]. Combing Eq. (3.16) with Eq. (3.9), with the probability being a charge density and regarding the multi-dimensional case, yields

$$\begin{aligned} \frac{\partial \rho}{\partial t} &= -\nabla \cdot (\mathbf{D_1}\rho) + \nabla^2(\mathbf{D_2}\rho) + \Gamma & (3.17)\\ &= -\nabla \cdot \Big\{\mathbf{D_1}\rho - \nabla(\mathbf{D_2}\rho)\Big\} + \Gamma & (3.18)\\ &= -\nabla \cdot \mathbf{J} + \Gamma & (3.19) \end{aligned}$$

with $\mathbf{D_1}$ the drift vector and $\mathbf{D_2}$ the diffusion tensor, in the general case and

$$\mathbf{J} = \mathbf{D_1}\rho - \nabla(\mathbf{D_2}\rho), \tag{3.20}$$

the corresponding current density. Further, we can make use of Einstein's relation

$$D_2 = \frac{\mu k_B T}{q}. \tag{3.21}$$

In this case D_2 is considered to be a scalar with μ denoting the particle mobility, q the elementary charge, k_B Boltzmann's constant and T the temperature. Now we have to determine the drift vector $\mathbf{D_1}$: This term describes a drift motion. Therefore $\mathbf{D_1}$ must be a velocity, generated by the occurring force which is in our case the electric field strength, thus

$$\mathbf{D_1} = \mathbf{v} = \mu \mathbf{E}. \tag{3.22}$$

Inserting Eq. (3.22) into Eq. (3.20) yields

$$\mathbf{J} = \mu \mathbf{E} \rho - \frac{\mu k_B T}{q} \nabla \rho, \tag{3.23}$$

the general drift-diffusion equation. In this equation, ρ is still the charge density but for our purpose it is more useful to substitute the particle densities for the charge density. Inserting the electron density $n = -\frac{\rho_n}{q}$ and the hole density $p = \frac{\rho_p}{q}$ into Eq. (3.16) results in

$$\frac{\partial n}{\partial t} = \frac{1}{q} \nabla \cdot \mathbf{J_n} + \Gamma^n, \tag{3.24}$$

$$\frac{\partial p}{\partial t} = -\frac{1}{q} \nabla \cdot \mathbf{J_p} + \Gamma^p. \tag{3.25}$$

The drift vector changes as well, because the force points in different directions for electrons and holes. After adapting the drift vectors in the form

$$\mathbf{D_1^n} = -\mu_n \mathbf{E} \quad \text{and} \quad \mathbf{D_1^p} = \mu_p \mathbf{E}, \tag{3.26}$$

where $\mu_{(n,p)}$ denotes the particular mobility of the charge carriers, and substituting them into Eq. (3.23), one yields the drift-diffusion equations for electrons and holes

$$\mathbf{J_n} = q \mu_n n \mathbf{E} + \mu_n k_B T \nabla n, \tag{3.27}$$

$$\mathbf{J_p} = q \mu_p p \mathbf{E} - \mu_p k_B T \nabla p. \tag{3.28}$$

3.5 Source-drain term

The source-drain terms in Eq. (3.24) and Eq. (3.25) remained undefined. However, in this particular case, when considering electrons, holes and excitons in a photovoltaic device, one observes generation (source) and recombination (drain):

$$\Gamma(\mathbf{r}, t) = G(\mathbf{r}, t) - R(\mathbf{r}, t). \tag{3.29}$$

Primarily, generation occurs if q photon is absorbed, generating an exciton, which can separate into free charge carriers. These charge carriers can, under particular circumstances, recombine to an exciton or directly relax to the ground state. In the following subsections, the different processes will be discussed in more detail.

3.5.1 Generation and recombination of particles

We will start by discussing the generation processes and then proceed to the recombination terms. It is reasonable to begin with the description of exciton generation because charge carriers are generated by exciton dissociation. After discussing the mathematical description of excitonic separation in the following subsection, the recombination processes are considered, beginning with the excitonic decay.

3.5.1.1 Exciton generation

The number of generated excitons at a certain position within the device, $\mathbf{r}$, with the distance $d(\mathbf{r})$ from the surface (in direction of the incident light beam) is proportional to the intensity of light at $\mathbf{r}$. To describe this effect, Lambert-Beer's law

$$\Phi(\mathbf{r}) = \int_{\lambda_{min}}^{\lambda_{max}} d\lambda\, \Phi_0(\lambda) \exp\left[-\alpha(\lambda) d(\mathbf{r})\right], \tag{3.30}$$

is used, where λ_{max} is the maximal occurring wavelength and represents the minimal energy necessary to absorb a photon and excite an electron from the S_0 to the S^* state (Fig. 2.3); λ_{min} is the minimal occurring wavelength, $\Phi_0(\lambda)$ the unreduced flux of incoming photons, as a function of the wavelength and $\alpha(\lambda)$ is the absorption coefficient, also as a function of λ. The maximal and minimal wavelengths are determined by the HOMO-LUMO gap of the materials used and thus might change within the device. Given a particular solar spectrum (in our case AM1.5, see Sec. 2.2), the spectral power density as a function of the wavelength, $W(\lambda)$, is known and can therefore be converted to a photon flux by

$$\Phi_0(\lambda) = \frac{W(\lambda)}{h\nu} = \frac{W(\lambda)\lambda}{hc}, \tag{3.31}$$

with h Planck's constant and c the velocity of light.

Additionally, excitons can be generated by electron-hole recombination (Sec. 3.5.1.4). Approximately, only 25 % of electrons and holes recombine to singlet excitons [4]. Combining these rates, the total exciton generation rate is given by

$$G_x(\mathbf{r}, \mathbf{E}) = \Phi(\mathbf{r}) + \frac{1}{4} R_{(n,p)}(\mathbf{r}, \mathbf{E}), \tag{3.32}$$

where $R_{(n,p)}(\mathbf{r}, \mathbf{E})$ stands for the recombination rate of charge carriers.

3.5.1.2 Charge carrier generation

Dissociation of excitons yields free charge carriers. This effect can be considered by introducing a charge carrier dissociation rate, $k_{diss}(\mathbf{r}, T, \mathbf{E})$, as described by Onsager, [7]. The model supposed by Onsager states that

$$\frac{k_{diss}(\mathbf{r}, T, \mathbf{E})}{k_{diss}(\mathbf{r}, T, 0)} = \frac{1}{\sqrt{-2b}} J_1(2\sqrt{-2b}), \tag{3.33}$$

where $\mathbf{r}$ denotes the position, T the temperature, $\mathbf{E}$ the occurring field strength and $J_1(x)$ the Bessel function of the first kind, given by [30]

$$J_\alpha(x) = \sum_{m=0}^{\infty} \frac{(-1)^m}{m!\Gamma(m+\alpha+1)} \left(\frac{x}{2}\right)^{2m+\alpha} \tag{3.34}$$

with the Gamma function $\Gamma(x)$. An alternative representation for integer values n reads

$$J_n(x) = \frac{1}{2\pi} \int_{-\pi}^{\pi} d\tau \, e^{-i(n\tau - x\sin\tau)}. \tag{3.35}$$

The factor b in Eq. (3.33) is given by

$$b = \frac{q^3|\mathbf{E}|}{8\pi\epsilon(k_B T)^2}. \tag{3.36}$$

Further, the equilibrium constant at zero field $K(0)$ is given by [6]

$$K(0) = \frac{k_{diss}(\mathbf{r}, T, 0)}{k_r} = \frac{3}{4\pi a^3} e^{-\frac{E_b}{k_B T}} \tag{3.37}$$

with the recombination rate constant

$$k_r = \frac{q}{\varepsilon}(\mu_n + \mu_p), \tag{3.38}$$

which will be discussed in detail in Sec. 3.5.1.4. The exciton binding length is denoted by a, the exciton binding energy by E_b and μ_n and μ_p stand for the mobility of electrons and holes, respectively. Combining Eq. (3.33) and Eq. (3.37) yields the final expression for the dissociation rate constant as a function of space, temperature and electric field strength:

$$k_{diss}(\mathbf{r}, T, \mathbf{E}) = \frac{3k_r}{4\pi a^3} e^{-\frac{E_b}{k_B T}} \frac{1}{\sqrt{-2b}} J_1(2\sqrt{-2b}). \tag{3.39}$$

There are two distinct approaches to describe the probability of an exciton dissociat-

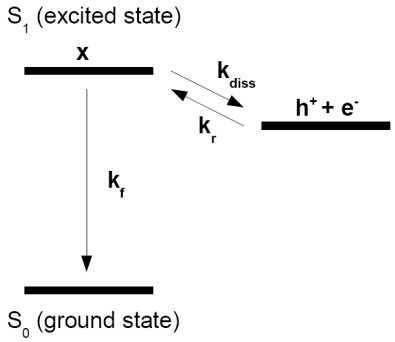

Figure 3.1: Sketch of charge transfer state dissociation kinetics assumed in Braun's model. An exciton, x in state S_1 can decay to the ground state S_0 or dissociate to unbound charge carriers, $e^- + h^+$.

ing at a given rate constant. The simplest consideration is to regard it as a chemical equilibrium reaction, as done by Buxton [4]. In this approach, the generation rate for electrons and holes is given by

$$G_{(n,p)}(\mathbf{r}, T, \mathbf{E}) = k_{diss}(\mathbf{r}, T, \mathbf{E}) x(\mathbf{r}, t). \tag{3.40}$$

Here, $x(\mathbf{r}, t)$ denotes the exciton density. A more sophisticated approach is based on evaluating the probability for an exciton dissociating immediately to charge carriers as given by Braun [6]:

$$P(\mathbf{r}, T, \mathbf{E}) = \frac{k_{diss}(\mathbf{r}, T, \mathbf{E})}{k_{diss}(\mathbf{r}, T, \mathbf{E}) + k_f}, \tag{3.41}$$

where k_f stands for the rate constant for the decay of an exciton into the ground state, see Fig. 3.1.

Fig. 3.2 shows the dissociation probability at a default set of parameters (see Sec. 4) given by Braun's model as a function of the electric field strength.

The charge carrier generation rate reads

$$G_{(n,p)}(\mathbf{r}, T, \mathbf{E}) = P(\mathbf{r}, T, \mathbf{E}) \Phi(\mathbf{r}) \tag{3.42}$$

where $\Phi(\mathbf{r})$ denotes the exciton generation rate according to Lambert-Beer's law (Sec. 3.5.1.1). It has to be emphasized that this approach assumes that an exciton can only dissociate field-assisted immediately after being generated to unbound charge carriers. Thus, the destiny of an exciton is determined *a priori*.

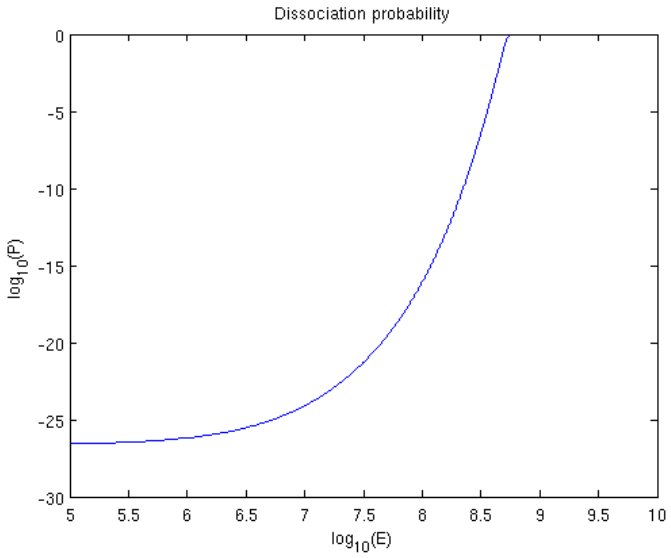

Figure 3.2: The exciton dissociation probability $P(\mathbf{r}, T, \mathbf{E})$ given by Braun's model as a function of the electric field, $|\mathbf{E}|$. The parameters used are listed in Tab. 4.1 (P3EBT).

3.5.1.3 Decay of excitons

Excitons can decay without emission of a photon from the bound state to the ground state, with a decay rate k_f usually taken to be $k_f = \frac{1}{\tau_x}$ with τ_x the average lifetime of an exciton, which is about $\tau_x = 10^{-6}$ s [4]. Thus, the exciton recombination rate is given by

$$R_x(\mathbf{r}, t) = k_f x(\mathbf{r}, t) = \frac{x(\mathbf{r}, t)}{\tau_x}. \tag{3.43}$$

where $x(\mathbf{r}, t)$ denotes the exciton density at position $\mathbf{r}$ and time t.

3.5.1.4 Charge carrier recombination

Bimolecular recombination of free charge carriers is a second order reaction and therefore proportional to the product of the electron and hole density. Consequently, the recombination rate reads

$$R_{(n,p)}(\mathbf{r}, \mathbf{E}) = k_r(\mathbf{r}, \mathbf{E}) n(\mathbf{r}, t) p(\mathbf{r}, t) \tag{3.44}$$

by using the recombination rate constant in a Langevin form [5]

$$k_r(\mathbf{r}, \mathbf{E}) = \frac{q}{\epsilon(\mathbf{r})} \left[\mu_n(\mathbf{r}, \mathbf{E}) + \mu_p(\mathbf{r}, \mathbf{E})\right], \tag{3.45}$$

as used in Sec. 3.5.1.2. Here, q denotes the elementary charge, $\epsilon(\mathbf{r}) = \epsilon_0\epsilon_r(\mathbf{r})$ the dielectric constant and $\mu_{(n,p)}(\mathbf{r}, \mathbf{E})$ the electron and hole mobility, respectively. An approach proposed by Koster [5] approximates the recombination rate constant in the organic material by

$$k_r(\mathbf{r}, \mathbf{E}) = \frac{q}{\epsilon(\mathbf{r})} \min\left[\mu_n(\mathbf{r}, \mathbf{E}), \mu_p(\mathbf{r}, \mathbf{E})\right]. \tag{3.46}$$

The justification for this assumption is that particles can only recombine, if they are at the same position. Thus, the rate has to be a function of the mobility of the slower particle.

3.5.2 Complete source-drain term

Combining the rates introduced in Sec. 3.5.1 (model introduced by Braun [6]) and leaving arguments for simplicity, the source drain terms for electrons, holes and excitons can be written as

$$\Gamma_{(n,p)} = G_{(n,p)} - R_{(n,p)} = \frac{k_{diss}}{k_{diss} + k_f}\Phi - \frac{q}{\epsilon}(\mu_n + \mu_p)np, \tag{3.47}$$

$$\Gamma_x = G_x - R_x = \left(1 - \frac{k_{diss}}{k_{diss} + k_f}\right)\Phi + \frac{1}{4}\frac{q}{\epsilon}(\mu_n + \mu_p)np - \frac{x}{\tau_x}. \tag{3.48}$$

3.6 Summary - Complete set of equations

Combining all equations previously discussed leads to the following set of equations, which must be solved.

First, the Poisson equation

$$\nabla \cdot [\epsilon(\mathbf{r})\nabla\psi(\mathbf{r})] = -\rho(\mathbf{r}), \tag{3.49}$$

provides us with the potential and the electric field strength. And second, the continuity

equations for for electrons, holes and excitons:

$$\begin{aligned}
\frac{\partial n(\mathbf{r},t)}{\partial t} &= \frac{1}{q}\nabla\cdot\mathbf{J}_n(\mathbf{r},t)+\Gamma^n(\mathbf{r}),\\
\frac{\partial p(\mathbf{r},t)}{\partial t} &= -\frac{1}{q}\nabla\cdot\mathbf{J}_p(\mathbf{r},t)+\Gamma^p(\mathbf{r}),\\
\frac{\partial x(\mathbf{r},t)}{\partial t} &= -\frac{1}{q}\nabla\cdot\mathbf{J}_x(\mathbf{r},t)+\Gamma^x(\mathbf{r}),
\end{aligned} \tag{3.50}$$

with

$$\begin{aligned}
\mathbf{J}_n(\mathbf{r},t) &= q\mu_n(\mathbf{r},\mathbf{E})n(\mathbf{r},t)\mathbf{E}(\mathbf{r})+\mu_n(\mathbf{r},\mathbf{E})k_BT\nabla n(\mathbf{r},t),\\
\mathbf{J}_p(\mathbf{r},t) &= q\mu_p(\mathbf{r},\mathbf{E})p(\mathbf{r},t)\mathbf{E}(\mathbf{r})-\mu_p(\mathbf{r},\mathbf{E})k_BT\nabla p(\mathbf{r},t),\\
\mathbf{J}_x(\mathbf{r},t) &= -\mu_x(\mathbf{r})k_BT\nabla x(\mathbf{r},t),
\end{aligned} \tag{3.51}$$

govern the temporal evolution of the electron, hole and exciton density.

The boundary conditions for this set of equations are explicitly given in Sec. 4.4. Basically, we apply Dirichlet boundary conditions at the contacts and periodic boundary conditions on the border (see Fig. 4.1). The numeric scheme for solving this set of equations is given in Sec. 4 in detail.

4 Numerical Method

In this section the numerical schemes used are explained in detail. First of all, the Poisson equation must be solved to gain the electric potential as a function of position and time caused by the charge carrier density and the applied voltage. The obtained potential is used to calculate the electric field, which is needed to determine field-dependent mobilities and charge carrier generation. Furthermore, the potential enters the continuity equations for electrons, holes and excitons, which are solved with a Scharfetter-Gummel algorithm. After solving the Poisson and continuity equations self-consistently, the next time step is evaluated in the same manner until a steady state is reached, i.e. the relative change of the charge carrier densities and exciton densities is negligible. Additionally, the current distribution change is considered, to ensure that a steady state has been reached.

The device is assumed to be invariant in the third dimension. Thus, only a two-dimensional cut through the anode and cathode is considered as a representative unit. This area is discretized by a grid, in order to give every position unambiguous coordinates of the form

$$P_{i,j} = (x_i, y_j)$$

with $i = 0, 1, \ldots, i_{max}$ and $j = 0, 1, \ldots, j_{max}$. The grid-points are defined by $x_0 = y_0 = 0$ and

$$\begin{aligned} x_{i+1} &= x_i + \Delta x_i, \quad i = 0, 1, \ldots, i_{max-1} \\ y_{j+1} &= y_j + \Delta y_j, \quad j = 0, 1, \ldots, j_{max-1}. \end{aligned}$$

On this grid we define the necessary functions and solve the corresponding equations based on a certain discretization scheme to sets of linear algebraic equations. These linear systems of equations are solved iteratively.

In principle, we consider a matrix $\mathbf{A} \in \mathbb{C}^{n \times n}$ which describes our set of equations with the right side $\mathbf{b} \in \mathbb{C}^n$ and the vector of unknowns $\mathbf{z} \in \mathbb{C}^n$ in the form

$$\mathbf{A}\mathbf{z} = \mathbf{b} \tag{4.1}$$

Now, we introduce an invertible matrix $\mathbf{B} \in \mathbb{C}^{n\times n}$. Substituting it into Eq. (4.1) yields

$$[\mathbf{B} + (\mathbf{A} - \mathbf{B})]\,\mathbf{z} = \mathbf{b}. \tag{4.2}$$

By multiplying both sites with $\mathbf{B}^{-1}$, we get the fixed point equation

$$\mathbf{z} = \mathbf{B}^{-1}\,(\mathbf{B} - \mathbf{A})\,\mathbf{z} + \mathbf{B}^{-1}\mathbf{b}. \tag{4.3}$$

Defining $\mathbf{M} := \mathbf{I} - \mathbf{B}^{-1}\mathbf{A}$, with the identity matrix $\mathbf{I}$, and choosing the starting value as $\mathbf{z}_0$, we can evaluate the solution vector iteratively by

$$\mathbf{z}^{k+1} = \mathbf{M}\mathbf{z}^k + \mathbf{B}^{-1}\mathbf{b}. \tag{4.4}$$

The solution is regarded as converged, if $|\mathbf{z}^{k+1} - \mathbf{z}^k| < \eta$, where η denotes a chosen limit. We chose $\mathbf{B} = \mathbf{I}$ for simplicity.

Another way to solve the equation is to express every z_i, $i = 1, \ldots, N$ as function of the remaining components of the vector of unknowns, z_j, $j = 1, \ldots, i-1, i+1, \ldots, N$, with $\mathbf{z} = \{z_i\}_{i=1,N}$. To illustrate this method, we rewrite Eq. (4.4) in terms of the components:

$$z_i = \sum_{j=1}^{N} m_{ij} z_j + b_i. \quad i = 1, \ldots, N \tag{4.5}$$

Here, m_{ij} and b_i denote the elements of $\mathbf{M}$ and $\mathbf{b}$, respectively. Expressing z_i from Eq. (4.5) yields

$$z_i = \frac{1}{1 - m_{ii}} \left[\sum_{\substack{j=1 \\ j\neq i}}^{N} m_{ij} x_j + b_i \right]. \tag{4.6}$$

Inserting the definition of the matrix $\mathbf{M}$ (with $\mathbf{B} = \mathbf{I}$, i.e. $m_{ij} = \delta_{ij} - a_{ij}$, where a_{ij} denote the components of $\mathbf{A}$ and $\delta_{i,j}$ Kronecker's delta, we obtain

$$z_i = \frac{1}{a_{ii}} \left[b_i - \sum_{\substack{j=1 \\ j\neq i}}^{N} a_{ij} z_j \right]. \tag{4.7}$$

This equation is the basis of the well-known Gauss-Seidel algorithm for equations with $a_{ii} \neq 0$, $\forall i$. Including the iteration index k and replacing all elements $z_j^k = z_j^{k+1}$ for

$j \leq i$ yields

$$z_i^{k+1} = \frac{1}{a_{ii}} \left[b_i - \sum_{j=1}^{i-1} a_{ij} z_j^{k+1} - \sum_{j=i+1}^{N} a_{ij} z_j^k \right]. \tag{4.8}$$

4.1 Poisson equation

The Poisson equation

$$\nabla \cdot [\epsilon(\mathbf{r}) \nabla \psi(\mathbf{r})] = -\rho(\mathbf{r}), \tag{4.9}$$

is a second-order partial differential equation with the dielectric constant $\epsilon(\mathbf{r}) = \epsilon_0 \epsilon_r(\mathbf{r})$, the electric potential $\psi(\mathbf{r})$ and the charge density $\rho(\mathbf{r}) = q\,(p(\mathbf{r}) - n(\mathbf{r}))$. All these quantities are regarded as functions of $\mathbf{r} \in \mathbb{R}^2$.

This equation is numerically treated with a finite difference approach. The procedure is based on approximating the divergence of a vector field $\mathbf{f}(\mathbf{r}) = (f_x(\mathbf{r}), f_y(\mathbf{r}))$ by

$$\begin{aligned} \nabla \cdot \mathbf{f}(\mathbf{r})\Big|_{\mathbf{r}=(x_i,y_j)} \approx & \frac{f_x(x_i + \frac{1}{2}\Delta x_i, y_j) - f_x(x_i - \frac{1}{2}\Delta x_{i-1}, y_j)}{\frac{\Delta x_i + \Delta x_{i-1}}{2}} \\ & + \frac{f_y(x_i, y_j + \frac{1}{2}\Delta y_j) - f_y(x_i, y_j - \frac{1}{2}\Delta y_{j-1})}{\frac{\Delta y_j + \Delta y_{j-1}}{2}}, \end{aligned} \tag{4.10}$$

at position $\mathbf{r} = (x_i, y_j)$. In the following, we use abbreviations of the form $f_{i,j} = f(x_i, y_j)$ and $f_{i+\frac{1}{2},j} = f(x_{i+\frac{1}{2}}, y_j) = f(x_i + \frac{1}{2}\Delta x_i, y_j)$. Based on Eq. 4.10, Eq. (4.9) can be approximated as

$$\begin{aligned} \nabla \cdot [\epsilon(\mathbf{r}) \nabla \psi(\mathbf{r})]\Big|_{\mathbf{r}=(x_i,y_j)} \approx & \frac{[\epsilon(\nabla\psi)_x]_{i+\frac{1}{2},j} - [\epsilon(\nabla\psi)_x]_{i-\frac{1}{2},j}}{\frac{\Delta x_i + \Delta x_{i-1}}{2}} \\ & + \frac{[\epsilon(\nabla\psi)_y]_{i,j+\frac{1}{2}} - [\epsilon(\nabla\psi)_y]_{i,j-\frac{1}{2}}}{\frac{\Delta y_j + \Delta y_{j-1}}{2}}. \end{aligned} \tag{4.11}$$

Repeating this discretization and using

$$[f(x)g(x)]_{i,j} = f_{i,j} g_{i,j}, \tag{4.12}$$

as well as

$$[(\nabla f)_x]_{i+\frac{1}{2},j} \approx \frac{f_{i+1,j} - f_{i,j}}{\Delta x_i} \tag{4.13}$$

yields

$$\frac{[\epsilon(\nabla\psi)_x]_{i+\frac{1}{2},j} - [\epsilon(\nabla\psi)_x]_{i-\frac{1}{2},j}}{\frac{\Delta x_i + \Delta x_{i-1}}{2}} + \frac{[\epsilon(\nabla\psi)_y]_{i,j+\frac{1}{2}} - [\epsilon(\nabla\psi)_y]_{i,j-\frac{1}{2}}}{\frac{\Delta y_j + \Delta y_{j-1}}{2}} \approx$$
$$\frac{\epsilon_{i+\frac{1}{2},j}(\frac{\psi_{i+1,j}-\psi_{i,j}}{\Delta x_i}) - \epsilon_{i-\frac{1}{2},j}(\frac{\psi_{i,j}-\psi_{i-1,j}}{\Delta x_{i-1}})}{\frac{\Delta x_i + \Delta x_{i-1}}{2}} + \frac{\epsilon_{i,j+\frac{1}{2}}(\frac{\psi_{i,j+1}-\psi_{i,j}}{\Delta y_j}) - \epsilon_{i,j-\frac{1}{2}}(\frac{\psi_{i,j}-\psi_{i,j-1}}{\Delta y_{j-1}})}{\frac{\Delta y_j + \Delta y_{j-1}}{2}}. \quad (4.14)$$

Assuming equal grid spacing, i.e. $\Delta x_i = \Delta x_{i-1} = h_x$ and $\Delta y_j = \Delta y_{j-1} = h_y$ yields the descretized Poisson equation as a coupled system of linear equations.

$$\frac{1}{h_x^2}[\epsilon_{i+\frac{1}{2},j}\psi_{i+1,j} - (\epsilon_{i+\frac{1}{2},j} + \epsilon_{i-\frac{1}{2},j})\psi_{i,j} + \epsilon_{i-\frac{1}{2},j}\psi_{i-1,j}]$$
$$+\frac{1}{h_y^2}[\epsilon_{i,j+\frac{1}{2}}\psi_{i,j+1} - (\epsilon_{i,j+\frac{1}{2}} + \epsilon_{i,j-\frac{1}{2}})\psi_{i,j} + \epsilon_{i,j-\frac{1}{2}}\psi_{i,j-1}] = -\rho_{i,j}. \quad (4.15)$$

Expressing $\psi_{i,j}$ by this equation gives a way to calculate the potential at a particular grid point as a function of the value at the neighboring grid points and, hence, solving the system of N linear equations, for $i = 1, \ldots, N$, iteratively:

$$\psi_{i,j}^{n+1} =$$
$$\frac{\rho_{i,j}h_x^2h_y^2 + h_y^2(\epsilon_{i+\frac{1}{2},j}\psi_{i+1,j}^n + \epsilon_{i-\frac{1}{2},j}\psi_{i-1,j}^n) + h_x^2(\epsilon_{i,j+\frac{1}{2}}\psi_{i,j+1}^n + \epsilon_{i,j-\frac{1}{2}}\psi_{i,j-1}^n)}{h_y^2(\epsilon_{i+\frac{1}{2},j} + \epsilon_{i-\frac{1}{2},j}) + h_x^2(\epsilon_{i,j+\frac{1}{2}} + \epsilon_{i,j-\frac{1}{2}})}, \quad (4.16)$$

where n denotes the iteration index. In our particular case, the dielectric constant is assumed to be linear between grid points, thus

$$\epsilon_{i+\frac{1}{2},j} = \frac{\epsilon_{i+1,j} + \epsilon_{i,j}}{2}. \quad (4.17)$$

The solution is regarded as converged if the absolute error is less than a given threshold value η, i.e.

$$\Delta\psi = \sum_{i,j} |\psi_{i,j}^{n+1} - \psi_{i,j}^n| \leq \eta. \quad (4.18)$$

4.2 Continuity equation - Scharfetter-Gummel algorithm

The so-called Scharfetter-Gummel scheme [31] considers the drift-diffusion current equation (3.51) approximately by assuming the current to be constant between two neighboring grid points. Therefore, the current is always calculated between two grid points as a function of the neighboring charge carrier densities.

To demonstrate this approach we will, at first, for simplicity, only consider the drift-diffusion equation for electrons in one dimension:

$$J_n = q\mu_n E n(x) + k_B T \mu_n \frac{\partial n(x)}{\partial x} = const, \quad \forall x \in [x_i, x_{i+1}], \tag{4.19}$$

where we regard the electron density as a function of space, independent of time. The solution of Eq. (4.19) is given by

$$n(x) = \tilde{C_1} \exp\left(-\frac{qE}{k_B T} x\right) + \frac{J_n}{q\mu_n E}. \tag{4.20}$$

Here, $\tilde{C_1}$ denotes an arbitrary constant. First, we chose

$$\tilde{C_1} = C_1 \exp\left(\frac{qE}{k_B T} x_i\right), \tag{4.21}$$

with another constant C_1. Inserting Eq. (4.21) into Eq. (4.20) yields

$$n(x) = C_1 \exp\left(-\frac{qE}{k_B T}(x - x_i)\right) + \frac{J_n}{q\mu_n E}. \quad \forall x \in [x_i, x_{i+1}] \tag{4.22}$$

Inserting $x = x_i$ and solving Eq. (4.22) for C_1 gives

$$C_1 = n_i - \frac{J_n}{q\mu_n E}. \tag{4.23}$$

Using this expression for C_1 and inserting $x = x_{i+1}$ into Eq. (4.22), leads to

$$n_{i+1} = \left(n_i - \frac{J_n}{q\mu_n E}\right) \exp\left(-\frac{qE}{k_B T} \Delta x_i\right) + \frac{J_n}{q\mu_n E}, \tag{4.24}$$

Finally, solving for J_n gives

$$J_n = q\mu_n E \frac{n_{i+1} - n_i \exp\left(-\frac{qE}{k_B T} \Delta x_i\right)}{1 - \exp\left(-\frac{qE}{k_B T} \Delta x_i\right)}. \tag{4.25}$$

Thus, we yield an expression, which unambiguously determines the current within a given interval under the assumption that in this interval Eq. (4.19) is valid and the neighboring charge carrier densities are known.

Approximating the electric field E by

$$E_i \approx -\frac{\psi_{i+1} - \psi_i}{\Delta x_i}, \tag{4.26}$$

and expressing Eq. (4.25) in terms of the Bernoulli function

$$B(x) = \frac{x}{\exp(x) - 1}, \tag{4.27}$$

yields the current density between two grid points as

$$J_n^{i+\frac{1}{2}} = \frac{\mu_n^{i+\frac{1}{2}} V_t q}{\Delta x_i} \left[n_{i+1} B\left(\frac{\psi_{i+1} - \psi_i}{V_t} \right) - n_i B\left(-\frac{\psi_{i+1} - \psi_i}{V_t} \right) \right], \tag{4.28}$$

with the thermal voltage $V_t = \frac{k_B T}{q}$ and

$$\mu_n^{i+\frac{1}{2}} = \frac{\mu_n^i + \mu_n^{i+1}}{2}, \tag{4.29}$$

Now, we introduce the generalized potential

$$\Psi_{i,j}^{(n,p)} := \psi_{i,j} - \frac{\Theta_{i,j}^{(n,p)}}{q}, \tag{4.30}$$

with $\Theta_{i,j}^{(n,p)}$ the relative height of the HOMO and LUMO levels, respectively. The effective potential is different for electrons and holes and dominates their movement within the device. Extending Eq. (4.28) to the multi-dimension case and using (4.30), finally, leads to the Scharfetter-Gummel current equations:

$${}^x J_n^{i+\frac{1}{2},j} = \frac{\mu_n^{i+\frac{1}{2},j} V_t q}{\Delta x_i} \left[n_{i+1,j} B\left(\frac{\Psi_{i+1,j}^n - \Psi_{i,j}^n}{V_t} \right) - n_{i,j} B\left(-\frac{\Psi_{i+1,j}^n - \Psi_{i,j}^n}{V_t} \right) \right], \tag{4.31}$$

$${}^y J_n^{i,j+\frac{1}{2}} = \frac{\mu_n^{i,j+\frac{1}{2}} V_t q}{\Delta y_j} \left[n_{i,j+1} B\left(\frac{\Psi_{i,j+1}^n - \Psi_{i,j}^n}{V_t} \right) - n_{i,j} B\left(-\frac{\Psi_{i,j+1}^n - \Psi_{i,j}^n}{V_t} \right) \right], \tag{4.32}$$

$${}^x J_p^{i+\frac{1}{2},j} = \frac{\mu_p^{i+\frac{1}{2},j} V_t q}{\Delta x_i} \left[p_{i,j} B\left(\frac{\Psi_{i+1,j}^p - \Psi_{i,j}^p}{V_t} \right) - p_{i+1,j} B\left(-\frac{\Psi_{i+1,j}^p - \Psi_{i,j}^p}{V_t} \right) \right], \tag{4.33}$$

$${}^y J_p^{i,j+\frac{1}{2}} = \frac{\mu_p^{i,j+\frac{1}{2}} V_t q}{\Delta y_j} \left[p_{i,j} B\left(\frac{\Psi_{i,j+1}^p - \Psi_{i,j}^p}{V_t} \right) - p_{i,j+1} B\left(-\frac{\Psi_{i,j+1}^p - \Psi_{i,j}^p}{V_t} \right) \right]. \tag{4.34}$$

Now, the continuity equations, Eq. (3.50), are discretized and then Eq. (4.31) - (4.34) are inserted into the resulting equations.

The time derivative of the particle densities and the space derivative of the current-densities are approximated with a first order finite difference scheme. The continuity

equation (3.50) for electrons at a position $\mathbf{r} = (x_i, y_j)$ reads

$$\frac{n_{i,j}^{t+\Delta t} - n_{i,j}^{t}}{\Delta t} = \frac{1}{q}\left(\frac{{}_n^x J_{i+\frac{1}{2}j}^{t+\Delta t} - {}_n^x J_{i-\frac{1}{2},j}^{t+\Delta t}}{\frac{\Delta x_i + \Delta x_{i-1}}{2}} + \frac{{}_n^y J_{i,j+\frac{1}{2}}^{t+\Delta t} - {}_n^y J_{i,j-\frac{1}{2}}^{t+\Delta t}}{\frac{\Delta y_j + \Delta y_{j-1}}{2}}\right) + {}^n\Gamma_{i,j}^{t+\Delta t}, \tag{4.35}$$

where we used an implicit time step method and the discretization described in Eq. (4.10). Here, $\Gamma^{(n,p)}(\mathbf{r},t)|_{\mathbf{r}=(x_i,y_j)} = {}^{(n,p)}\Gamma_{i,j}^{t}$ denotes the source-drain term at a particular position. Inserting Eq. (4.31) and (4.32) into Eq. (4.35) and replacing $\mu_n^{i,j} V_t = D_n^{i,j}$ yields

$$\begin{aligned}
&\frac{n_{i,j}^{t+\Delta t} - n_{i,j}^{t}}{\Delta t} = \\
&\frac{1}{q}\Bigg\{ \frac{1}{\frac{\Delta x_i + \Delta x_{i-1}}{2}}\Bigg[\frac{D_n^{i+\frac{1}{2},j} q}{\Delta x_i}\left(n_{i+1,j}^{t+\Delta t} B\left(\frac{{}^n\Psi_{i+1,j}^{t+\Delta t} - {}^n\Psi_{i,j}^{t+\Delta t}}{V_t}\right) - n_{i,j}^{t+\Delta t} B\left(-\frac{{}^n\Psi_{i+1,j}^{t+\Delta t} - {}^n\Psi_{i,j}^{t+\Delta t}}{V_t}\right)\right) \\
&\quad - \frac{D_n^{i-\frac{1}{2},j} q}{\Delta x_{i-1}}\left(n_{i,j}^{t+\Delta t} B\left(\frac{{}^n\Psi_{i,j}^{t+\Delta t} - {}^n\Psi_{i-1,j}^{t+\Delta t}}{V_t}\right) - n_{i-1,j}^{t+\Delta t} B\left(-\frac{{}^n\Psi_{i,j}^{t+\Delta t} - {}^n\Psi_{i-1,j}^{t+\Delta t}}{V_t}\right)\right)\Bigg] \\
&+ \frac{1}{\frac{\Delta y_j + \Delta y_{j-1}}{2}}\Bigg[\frac{D_n^{i,j+\frac{1}{2}} q}{\Delta y_j}\left(n_{i,j+1}^{t+\Delta t} B\left(\frac{{}^n\Psi_{i,j+1}^{t+\Delta t} - {}^n\Psi_{i,j}^{t+\Delta t}}{V_t}\right) - n_{i,j}^{t+\Delta t} B\left(-\frac{{}^n\Psi_{i,j+1}^{t+\Delta t} - {}^n\Psi_{i,j}^{t+\Delta t}}{V_t}\right)\right) \\
&\quad - \frac{D_n^{i,j-\frac{1}{2}} q}{\Delta y_{j-1}}\left(n_{i,j}^{t+\Delta t} B\left(\frac{{}^n\Psi_{i,j}^{t+\Delta t} - {}^n\Psi_{i,j-1}^{t+\Delta t}}{V_t}\right) - n_{i,j-1}^{t+\Delta t} B\left(-\frac{{}^n\Psi_{i,j}^{t+\Delta t} - {}^n\Psi_{i,j-1}^{t+\Delta t}}{V_t}\right)\right)\Bigg]\Bigg\} \\
&\qquad + {}^n\Gamma_{i,j}^{t+\Delta t}.
\end{aligned} \tag{4.36}$$

Solving Eq. (4.36) for $n_{i,j}^{t+\Delta t}$ yields

$$
\begin{aligned}
n_{i,j}^{t+\Delta t} = \Bigg[& \left({}^{n}\Gamma_{i,j}^{t+\Delta t} + \frac{n_{i,j}^{t}}{\Delta t} \right) \frac{\Delta x_i + \Delta x_{i-1}}{2} \frac{\Delta y_j + \Delta y_{j-1}}{2} \\
& + n_{i+1,j}^{t+\Delta t} D_n^{i+\frac{1}{2},j} B \left(\frac{{}^{n}\Psi_{i+1,j}^{t+\Delta t} - {}^{n}\Psi_{i,j}^{t+\Delta t}}{V_t} \right) \frac{\Delta y_j + \Delta y_{j-1}}{2\Delta x_i} \\
& + n_{i,j+1}^{t+\Delta t} D_n^{i,j+\frac{1}{2}} B \left(\frac{{}^{n}\Psi_{i,j+1}^{t+\Delta t} - {}^{n}\Psi_{i,j}^{t+\Delta t}}{V_t} \right) \frac{\Delta x_i + \Delta x_{i-1}}{2\Delta y_j} \\
& + n_{i-1,j}^{t+\Delta t} D_n^{i-\frac{1}{2},j} B \left(\frac{{}^{n}\Psi_{i-1,j}^{t+\Delta t} - {}^{n}\Psi_{i,j}^{t+\Delta t}}{V_t} \right) \frac{\Delta y_j + \Delta y_{j-1}}{2\Delta x_{i-1}} \\
& + n_{i,j-1}^{t+\Delta t} D_n^{i,j-\frac{1}{2}} B \left(\frac{{}^{n}\Psi_{i,j-1}^{t+\Delta t} - {}^{n}\Psi_{i,j}^{t+\Delta t}}{V_t} \right) \frac{\Delta x_i + \Delta x_{i-1}}{2\Delta y_{j-1}} \Bigg] \\
& \Bigg[D_n^{i+\frac{1}{2},j} B \left(\frac{{}^{n}\Psi_{i,j}^{t+\Delta t} - {}^{n}\Psi_{i+1,j}^{t+\Delta t}}{V_t} \right) \frac{\Delta y_j + \Delta y_{j-1}}{2\Delta x_i} \\
& + D_n^{i,j+\frac{1}{2}} B \left(\frac{{}^{n}\Psi_{i,j}^{t+\Delta t} - {}^{n}\Psi_{i,j+1}^{t+\Delta t}}{V_t} \right) \frac{\Delta x_i + \Delta x_{i-1}}{2\Delta y_j} \\
& + D_n^{i-\frac{1}{2},j} B \left(\frac{{}^{n}\Psi_{i,j}^{t+\Delta t} - {}^{n}\Psi_{i-1,j}^{t+\Delta t}}{V_t} \right) \frac{\Delta y_j + \Delta y_{j-1}}{2\Delta x_{i-1}} \\
& + D_n^{i,j-\frac{1}{2}} B \left(\frac{{}^{n}\Psi_{i,j}^{t+\Delta t} - {}^{n}\Psi_{i,j-1}^{t+\Delta t}}{V_t} \right) \frac{\Delta x_i + \Delta x_{i-1}}{2\Delta y_{j-1}} \\
& + \frac{1}{\Delta t} \frac{\Delta x_i + \Delta x_{i-1}}{2} \frac{\Delta y_j + \Delta y_{j-1}}{2} \Bigg]^{-1} .
\end{aligned}
\tag{4.37}
$$

By applying the same procedure on the continuity equations (3.50) and drift-diffusion current equations (3.51) for holes and excitons, one gets the corresponding discretized

drift-diffusion equations:

$$
\begin{aligned}
p_{i,j}^{t+\Delta t} = \Bigg[& \left({}^{p}\Gamma_{i,j}^{t+\Delta t} + \frac{p_{i,j}^{t}}{\Delta t} \right) \frac{\Delta x_i + \Delta x_{i-1}}{2} \frac{\Delta y_j + \Delta y_{j-1}}{2} \\
& + p_{i+1,j}^{t+\Delta t} D_p^{i+\frac{1}{2},j} B \left(\frac{{}^{p}\Psi_{i,j}^{t+\Delta t} - {}^{p}\Psi_{i+1,j}^{t+\Delta t}}{V_t} \right) \frac{\Delta y_j + \Delta y_{j-1}}{2\Delta x_i} \\
& + p_{i,j+1}^{t+\Delta t} D_p^{i,j+\frac{1}{2}} B \left(\frac{{}^{p}\Psi_{i,j}^{t+\Delta t} - {}^{p}\Psi_{i,j+1}^{t+\Delta t}}{V_t} \right) \frac{\Delta x_i + \Delta x_{i-1}}{2\Delta y_j} \\
& + p_{i-1,j}^{t+\Delta t} D_p^{i-\frac{1}{2},j} B \left(\frac{{}^{p}\Psi_{i,j}^{t+\Delta t} - {}^{p}\Psi_{i-1,j}^{t+\Delta t}}{V_t} \right) \frac{\Delta y_j + \Delta y_{j-1}}{2\Delta x_{i-1}} \\
& + p_{i,j-1}^{t+\Delta t} D_p^{i,j-\frac{1}{2}} B \left(\frac{{}^{p}\Psi_{i,j}^{t+\Delta t} - {}^{p}\Psi_{i,j-1}^{t+\Delta t}}{V_t} \right) \frac{\Delta x_i + \Delta x_{i-1}}{2\Delta y_{j-1}} \Bigg] \\
& \Bigg[D_p^{i+\frac{1}{2},j} B \left(\frac{{}^{p}\Psi_{i+1,j}^{t+\Delta t} - {}^{p}\Psi_{i,j}^{t+\Delta t}}{V_t} \right) \frac{\Delta y_j + \Delta y_{j-1}}{2\Delta x_i} \\
& + D_p^{i,j+\frac{1}{2}} B \left(\frac{{}^{p}\Psi_{i,j+1}^{t+\Delta t} - {}^{p}\Psi_{i,j}^{t+\Delta t}}{V_t} \right) \frac{\Delta x_i + \Delta x_{i-1}}{2\Delta y_j} \\
& + D_p^{i-\frac{1}{2},j} B \left(\frac{{}^{p}\Psi_{i-1,j}^{t+\Delta t} - {}^{p}\Psi_{i,j}^{t+\Delta t}}{V_t} \right) \frac{\Delta y_j + \Delta y_{j-1}}{2\Delta x_{i-1}} \\
& + D_p^{i,j-\frac{1}{2}} B \left(\frac{{}^{p}\Psi_{i,j-1}^{t+\Delta t} - {}^{p}\Psi_{i,j}^{t+\Delta t}}{V_t} \right) \frac{\Delta x_i + \Delta x_{i-1}}{2\Delta y_{j-1}} \\
& + \frac{1}{\Delta t} \frac{\Delta x_i + \Delta x_{i-1}}{2} \frac{\Delta y_j + \Delta y_{j-1}}{2} \Bigg]^{-1} .
\end{aligned}
\tag{4.38}
$$

$$
\begin{aligned}
x_{i,j}^{t+\Delta t} = \Bigg[& \left({}^{x}\Gamma_{i,j} - \frac{x_{i,j}^{t}}{\Delta t} \right) \frac{\Delta x_i + \Delta x_{i-1}}{2} \frac{\Delta y_j + \Delta y_{j-1}}{2} \\
& + x_{i+1,j}^{t+\Delta t} D_x^{i+\frac{1}{2},j} \frac{\Delta y_j + \Delta y_{j-1}}{2\Delta x_i} + x_{i,j+1}^{t+\Delta t} D_x^{i,j+\frac{1}{2}} \frac{\Delta x_i + \Delta x_{i-1}}{2\Delta y_j} \\
& + x_{i-1,j}^{t+\Delta t} D_x^{i-\frac{1}{2},j} \frac{\Delta y_j + \Delta y_{j-1}}{2\Delta x_{i-1}} + x_{i,j-1}^{t+\Delta t} D_x^{i,j-\frac{1}{2}} \frac{\Delta x_i + \Delta x_{i-1}}{2\Delta y_{j-1}} \Bigg] \\
& \Bigg[D_x^{i+\frac{1}{2},j} \frac{\Delta y_j + \Delta y_{j-1}}{2\Delta x_i} + D_x^{i,j+\frac{1}{2}} \frac{\Delta x_i + \Delta x_{i-1}}{2\Delta y_j} \\
& + D_x^{i-\frac{1}{2},j} \frac{\Delta y_j + \Delta y_{j-1}}{2\Delta x_{i-1}} + D_x^{i,j-\frac{1}{2}} \frac{\Delta x_i + \Delta x_{i-1}}{2\Delta y_{j-1}} \\
& + \frac{1}{\Delta t} \frac{\Delta x_i + \Delta x_{i-1}}{2} \frac{\Delta y_j + \Delta y_{j-1}}{2} \Bigg]^{-1} .
\end{aligned} \tag{4.39}
$$

Note that there is no drift term in the transport equations for excitons (see Eq. 3.51).

4.3 Additional steps

Before starting the iterative cycle the exciton generation rate is calculated by using an experimental sun spectrum and, if Lambert-Beer's law is considered, Eq. (3.30), an experimental absorption coefficient α is taken into account.

After solving the Poisson equation and before evaluating the continuity equations, the mobilities, the recombination rate constant and the exciton dissociation rate constant must be updated, following Eq. (2.9), Eq. (3.38) and (3.39), respectively. Therefore, the gained potential is used to calculate the local occurring field strength $\mathbf{E} = (E_x, E_y)$ by

$$
E_x(\mathbf{r})\Big|_{\mathbf{r}=(x_i,y_j)} = -[\nabla\psi(\mathbf{r})]_x\Big|_{\mathbf{r}=(x_i,y_j)} \approx \frac{\psi_{i-1,j} - \psi_{i+1,j}}{\Delta x_i + \Delta x_{i-1}}, \tag{4.40}
$$

$$
E_y(\mathbf{r})\Big|_{\mathbf{r}=(x_i,y_j)} = -[\nabla\psi(\mathbf{r})]_y\Big|_{\mathbf{r}=(x_i,y_j)} \approx \frac{\psi_{i,j-1} - \psi_{i,j+1}}{\Delta y_j + \Delta y_{j-1}}, \tag{4.41}
$$

and therefore

$$
|\mathbf{E}(\mathbf{r})|\Big|_{\mathbf{r}=(x_i,y_j)} = |\mathbf{E}_{i,j}| \approx \sqrt{\left(\frac{\psi_{i-1,j} - \psi_{i+1,j}}{\Delta x_i + \Delta x_{i-1}} \right)^2 + \left(\frac{\psi_{i,j-1} - \psi_{i,j+1}}{\Delta y_j + \Delta y_{j-1}} \right)^2}. \tag{4.42}
$$

Hence, the mobility is given by

$$
\mu_{(n,p)}^{i,j} = {}^{0}\mu_{(n,p)}^{i,j} \exp\left(\gamma |\mathbf{E}_{i,j}|\right), \tag{4.43}
$$

where ${}^{0}\mu^{i,j}_{(n,p)}$ denotes the mobility at zero field, according to Eq. (2.9). The exciton dissociation rate constant k_{diss} and the recombination rate constant k_r are updated following Eqs. (3.39) and (3.38).

The charge carrier generation, Eq. (3.42), and the particle recombination rates, Eq. (3.44) and (3.43), are updated in the drift-diffusion cycle after every iteration step because of their dependence on the local charge carrier densities.

4.4 Simulating the charge transport in organic solar cells

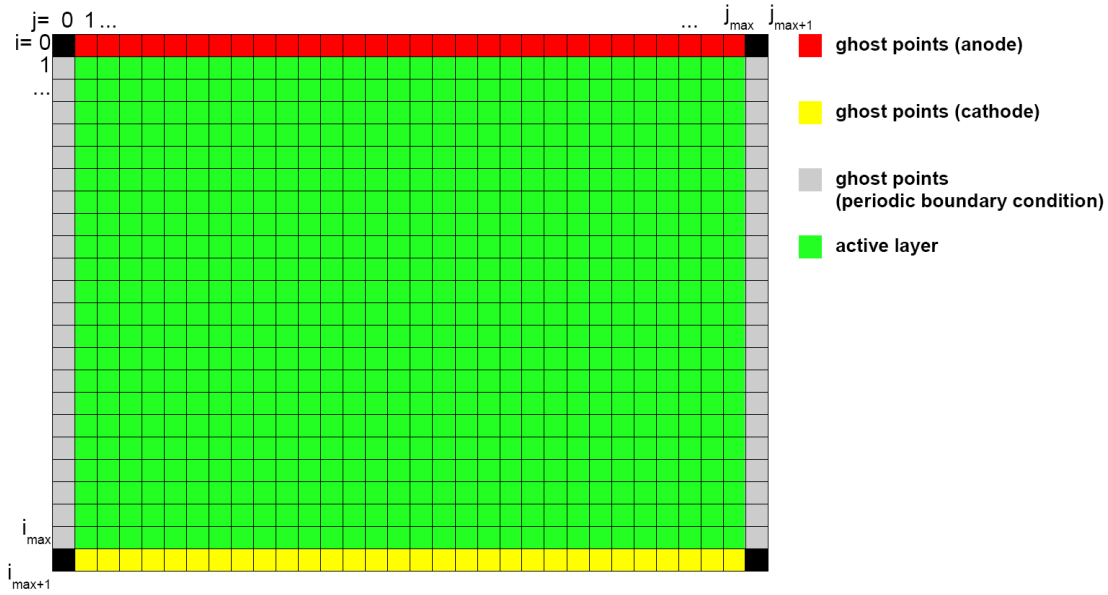

Figure 4.1: Discretization scheme for the simulation. Anode, cathode, active layer and ghost points are indicated with red, yellow, green an grey, respectively.

The device is partitioned into four different parts: anode, cathode, active layer, which consist of an organic and an inorganic part, and ghost points (Fig. 4.1). On anode and cathode the intrinsic particle densities and the potential, depending on the applied

voltage, are set constant,

$$
\begin{aligned}
n_{Anode} &= 0\ \mathrm{m}^{-3}, \quad n_{Cathode} = 10^{22}\ \mathrm{m}^{-3} \\
p_{Anode} &= 10^{22}\ \mathrm{m}^{-3}, \quad p_{Cathode} = 0\ \mathrm{m}^{-3} \\
x_{Anode} &= 0\ \mathrm{m}^{-3}, \quad x_{Cathode} = 0\ \mathrm{m}^{-3} \\
\psi_{Anode} &= \frac{V_a - E_{gap}}{2}, \quad \psi_{Cathode} = -\frac{V_a - E_{gap}}{2},
\end{aligned}
$$

with the applied voltage V_a and the band gap difference between organic and inorganic layers resulting from the assumption of ohmic contacts and the used materials, E_{gap}, (Fig. 4.2). Furthermore, the mobilities are set constant:

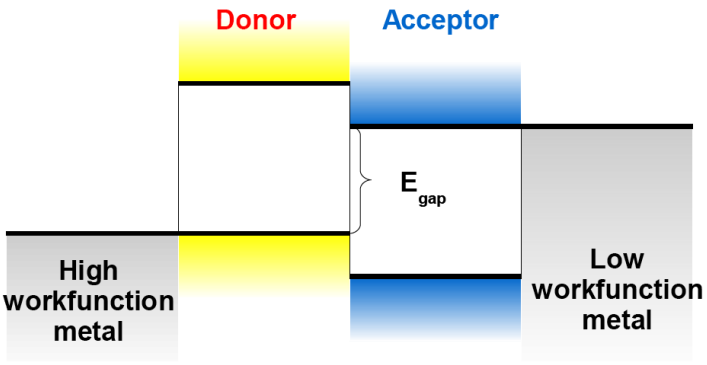

Figure 4.2: Illustration of the definition of E_{gap}.

$$
\begin{aligned}
\mu^{(n,p)}_{Anode} &= \mu^{(n,p)}_{Cathode} = 10^{-6}\mathrm{m}^2\mathrm{V}^{-1}\mathrm{s}^{-1} \\
\mu^{x}_{Anode} &= \mu^{x}_{Cathode} = 0\ \mathrm{m}^2\mathrm{V}^{-1}\mathrm{s}^{-1}
\end{aligned}
$$

The additional ghost points are used to implement periodic boundary conditions, which is done by setting

$$\begin{aligned} \psi_{i,0} &= \psi_{i,j_{max}}, \quad \psi_{i,j_{max+1}} = \psi_{i,1}, \\ n_{i,0} &= n_{i,j_{max}}, \quad n_{i,j_{max+1}} = n_{i,1}, \\ p_{i,0} &= p_{i,j_{max}}, \quad p_{i,j_{max+1}} = p_{i,1}, \\ x_{i,0} &= x_{i,j_{max}}, \quad x_{i,j_{max+1}} = x_{i,1}, \\ D^{i,0}_{(n,p,x)} &= D^{i,j_{max}}_{(n,p,x)}, \quad D^{i,j_{max+1}}_{(n,p,x)} = D^{i,1}_{(n,p,x)}, \end{aligned} \tag{4.44}$$

for $i = 1, \ldots, i_{max}$. Within the active layer the corresponding equations are solved iteratively. The input parameters are the mobilities at zero field, ${}^0\mu^{i,j}_{(n,p)}$, the HOMO and LUMO levels, the dielectric constant $\epsilon_{i,j}$, the absorption coefficient α, the exciton binding energy E_b, the exciton binding length a, the average exciton lifetime τ_x, the temperature T and the solar spectrum AM1.5. The input parameters are summarized in Tab. 4.1.

Table 4.1: Default input parameters for the active layers: organic donor layer (D), inorganic acceptor layer (A).

	P3EBT (D)	P3HT (D)	F8T2 (D)	CIS (A)
HOMO / eV	-5.6	-5.2	-5.4	-5.6
LUMO / eV	-3.7	-3.5	-2.5	-4.1
${}^0\mu_n$ / $\mathrm{m^2V^{-1}s^{-1}}$	10^{-8}	10^{-8}	10^{-8}	10^{-6}
${}^0\mu_p$ / $\mathrm{m^2V^{-1}s^{-1}}$	10^{-8}	10^{-8}	10^{-8}	10^{-6}
μ_x / $\mathrm{m^2V^{-1}s^{-1}}$	$3.86 \cdot 10^{-9}$	$3.86 \cdot 10^{-9}$	$3.86 \cdot 10^{-9}$	-
ϵ_r	1	1	1	10
α / $\mathrm{m^{-1}}$	$2 \cdot 10^7$	$2 \cdot 10^7$	$2 \cdot 10^7$	$2 \cdot 10^7$
E_b / eV	0.5	0.5	0.5	0.5
a / nm	1.3	1.3	1.3	1.3
τ_x / s	10^{-6}	10^{-6}	10^{-6}	-
T / K	298.15	298.15	298.15	298.15

Excitons are assumed to exist only in the organic layer, i.e., every exciton reaching the inorganic layer or being generated in the inorganic layer separates directly into an electron and a hole. To distinguish between organic (D: Donor) and inorganic (A: Acceptor) parts in the active layer, a matrix, *mask*, is defined as input parameter with

$$mask_{i,j} = \begin{cases} 0, (i,j) \in D \\ 1, (i,j) \in A \end{cases} \tag{4.45}$$

Furthermore, several switches are implemented to control the different processes taking place within the active layer and to extract their effects in a detailed manner:

- switchlight: Turn on/off light illumination.
- switchlambertbeer: Turn on/off Lambert-Beer's law.
- switchre: Turn on/off recombination.
- switchmob: Turn on/off field-dependent mobilities.
- switchex: Turn on/off exciton consideration.
- switchbraun: Turn on/off Braun's exciton dissociation model.
- switchrandom: Turn on/off random levels for inorganic material.

Fig. 4.3 gives a short overview of the functionality of the different switches, showing the different treatment of particular quantities.

Switches

switchlight = 0	**switchlight = 1**
$\Phi_{i,j} = 0$ $x_{i,j} = 0$	$\Phi_{i,j} \neq 0$ $x_{i,j} \neq 0$
switchlambertbeer = 0	**switchlambertbeer = 1**
$\Phi_{i,j} = \int_{\lambda_{min}}^{\lambda_{max}} d\lambda\, \Phi_{i,j}^{0}(\lambda)$	$\Phi_{i,j} = \int_{\lambda_{min}}^{\lambda_{max}} d\lambda\, \Phi_{i,j}^{0}(\lambda) \exp[-\alpha(\lambda) x_i]$
switchre = 0	**switchre = 1**
$R_{i,j}^{(n,p,x)} = 0$	$R_{i,j}^{(n,p)} = k_r^{i,j} n_{i,j} p_{i,j}$ $R_{i,j}^{x} = \frac{x_{i,j}}{\tau_x}$
switchmob = 0	**switchmob = 1**
$\mu_{i,j}^{(n,p)} = {}^{0}\mu_{i,j}^{(n,p)}$	$\mu_{i,j}^{(n,p)} = {}^{0}\mu_{i,j}^{(n,p)} \exp\left(\gamma \lvert E_{i,j} \rvert\right)$
switchex = 0	**switchex = 1**
$x_{i,j} = 0$ $G_{i,j}^{(n,p)} = \Phi_{i,j}\ \forall i,j : mask_{i,j} = 1$ $G_{i,j}^{(n,p)} = 0\ \forall i,j : mask_{i,j} = 0$	$x_{i,j} \neq 0\ \forall i,j : mask_{i,j} = 0$ $G_{i,j}^{(n,p)} = G_{i,j}^{(n,p)}(\Phi_{i,j}, x_{i-1,j}, ...)\ \forall i,j : mask_{i,j} = 1$ $G_{i,j}^{(n,p)} = G_{i,j}^{(n,p)}(k_{diss}^{i,j})\ \forall i,j : mask_{i,j} = 0$
switchbraun = 0	**switchbraun = 1**
$G_{i,j}^{(n,p)} = x_{i,j} k_{diss}^{i,j}$	$G_{i,j}^{(n,p)} = P_{i,j}(k_{diss}^{i,j}, E_{i,j}) \Phi_{i,j}$
switchrandom = 0	**switchrandom = 1**
$\Theta_{i,j}^{(n,p)} = const.\ \forall i,j$	$\Theta_{i,j}^{(n,p)} = const.\ \forall i,j : mask_{i,j} = 0$ $\Theta_{i,j}^{(n,p)} = const. + 0.05 \times rand_{-1,1}\ \forall i,j : mask_{i,j} = 1$

Figure 4.3: Functionality of the different switches. The quantity $rand_{-1,1}$ denotes uniform distributed random numbers taken from the interval $[-1, 1]$.

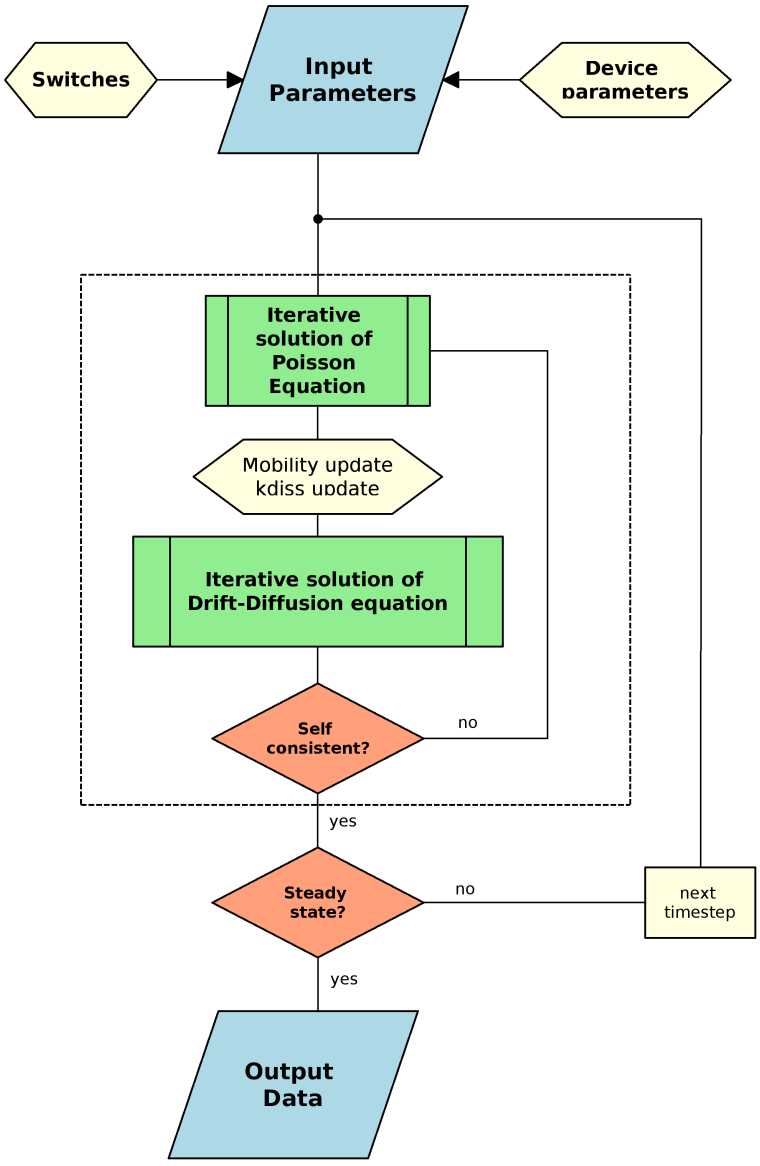

Figure 4.4: Iteration flowchart for solving the complete algorithm.

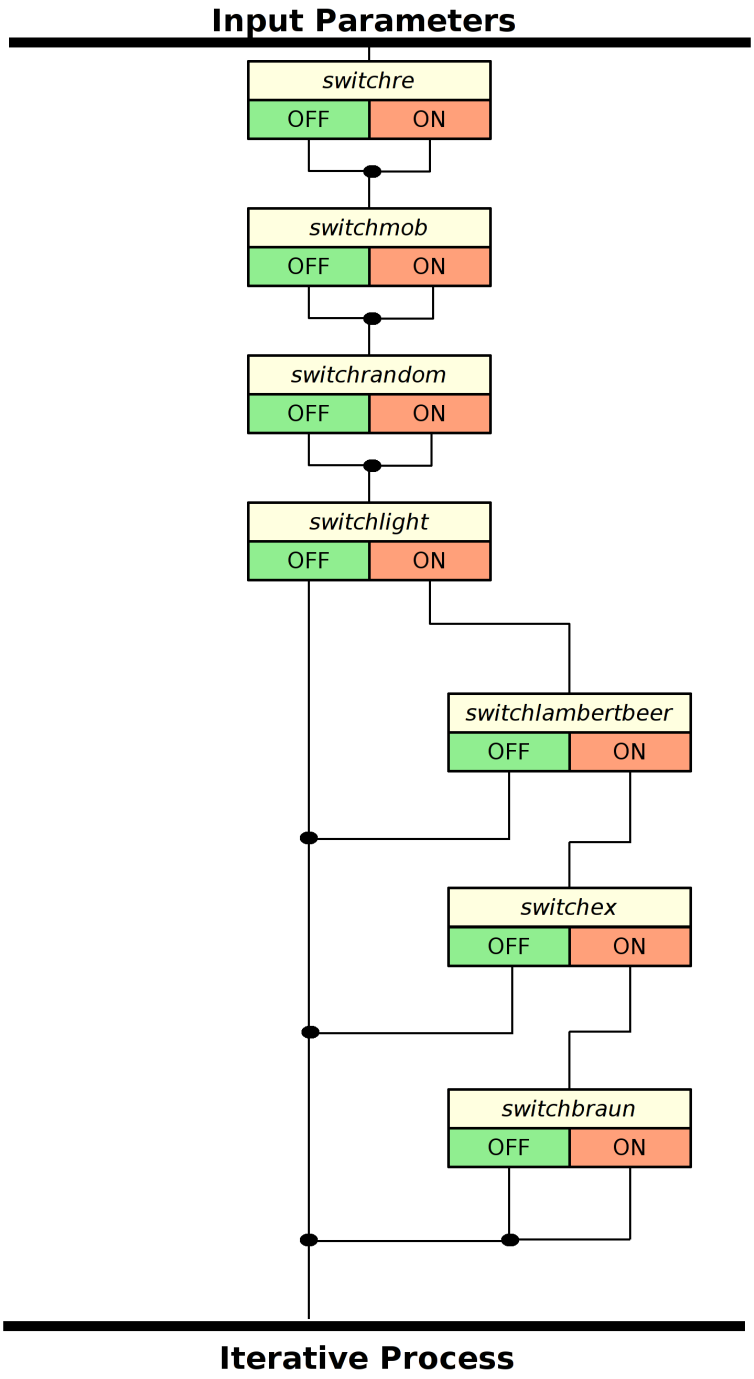

Figure 4.5: Flowchart displaying the interplay of the used switches. Summary of the icon labeled *Switches* in Fig. 4.4

From Fig. 4.3 it can be seen that some switches are only relevant if others are turned

on, for instance, if $switchlight = 0$, $switchex$ does not play any role because $\Phi_{i,j} = 0$ anyway. This interplay of switches shown in Fig. 4.5, refers the the icon $Switches$ in Fig. 4.4.

The complete iteration scheme, schematically shown in Fig. 4.4, mainly consists of two iterative cycles. After reading-in the input parameters and checking the setting of the switches, the Poisson equation is solved iteratively. We continue by updating the field-dependent variables, i.e., the mobilities, and therefore k_r, and the exciton dissociation rate constant, and then we also solve the set of continuity equations iteratively. If the solutions of the Poisson equation and the drift-diffusion equations are self consistent, the next time step is performed. Otherwise, the whole set consisting of the Poisson equation and the drift-diffusion equations is solved again, until self-consistency is reached. This inner part of the whole iteration cycle is surrounded by a dashed line in Fig. 4.4. After a particular number of performed time steps, the solution will reach the steady state, and the relevant output data (particle densities, current densities, generation profiles, mobility profiles, potential distribution and electric-field) are saved. Now the whole process can be started again with different input data, for instance with different applied voltages V_a, to finally gain an I-V curve.

5 Simulation results

This chapter is separated into three parts: First we investigate the influence of different effects on the shape of the I-V characteristic by studying a flat interface structure to exclude morphological effects. Based on the knowledge gained, we study the influence of a comb-like structure on the I-V characteristic and additionally briefly discuss photocurrent characteristics for the P3HT / PCBM-C61 system, which represents an organic-organic solar cell. In the last section we will discuss the different generation profiles in detail, obtained by the simulations presented before.

5.1 Flat interface

First, we investigate which effects determine the particular shape of the I-V curve. For this purpose, we make use of the different *switches* introduced in Sec. 4.4 and turn them on one after another to see the outcome of these effects. A flat interface (Fig. 5.1) was chosen to reduce the system to the simplest morphological case. For a detailed study on morphological effects on the I-V characteristic see [2]. As sample polymer P3EBT was chosen with the material parameters listed in Tab. 4.1. The different switch configurations are summarized in Sec. 5.1.1.

The second part of the flat interface study, Sec. 5.1.2, deals with the use of the three different polymers introduced in Sec. 2.3.3, i.e. P3HT, P3EBT and F8T2.

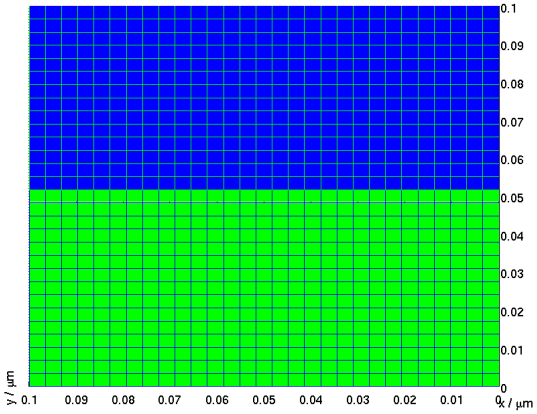

Figure 5.1: Morphology of the active layer for the flat interface structure consisting of an acceptor (blue) and a donor (green).

5.1.1 Switch settings

Every subsection will begin with a table demonstrating the switch settings used, as introduced in Fig. 4.3. The input data is in the default configuration for P3EBT and CIS, with the already introduced parameters summarized in Sec. 4.4, if not mentioned otherwise. Further, the corresponding I-V characteristic is shown and discussed.

5.1.1.1 Switch setting 1

Table 5.1: Switch setting 1.

switch	status
switchlight	0
switchlambertbeer	0
switchre	0
switchmob	0
switchex	0
switchbraun	0
switchrandom	0

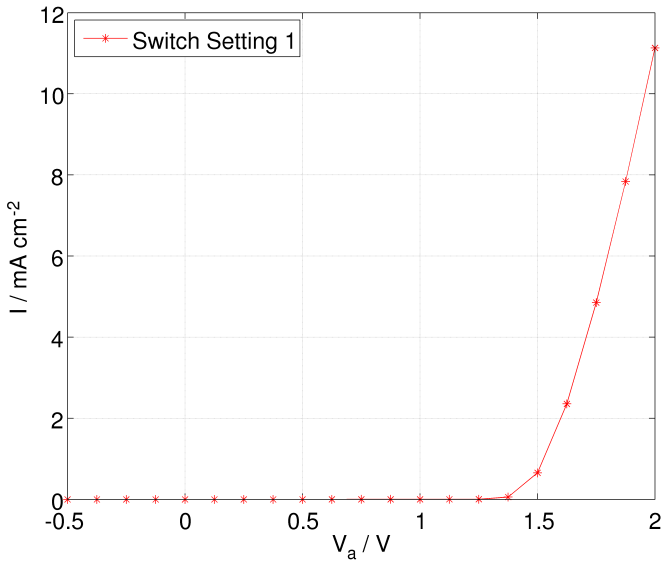

Figure 5.2: I-V characteristic with default settings and switch configuration shown in Tab.5.1.

Because of the *switchlight* = 0 setting, the I-V curve in Fig. 5.2 represents the dark case. No generation of particles takes place in the whole operating mode, thus the

current for voltages significantly lower than the built-in voltage ($V_{bi} = E_{gap} = 1.5$ eV for P3EBT/CIS), equals zero. The reason for the current rising slightly before reaching the built-in voltage is due to diffusional processes, which means that some electrons have enough energy to overcome the band gap barrier.

5.1.1.2 Switch setting 2

Table 5.2: Switch setting 2.

switch	status
switchlight	1
switchlambertbeer	0
switchre	0
switchmob	0
switchex	0
switchbraun	0
switchrandom	0

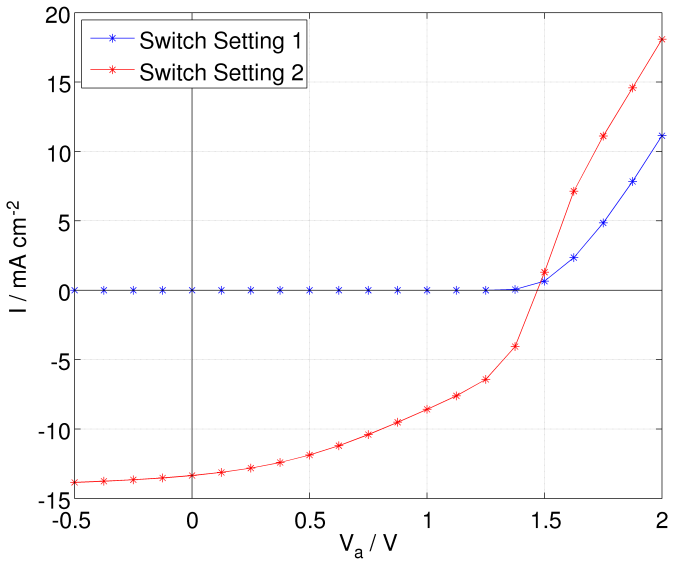

Figure 5.3: I-V characteristic with modified settings (Eq. (5.2)) and switch configuration shown in Tab. 5.2 (red line). The blue curve represents the dark case, i.e. $switchlight = 0$.

The red curve in Fig. 5.3 displays the I-V characteristic for the illuminated case. The results are based on the switch setting given in Tab. 5.2, but with a modification of

$switchex = 0$ from

$$\begin{aligned} x_{i,j} &= 0 \\ G_{i,j}^{(n,p)} &= \Phi_{i,j} \ \forall i,j : mask_{i,j} = 1 \\ G_{i,j}^{(n,p)} &= 0 \ \forall i,j : mask_{i,j} = 0, \end{aligned} \tag{5.1}$$

to

$$\begin{aligned} x_{i,j} &= 0 \\ G_{i,j}^{(n,p)} &= \Phi_{i,j} \ \forall i,j. \end{aligned} \tag{5.2}$$

Thus, electrons and holes are generated in the whole device.

The I-V characteristic of the illuminated case saturates for negative applied voltages to a constant current value. It rises earlier than the dark current since there are more electrons and holes within the device. Because of the higher electron and hole densities, the diffusional current also sets on earlier. The region with a maximum slope observed in the illuminated characteristic is due to a rapid increase of the current in the region of the open circuit voltage. At a particular voltage electrons can overcome the energetic LUMO barrier. At higher voltages, the slope decreases, because the energy of electrons is sufficiently high, that they do not actually feel the barrier.

5.1.1.3 Switch setting 3

Table 5.3: Switch setting 3.

switch	status
switchlight	1
switchlambertbeer	1
switchre	0
switchmob	0
switchex	0
switchbraun	0
switchrandom	0

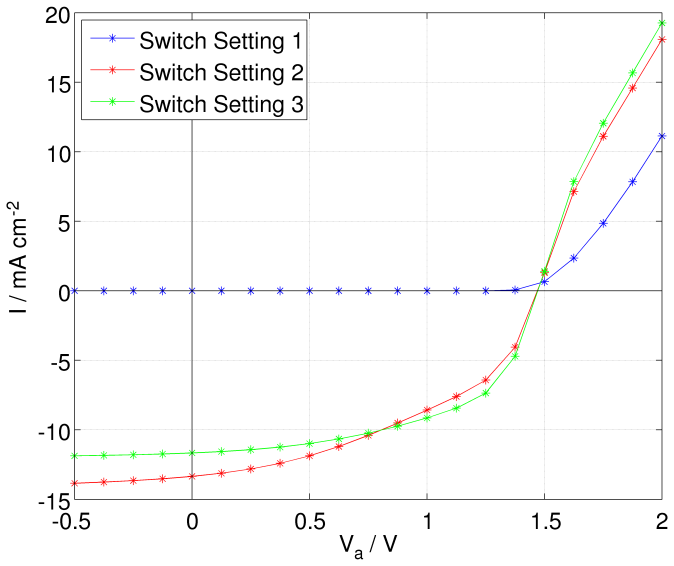

Figure 5.4: I-V characteristic with modified settings (Eq. (5.2)) and switch configuration shown in Tab.5.3 as well as switch configuration shown in Tab. 5.2. The third curve represents the dark case, i.e. $switchlight = 0$.

By introducing Lambert-Beer's law, i.e. $switchlambertbeer = 1$, we observe some interesting effects. The difference in the I-V curve (Fig. 5.4) resulting from including Lambert-Beer's law can be explained by considering that the generation profile decays exponentially to the cathode. Thus, there are fewer particles generated generally and, there are fewer particles generated in the inorganic layer, which is situated next to the cathode. At negative voltages the cathode is charged negative but there are fewer particles to provide current. At higher positive voltages, the current also rises less steeply than without considering Lambert-Beer's law, because there are fewer particles at the interface contributing to diffusion. At voltages $V_a > V_{bi}$ (forward bias) the current is slightly higher because of the same reason reversed: There are fewer particles diffusing back at the interface. It should be noted that there is only a bandgap difference for electrons when using P3EBT. Therefore, these considerations can be reduced to electrons, in the case of P3EBT only, because for holes the generalized potential equals the electrostatic potential, i.e.

$$^{p}\Psi_{i,j} \stackrel{!}{=} \psi_{i,j} \text{ or } \Theta^{p}_{i,j} \stackrel{!}{=} 0 \ \forall i, j.$$

A very interesting effect is the later on-set of the increase of the illuminated curve than in the $switchlambertbeer = 0$ case. This can be explained by the fact that there are

more holes next to the anode than there would be by assuming that the absorption is constant over the device (see Fig. 5.5).

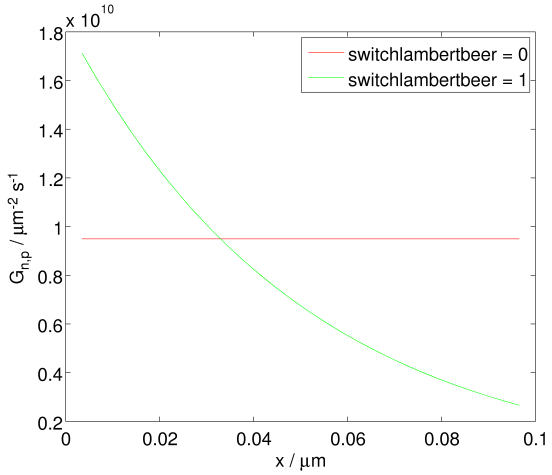

Figure 5.5: Illumination profile for $switchlambertbeer = 0$ and $switchlambertbeer = 1$.

Another interesting question might be, if this on-set is tunable by changing the $\epsilon_r^{inorganic} : \epsilon_r^{organic}$ ratio. The current rises with the electric field strength. Thus, if $\epsilon_r^{inorganic} \gg \epsilon_r^{organic}$, it follows that $|\mathbf{E}^{organic}| \gg |\mathbf{E}^{inorganic}|$ because of the relation $\epsilon_1 E_1 = \epsilon_2 E_2$.

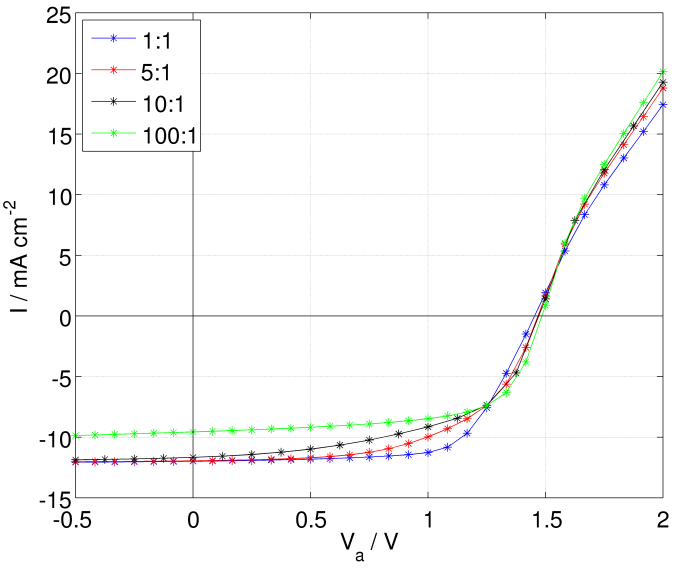

Figure 5.6: Dependence of the shape of the I-V curve on the ratio of $\epsilon_r^{inorganic} : \epsilon_r^{organic}$ with $switchex = 0$ condition modified according to Eq. (5.2).

In Fig. 5.6 it can be seen that at higher $\epsilon_r^{inorganic} : \epsilon_r^{organic}$ ratios the current in the negative regime is lower. This can be explained by the fact that the electric field in the inorganic layer is smaller and therefore more holes are diffusing to the cathode, lowering the current. In the positive regime the current is slightly increased, because now the barrier can be overcome and the field is higher in the organic region. Therefore, also the onset-voltage decreases with rising ϵ ratios and therefore also the gradient, i.e. the slope of the I-V curve, decreases.

Now taking the default $switchex = 0$ condition, i.e. particles are only generated in the inorganic material, the resulting curves, as a function of ϵ_r, change significantly.

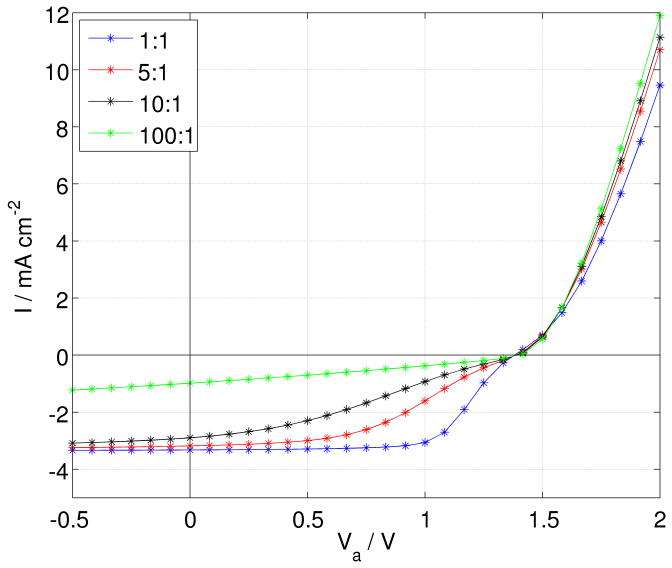

Figure 5.7: Dependence of the shape of the I-V curve on the ratio of $\epsilon_r^{inorganic} : \epsilon_r^{organic}$ with default $switchex = 0$ condition.

First of all, the current is much lower. This can be explained by the fact that there are fewer particles within the device due to the default $switchex = 0$ setting. Second, the current is not rising steadily, there is a saturation observed at $V_a \approx V_{bi}$. At this point almost the same number of electrons is diffusing back to the cathode as holes are drifting towards the cathode, thus these contributions to the complete current cancel out[1]. However, there are almost no electrons in the organic layer, therefore no remarkable electronic current contribution in this direction is observed, which would give the I-V curve the characteristic form seen in Fig. 5.6. The dependence on the ϵ_r ratio is the same as discussed previously.

[1]This effect was also experimentally observed by Uhrich *et al.* [32] and will also be discussed in Sec. 5.1.2.1.

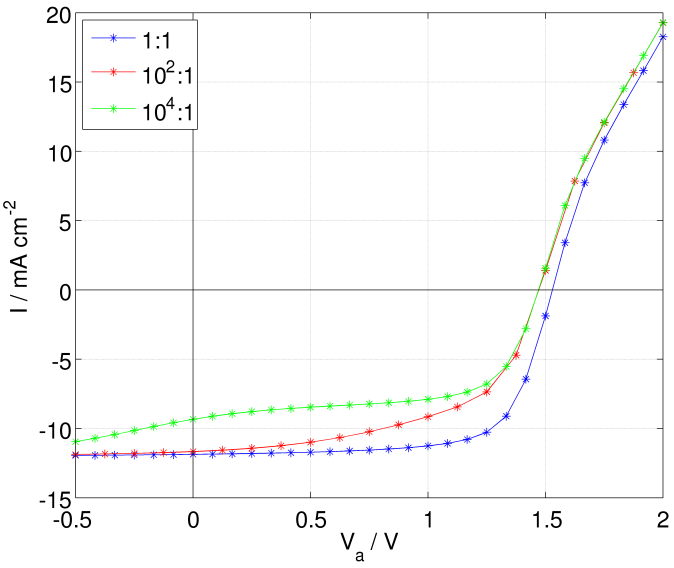

Figure 5.8: Influence of the inorganic mobility $\mu_0^{inorganic}$ on the shape of the I-V curve for three different mobilities with setting shown in Tab. 5.3 and $switchex = 0$ setting modified according to Eq. (5.2).

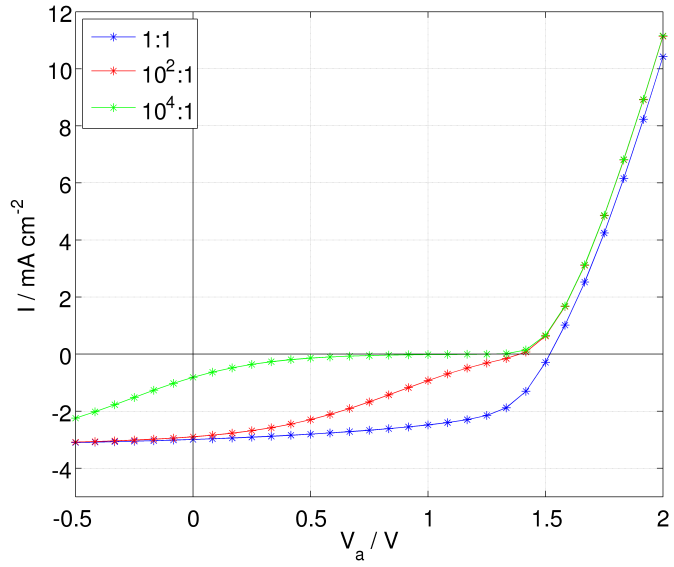

Figure 5.9: Influence of the inorganic mobility $\mu_0^{inorganic}$ on the shape of the I-V curve for three different mobilities with setting shown in Tab. 5.3 and default $switchex = 0$ setting.

All curves discussed so far were calculated under the assumption that the mobilities of electrons and holes are higher by a factor 100 in the inorganic material than in the organic layer. This assumption seems plausible because generally inorganic charge carrier mobilities are much higher than the organic mobilities. Now we will investigate the influence of changing the mobility in the inorganic layer on the I-V characteristic under the assumption that the inorganic mobility can not be smaller than the organic one (Fig. 5.8 and Fig. 5.9).

For the modified $switchex = 0$ setting, the current increases in the positive regime with higher inorganic mobility. However, the maximum power point and the current in the negative regime is higher for smaller mobilities. This can be explained by considering that for applied voltages lower than the built-in voltage, the cathode is charged positive and electrons are drawn to the cathode and holes to the anode. However, the mobility in the inorganic layer is much higher than in the organic layer and therefore particles diffuse preferably in the inorganic layer, where they propagate with a velocity by a factor 100 or even 10000 faster than in the other region. Therefore, there are significantly more holes diffusing in the same direction as the electrons and, therefore, lowering the current. If the mobilities do not differ in the different regions, there is no primarily-preferred diffusion direction and the motion of the particles is, basically, dominated by the drift term. Of course a local preference for a particular direction can occur due to a gradient in the particle densities but there are no different intrinsic conditions *a priori*.

From Fig. 5.9 one can see that with higher inorganic mobilities, the plateau containing the plateau observed in Fig. 5.7 gets broader, while it even disappears for the case $\mu_0^{inorganic} = \mu_0^{organic}$. The interpretation of this behavior of the characteristics is the same as above: A mobility change at the interface generates a preferred diffusion direction. This happens in various steps, first, particles reaching the interface accelerate immediately and are, thus, drawn off the interface. The lack of particles at the interface induces a gradient in the density leading to diffusion. Furthermore, particles near the inorganic layer already feel the higher mobility, and prefer this direction, which is quite obvious because in our model we take the mobilities $\mu_{i+\frac{1}{2},j}$ to simulate the drift as well as the diffusional transport, Eqs. (4.31)-(4.34)).

The only major difference between the curves shown in Fig. 5.8 and Fig. 5.9 is that for the second case the plateaus are shifted to zero current. This is due to band gap diffusion effect discussed above for different ϵ_r ratios at default $switchex = 0$ setting (Fig. 5.7).

5.1.1.4 Switch setting 4

Table 5.4: Switch setting 4.

switch	status
switchlight	1
switchlambertbeer	0
switchre	1
switchmob	0
switchex	0
switchbraun	0
switchrandom	0

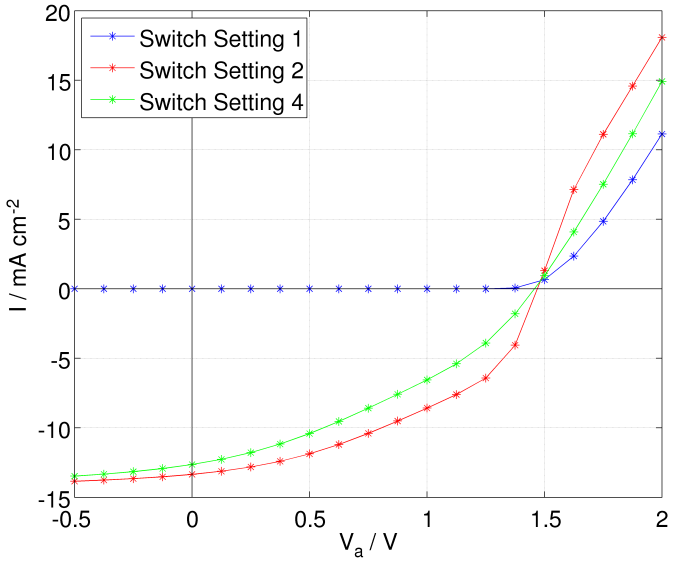

Figure 5.10: I-V characteristic with modified settings (5.1.1.2) and switch configuration shown in Tab.5.4 as well as switch configuration shown in Tab. 5.2. The third curve represents the dark case, i.e. $switchlight = 0$.

Considering recombination processes of electrons and holes (excitons do not exist due to $switchex = 0$) has the expected effect of slightly reducing the current all over the voltage regime. Particle densities are reduced by the bimolecular recombination process and, hence, there are fewer particles available contributing to the current. One interesting detail, which has to be highlighted at this point, is that because of equal loss of both kinds of charged particles the kink in the illuminated I-V characteristic, as seen in all calculations before, vanishes.

One question arising is, why the increase of the illuminated current sets on earlier than in Sec. 5.1.1.3. The reason is that in this case we lose particles equally distributed over the device, while in the case of *switchlambertbeer* = 0 the generation rate decreases exponentially, being highest at the anode and being there higher than in the *switchlambertbeer* = 0 case (Fig. 5.5). Thus there are more particles generated next to the anode, moving in the corresponding direction.

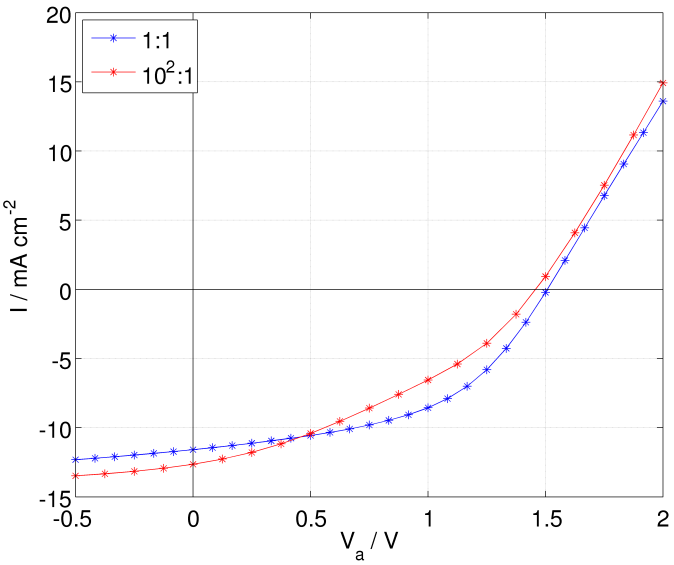

Figure 5.11: Influence of the mobility ratio $\mu_0^{inorganic} : \mu_0^{organic}$ on the shape of the I-V curve. The switch configuration is shown in Tab. 5.4 and modified *switchex* = 0 settings according to Eq. (5.2) are used.

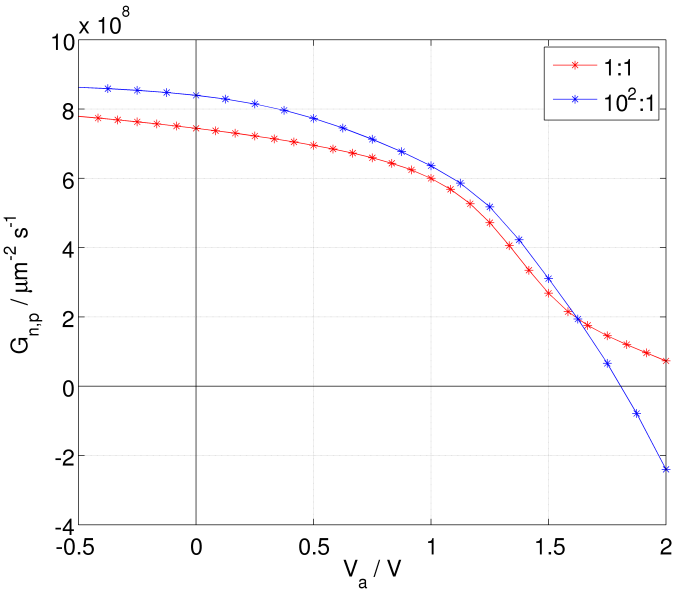

Figure 5.12: Influence of the mobility ratio $\mu_0^{inorganic} : \mu_0^{organic}$ on the average generation rate. Settings as in Fig. 5.11

One interesting topic is the influence of the mobility on the I-V curve (Fig. 5.11) because the recombination rate is directly proportional to the sum of the mobilities, see Sec. 3.5.1.4 . It has to be emphasized at this point that the result we get is quite remarkable, because we observe an increase of the short circuit voltage with decreasing $\mu_0^{inorganic}$ values. This is in contrast to the result obtained in Sec. 5.1.1.3. The recombination effect, being proportional to the mobility, lowers the short circuit current for lower mobilities because the recombination loss of particles is larger in the case of equal mobilities in the whole device (Fig. 5.12 shows the average generation rate, $\overline{\Gamma}_n = \frac{1}{N}\sum_{i,j}\Gamma_{i,j}$, where N denotes the total number of grid-points). This means that the net-generation rate is smaller, because charge carriers remain longer in the device. There is also no preferred diffusion direction, and, therefore, there are fewer particles within the device contributing to the current. However, after passing the built-in voltage, the recombination rate gets larger for the higher $\mu^{inorganic}$ case because at this voltage more particles cross the barrier and the diffusional advantage is negligible.

5.1.1.5 Switch setting 5

Table 5.5: Switch setting 5.

switch	status
switchlight	1
switchlambertbeer	0
switchre	0
switchmob	1
switchex	0
switchbraun	0
switchrandom	0

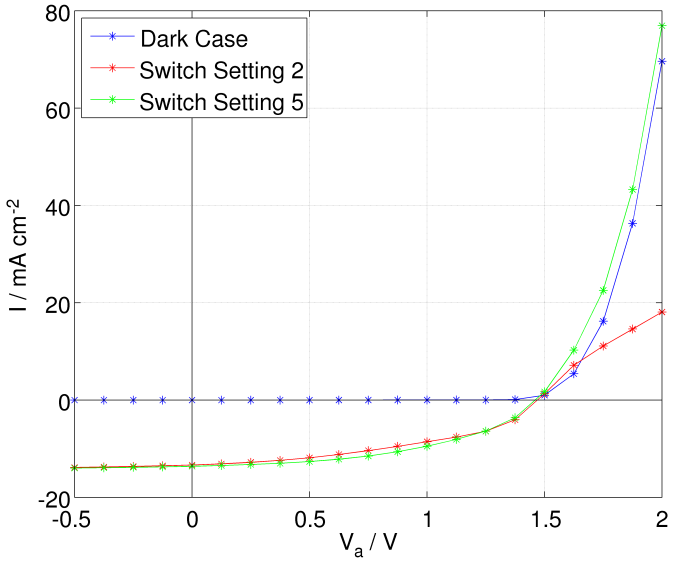

Figure 5.13: I-V characteristic with modified settings (5.1.1.2) and switch configuration shown in Tab.5.5 as well as switch configuration shown in Tab. 5.2. The third curve represents the dark case, i.e. *switchlight* = 0.

The first quite obvious changes in the curve are, that, as in Sec. 5.1.1.4 the kink in the illuminated I-V curve is not observed again, and the current, dark as well as illuminated, rises much faster than before. This can be explained by the fact that with higher positive voltages, the locally occurring field strengths and, therefore, the mobilities, which are proportional to the current density, increase. Also in the negative regime the current is slightly larger than in the calculation without consideration of field-dependent mobilities. This can be explained by the fact that the current is limited by the charge carrier

extraction from the contacts.

5.1.1.6 Switch setting 6

Table 5.6: Switch setting 6.

switch	status
switchlight	1
switchlambertbeer	0
switchre	0
switchmob	0
switchex	0
switchbraun	0
switchrandom	1

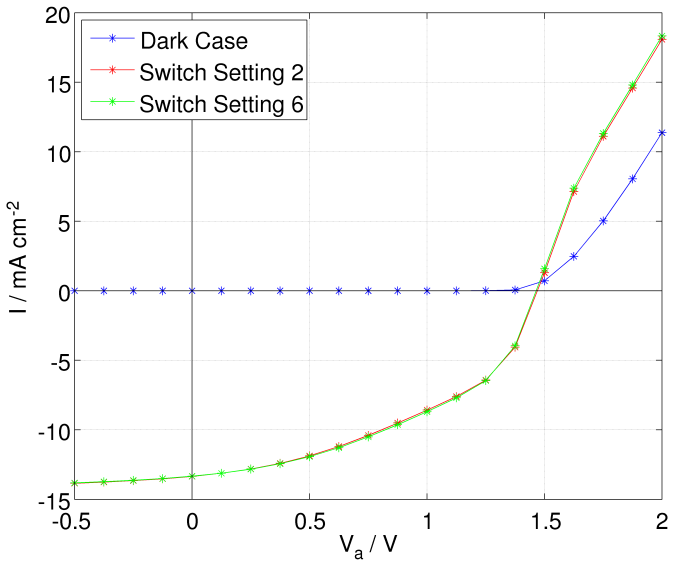

Figure 5.14: I-V characteristic with modified settings (5.1.1.2) and switch configuration shown in Tab.5.6 as well as switch configuration shown in Tab. 5.2. The blue curve represents the dark case, i.e. $switchlight = 0$.

In this case, the HOMO/LUMO levels of the inorganic material are randomly distributed around the exact value of 0.05 eV (Fig. 5.15):

$$\Theta_{i,j}^{(n,p)} = \begin{cases} \Theta_{i,j}^{(n,p)} & \text{if} \quad mask_{i,j} = 0 \\ \Theta_{i,j}^{(n,p)} + 0.05 rand_{-1,1} & \text{if} \quad mask_{i,j} = 1. \end{cases} \tag{5.3}$$

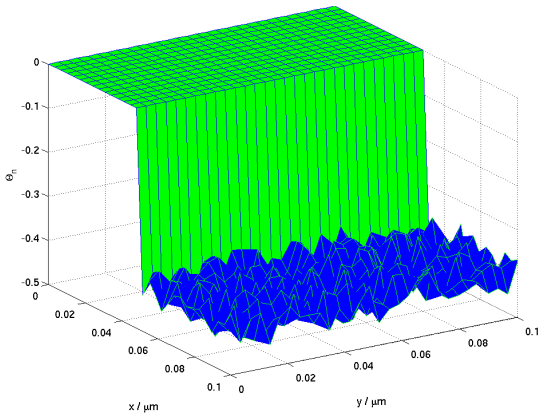

Figure 5.15: Illustration of the transport level distribution for electrons, Θ_n, for random distributed transport levels.

The motivation for this consideration is that experimentally the inorganic layer, CIS, is actually not continuous, but consists of CIS nanoparticles [22]. However, it is very dense, so that it is justified to regard it as a continuous layer in the theoretical model, but to account for the problem of continuous HOMO/LUMO levels, this approach can be chosen as well. Nevertheless, this effect does not change the characteristic curve significantly. In contrast to the characteristic, the electron and hole density profiles change, Fig. 5.16, because the randomly distributed deviations from the smooth transport levels act as traps.

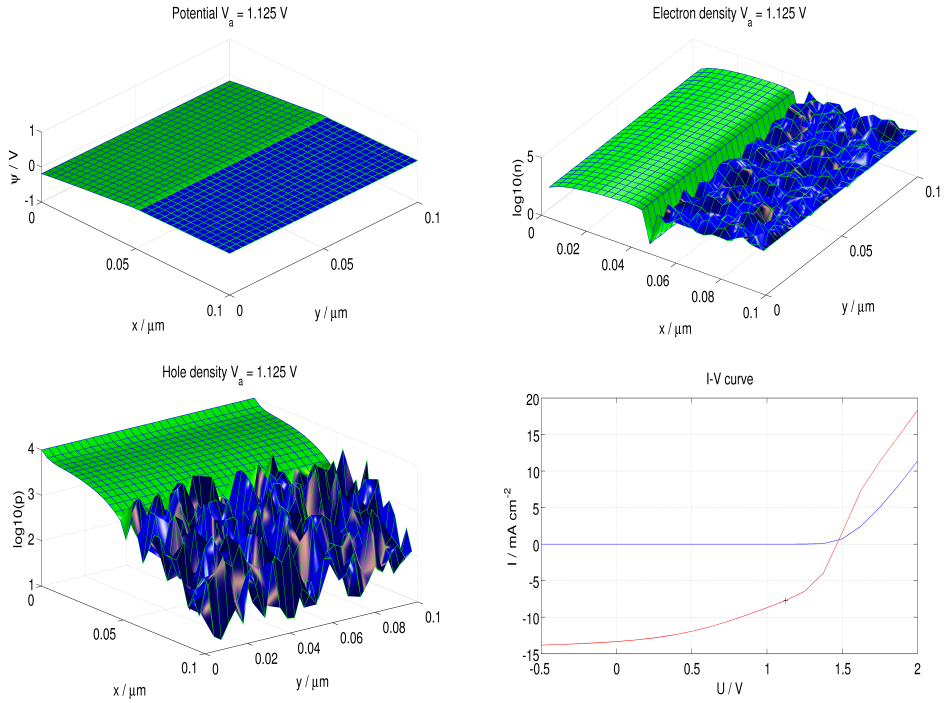

Figure 5.16: Potential (upper left panel), electron density (upper right panel) and hole density (lower left panel) corresponding to $V_a = 1.125$ V and I-V curve (lower right panel) resulting from the switch configuration shown in Tab. 5.6.

The deviations from the regular transport levels are the same for electrons and holes, Fig. 5.15. Nevertheless, in Fig. 5.16 it can be seen that at this particular voltage, i.e $V_a = 1.125$ V, holes are slightly better trapped than electrons. This effect occurs due to the high applied voltage which pushes electrons to the cathode and holes to the anode. The mobility in the inorganic layer (blue in Fig. 5.16) is much higher than in the organic region and therefore, holes trapped in the inorganic layer have to overcome the energetic barrier (in form of deviations of the default $\Theta_{(n,p)}$ values) as well as the *'diffusional barrier'* to the organic region (given by the mobility difference as discussed in Sec. 5.1.1.3).

The loss of electrons at the interface, seen in Fig. 5.16 (upper right panel), is not due to recombination effects, because these were not considered in this calculation. It is solely due to higher mobilities at the neighboring points (inorganic layer) and the bandgap off-set. Thus, electrons move immediately in the inorganic layer as soon as they come close to it, driven by diffusion, the electric field and the particular material

intrinsic HOMO/LUMO levels.

5.1.1.7 Switch setting 7

Table 5.7: Switch setting 7.

switch	status
switchlight	1
switchlambertbeer	1
switchre	1
switchmob	1
switchex	0
switchbraun	0
switchrandom	0

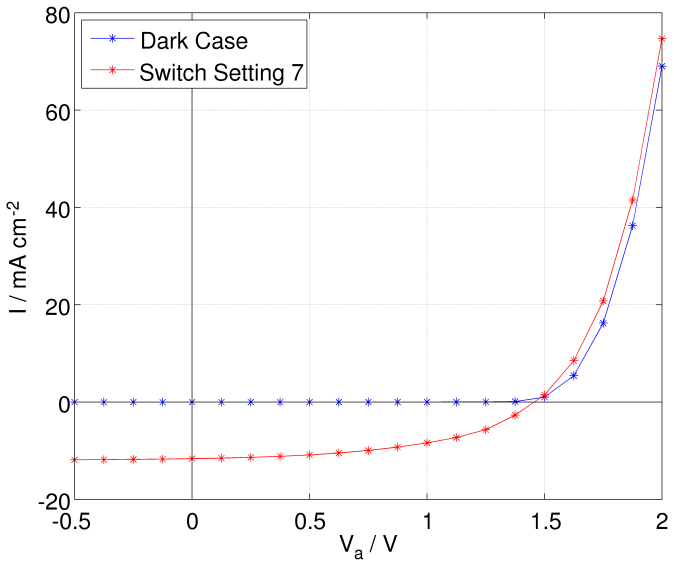

Figure 5.17: I-V characteristic with modified settings (Sec. 5.1.1.2) and switch configuration shown in Tab.5.7. The blue curve represents the dark case, i.e. *switchlight* = 0.

Setting all switches discussed in the previous sections to 1, except *switchrandom*, yields, as expected, a combination of these effects. There is no kink in the illuminated curve observed, and the dark as well as the illuminated curve rise quite rapidly with increasing voltages. The processes explaining the particular form of the I-V characteristic are discussed in Sec. 5.1.1.1 - Sec. 5.1.1.6.

5.1.1.8 Switch setting 8

Table 5.8: Switch setting 8.

switch	status
switchlight	1
switchlambertbeer	0
switchre	0
switchmob	0
switchex	1
switchbraun	0
switchrandom	0

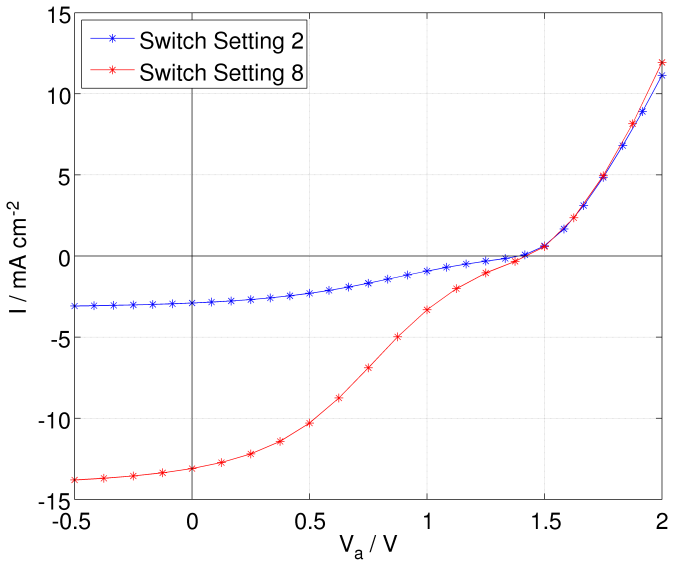

Figure 5.18: I-V characteristic with switch configuration shown in Tab.5.8 as well as switch configuration shown in Tab. 5.2 with default $switchex = 0$.

In this study we consider exciton diffusion as well as field-dependent charge carrier generation rates according to Onsager, [7], and Buxton, [4]. The rate expression of [4], given by Eq. (3.40), corresponds to a process solely described by the dissociation constant, a treatment commonly employed in chemical kinetics. Comparing the gained I-V characteristic with the corresponding curve without consideration of excitonic processes, Fig. 5.18, one observes, first that the current for the negative regime is much lower for the latter case. The reason for this effect is that at low, i.e. high negative, voltages, the electric field strength is sufficiently high to separate excitons to electrons and holes in

the organic region, although there is also only a steady charge carrier generation in the inorganic region. Therefore, this part of the curve is comparable to the curves obtained with $switchex = 0$ settings modified according to Eq. (5.2). With voltages approaching the built-in voltage, the occurring field strength decreases and therefore also the amount of generated charge carriers. In this part of the I-V curve (Fig. 5.18) we obtain the same situation as already seen in the curves for default $switchex = 0$ settings. Moreover, electrons and holes move in the same direction and, hence, the separate parts of the electron- and hole-current cancel out. Increasing the voltage, increases the field strength further and thus also the efficiency of exciton separation rises.

To see this effect of field-dependent generation of charge carriers in a more detailed way, a calculation was performed without an inorganic region, i.e. the whole solar cell consists of P3EBT,

$$mask_{i,j} = 0 \; \forall \; i, j,$$

across which excitons are assumed to dissociate field-assisted. Nevertheless, an E_{gap} of 1.5 eV was assumed [2].

To see the sole effect of a change of the ϵ_r-ratio on the field-dependent generation rate another calculation was performed. In this calculation it was assumed that there is, although without an inorganic region, i.e. no transport level difference and no mobility difference, a difference in ϵ_r as in the default inorganic case. Of course, this scenario is not very realistic; however, it allows us to study the direct influence of ϵ_r-dependent change of the electric field on the charge carrier generation rate (Fig. 5.19), because there is no constant contribution to the generation rates (no inorganic part).

[2] This approached can be regarded as an *effective medium* approach as also performed by, for instance, Koster [5], Deibel [33] *et al.*.

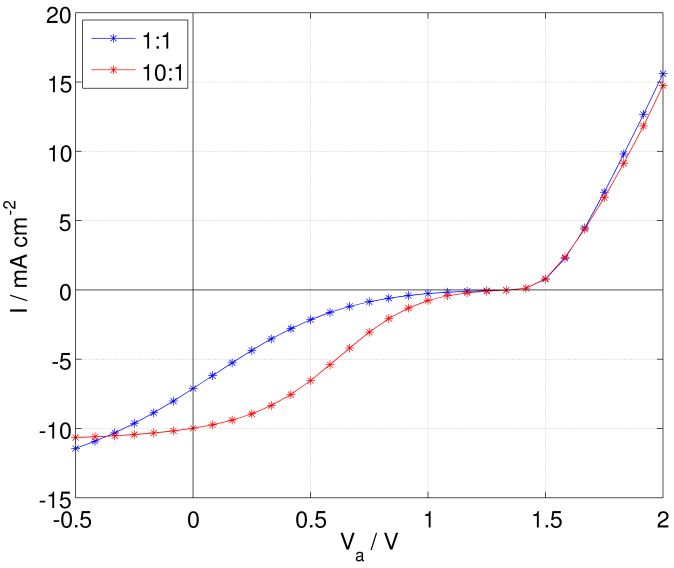

Figure 5.19: I-V curve for the switch configuration shown in Tab. 5.8 and the ϵ_r ratios $1:1$ and $10:1$. The inorganic region was not considered in this case. A detailed description of the ϵ_r consideration can be found in the text.

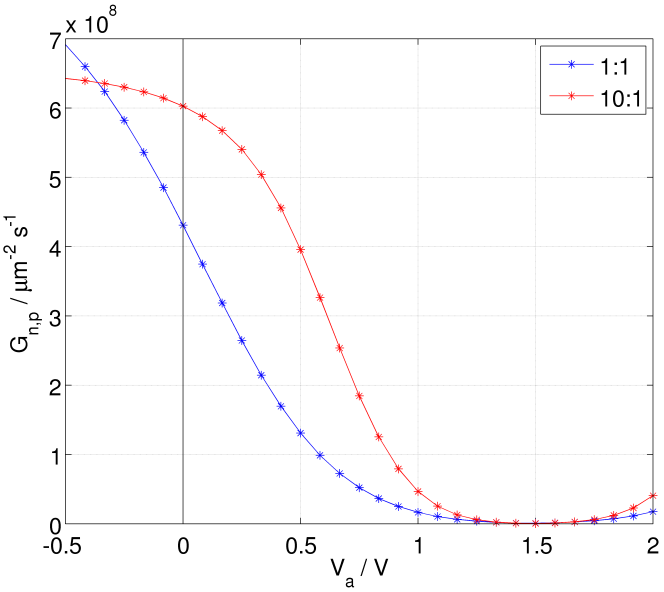

Figure 5.20: Average generation rate for switch configuration shown in Tab. 5.8 and the ϵ_r ratios $1:1$ and $10:1$. The inorganic region was not considered in this case. A detailed description of the ϵ_r consideration can be found in the text.

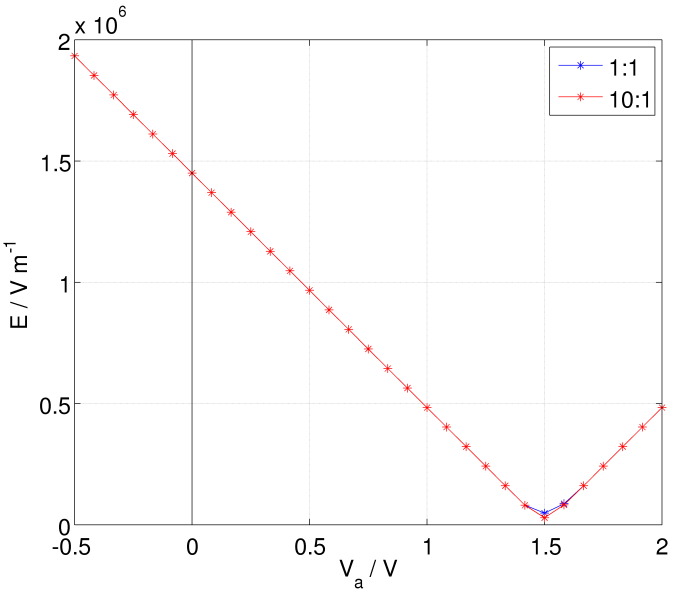

Figure 5.21: Average field strength for switch configuration shown in Tab. 5.8 and the ϵ_r ratios 1 : 1 and 10 : 1. The inorganic region was not considered in this case. A detailed description of the ϵ_r consideration can be found in the text.

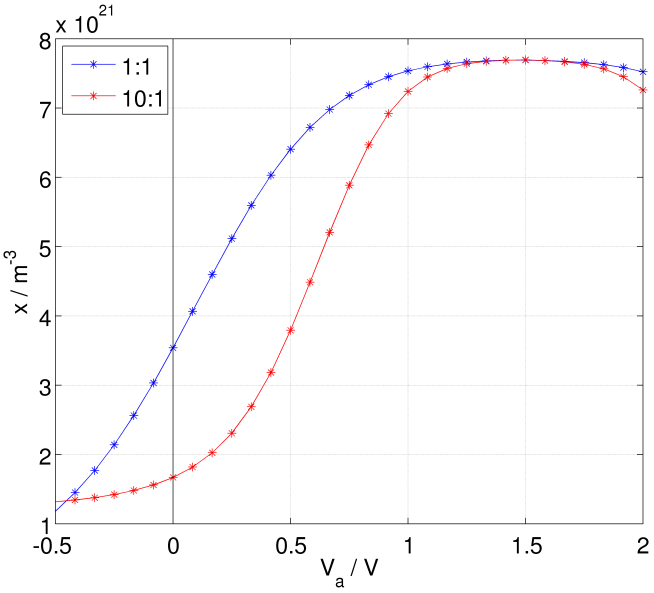

Figure 5.22: Average exciton density for switch configuration shown in Tab. 5.8 and the ϵ_r ratios 1 : 1 and 10 : 1. The inorganic region was not considered in this case. A detailed description of the ϵ_r consideration can be found in the text.

From Fig. 5.19 it is obvious that the current reaches a plateau in the region of the built-in voltage. This plateau is unambiguously caused by the minimal field strength and therefore minimal generation rate (compare Figs. 5.19-5.22). This is also the reason for the occurrence of a maximum in the average exciton density, Fig. 5.22. Furthermore, the plateau associated with the saddle point is much narrower for the case with an $\epsilon_r = 10$ region, Fig. 5.19, because also smaller changes in the applied voltage induce a large electric field, due to the continuity condition $\epsilon_1 E_1 = \epsilon_2 E_2$. Of course, the average electric field strength, $\overline{E} = \frac{1}{N}\sum_{i,j} E_{i,j}$ with N denoting the number of grid points, observed at a particular applied voltage is for both cases almost the same (Fig. 5.21). A remarkable fact is that the average field is even at $V_a = V_{bi}$ not equal to zero and that it differs slightly for the two different cases. This is due to a potential induced by charge carrier densities being not equal zero at this point. At higher applied voltages the average electric field strength is in a range in which local occurring particle densities do not have such a strong influence on the potential surface. The deviations of the average field distributions in the scale of $|V_a - V_{bi}| \lessapprox 0.3$ V are due to the different particle densities induced by different ϵ_r values.

Another interesting effect is that the generation rate for very small values of applied voltages is profoundly smaller for the continuous ϵ case, Fig. 5.20, although the average field strength is approximately the same for both cases at these voltages. To reach high generation rates at these voltages, a continuous field distribution is desirable because, in the other case, the high field domain is in a region in which almost all excitons are separated. Thus, increasing the field has only a marginal effect, while in the low-field region the field is too small, and increases too slowly. In the $\epsilon_r^1 : \epsilon_r^2 = 1 : 1$ case there are more particles generated. This effect can be estimated mathematically by

$$\overline{E} \approx \frac{\Delta\psi}{l}, \tag{5.4}$$

where $\overline{E}$ denotes the average field strength, $\Delta\psi$ the potential difference between cathode and anode, and l the device length. Using the relation

$$\epsilon_1 E_1 = \epsilon_2 E_2 \tag{5.5}$$

and assuming that the average field is given by

$$\overline{E} = \frac{E_1 + E_2}{2}, \tag{5.6}$$

i.e. both regions have exactly the same extensions. Now we can conclude that

$$\frac{\Delta\psi}{l} \approx \frac{E_1}{2}\left(1+\frac{\epsilon_1}{\epsilon_2}\right), \tag{5.7}$$

or by solving for E_1

$$E_1 \approx \frac{2\Delta\psi}{l\left(1+\frac{\epsilon_1}{\epsilon_2}\right)}. \tag{5.8}$$

Inserting $\frac{\epsilon_1}{\epsilon_2} = 10$ into the obtained expression gives

$$E_1 \approx \frac{2}{11}\overline{E}. \tag{5.9}$$

Note that $\overline{E}$ is also the value we get for the field strength of the continuous ϵ case. For instance, if we assume $\Delta\psi = 2$ V and $l = 1\mu$m, which is one of the outermost points of the calculated voltage region, we get

$$\begin{aligned}\overline{E} &\approx 2\cdot 10^6 \text{ Vm}^{-1},\\ E_1 &\approx 3.6\cdot 10^5 \text{ Vm}^{-1},\\ E_2 &\approx 3.6\cdot 10^6 \text{ Vm}^{-1}.\end{aligned}$$

So in this case we are in a region, in which the exciton dissociation rate is rather high in the continuous ϵ case and in the layer with the lower ϵ value for the second case, while it is very low for the other layer (see Fig. 3.2). Hence, there are more charge carriers generated in the first scenario $(1:1)$ at this voltage.

Summarizing, it is possible to conclude that the plateau produced by the excitonic separation behavior is for small $\epsilon_r^{inorganic}$ values much broader than the plateau produced by the band-gap diffusion phenomenon, described in Sec. 5.1.1.3, at the same conditions.

5.1.1.9 Switch setting 9

Table 5.9: Switch setting 9.

switch	status
switchlight	1
switchlambertbeer	0
switchre	0
switchmob	0
switchex	1
switchbraun	1
switchrandom	0

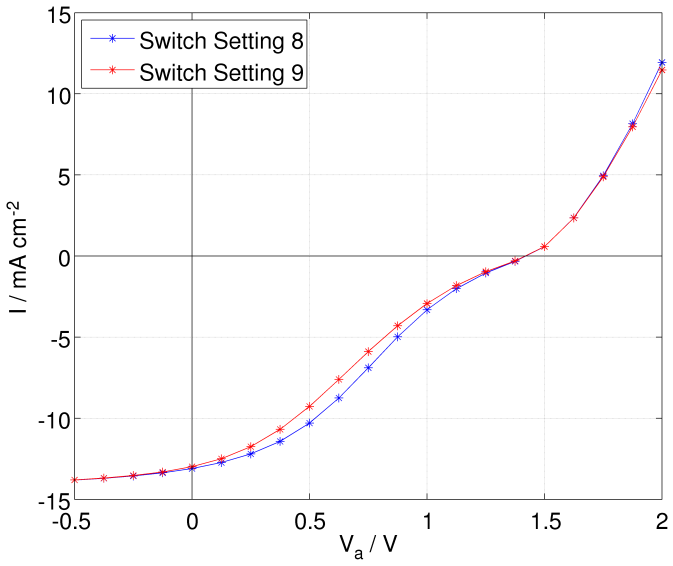

Figure 5.23: I-V characteristic with switch configuration shown in Tab.5.9 as well as switch configuration shown in Tab. 5.8.

Considering Braun's model of exciton dissociation results in a slight difference of the slope of the I-V characteristic compared to treating dissociation solely with the dissociation rate constant, Fig. 5.23. The deviations predicted by Braun's model can be understood by a closer inspection of Eq. (3.42). As a consequence of assuming a dissociation probability, excitons only dissociate to charge carriers immediately after being generated and thus more excitons are subjected to decay according to the exciton recombination rate, Eq. (3.43). In the other generation model, Eq. (3.40), no consideration of immediate dissociation is made primarily, because the rate only indicates the velocity

in which the process happens. Thus the future of the excitons, which do not dissociate immediately, is not determined *a priori* and remains insecure.

5.1.1.10 Switch setting 10

Table 5.10: Switch setting 10.

switch	status
switchlight	1
switchlambertbeer	1
switchre	1
switchmob	1
switchex	1
switchbraun	1
switchrandom	0

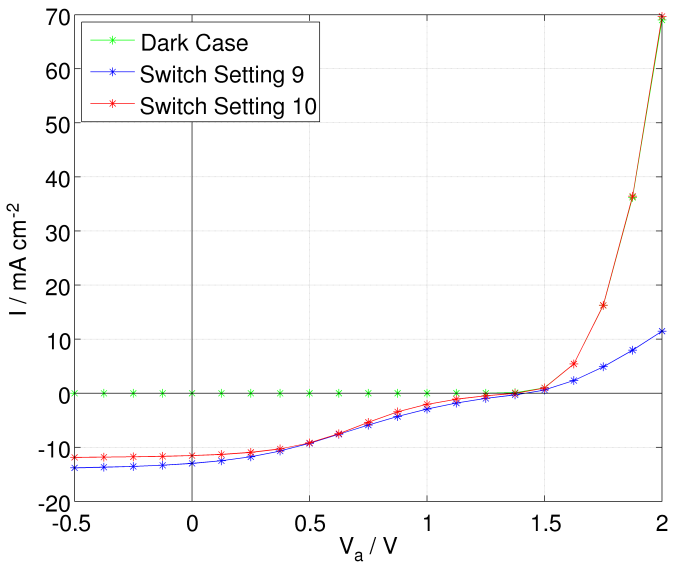

Figure 5.24: I-V characteristic with switch configuration shown in Tab.5.10, for illuminated as well as for the dark case, and switch configuration shown in Tab. 5.9.

Switching on all types of recombination and generation effects implemented results in an I-V characteristic, which can be understood in terms of all influences on the shape discussed in Sec. 5.1.1.1 - 5.1.1.9, Fig. 5.24. The rising current saturates at applied voltages $V_a \approx V_{bi}$ because of two different effects which overlap: First, electrons are

diffusing in the same direction as the holes. Thus the current cancels out, as discussed in Sec. 5.1.1.3. Second, by approaching the built-in voltage, the occurring electric field strength decreases and therefore also the number of generated charge carriers, as discussed in Sec. 5.1.1.8. In comparison to the curve given in Sec. 5.1.1.9, Fig. 5.23, the current increases much faster in the positive regime, because of field-dependent mobilities (see Sec. 5.1.1.5) while in the negative regime it is lower due to Lambert Beer's law and recombination effects (see Sec. 5.1.1.3 and Sec. 5.1.1.4). Furthermore, it is remarkable that there is almost no difference between illuminated and dark current in the positive regime, as already seen in Sec. 5.1.1.3 and Sec. 5.1.1.7.

An interesting question is the influence of change of the $\epsilon_r^{inorganic} : \epsilon_r^{organic}$ ratio on the shape of the curve because both effects responsible for the plateau are sensitive on the ϵ_r-ratio, as shown in Sec. 5.1.1.3 and 5.1.1.8, respectively.

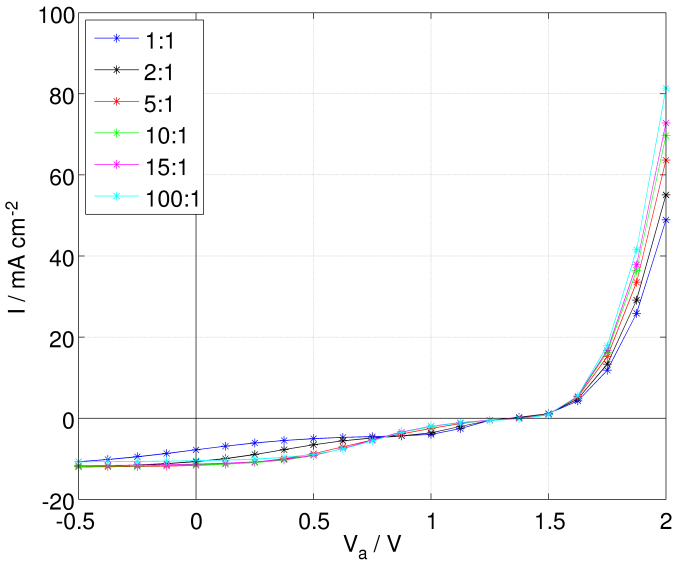

Figure 5.25: I-V characteristic with switch configuration shown in Tab.5.10, for different ϵ_r ratios.

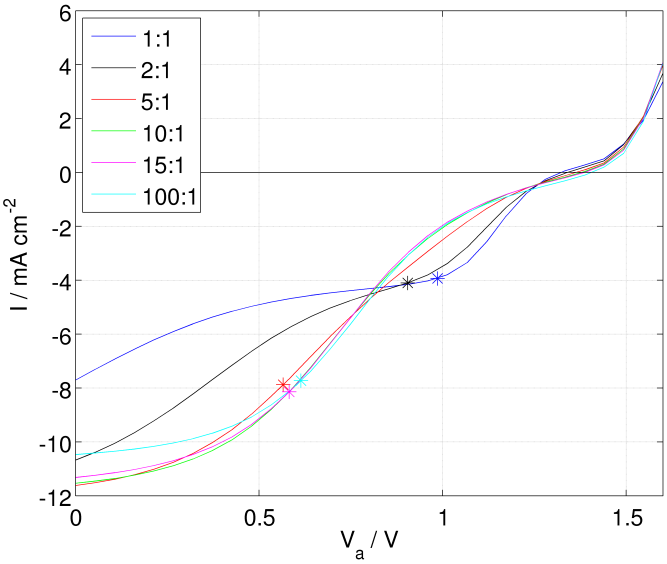

Figure 5.26: I-V characteristic with switch configuration shown in Tab.5.10, for different ϵ_r ratios with maximum power points indicated by an asterisk; closer view.

The band-gap diffusion process, see Sec. 5.1.1.3, shifts the on-set of the current-increase with higher ϵ_r ratios to higher negative voltages, while the exciton dissociation process shifts the onset to lower voltages, see Sec. 5.1.1.8. In Fig. 5.25 and Fig. 5.26 the overlap of both effects is shown. The exciton dissociation effect dominates and thus forces the curve with $\epsilon_r^{inorganic} : \epsilon_r^{organic} = 1 : 1$ to rise first and the curve $\epsilon_r^{inorganic} : \epsilon_r^{organic} = 100 : 1$ last. Note that there is almost no difference observable between the characteristics with $\epsilon_r^{inorganic} : \epsilon_r^{organic} = 100 : 1$ and $\epsilon_r^{inorganic} : \epsilon_r^{organic} = 15 : 1$. Then, at $V_a \gtrapprox 0$ V an interesting effect is observed: the curves with $\epsilon_r^{inorganic} : \epsilon_r^{organic} = 1 : 1$ and $\epsilon_r^{inorganic} : \epsilon_r^{organic} = 2 : 1$ reach a first plateau. This plateau is caused by the fact that, although there are almost no particles generated in the organic material in this voltage region, the electrons can propagate better than in the cases with higher ϵ_r ratios due to the particular slope of the potential surface. Thus, in this region, the two different effects coincide and force the I-V characteristic in a first plateau which is not observed for higher ratios. The second plateau, at $V_a \gtrapprox 1.2$ V is due to low charge carrier densities within the device because of field-dependent exciton dissociation rates. In the positive regime, at voltages above 1.5 V the current grows as usual.

Unsurprisingly, the occurrence of a second plateau for low ϵ_r ratios profoundly influences the values assigned to the maximum power point and the fill factor. Tab. 5.11 summarizes the calculated maximum power points and fill factors for the characteristics

shown in Fig. 5.26.

Table 5.11: Calculated values for maximum power point, P_{mpp}, fill factor, FF, open circuit voltage, V_{oc} and short circuit current, I_{sc}, for curves in Fig. 5.26.

$\epsilon_r^{inorganic} : \epsilon_r^{organic}$	P_{mpp} / W	FF	V_{oc} / V	I_{sc} / mAcm^{-2}
1 : 1	−38.79	0.379	1.325	−7.706
2 : 1	−37.11	0.256	1.358	−10.679
5 : 1	−44.56	0.279	1.374	−11.621
10 : 1	−47.36	0.295	1.389	−11.538
15 : 1	−47.39	0.298	1.406	−11.322
100 : 1	−47.47	0.319	1.422	−10.471

From Tab. 5.11 it is obvious that the open circuit voltage increases with the ϵ_r ratio while it remains hard to predict the short circuit current. From Sec. 5.1.1.3 we already know that basically the short circuit current decreases, i.e. becomes less negative, with higher ratios due to diffusional processes (Fig. 5.7). However, in Sec. 5.1.1.8 we observed that it increases, i.e. becomes more negative, with rising ϵ_r ratios (Fig. 5.19) due to the excitonic dissociation process. Therefore, it is reasonable to conclude from Tab. 5.11 and Fig. 5.26 that up to an ϵ_r ratio of about 1 : 5 the curves are dominated by the excitonic effect, while for higher ratios the effect of the diffusional process is stronger.

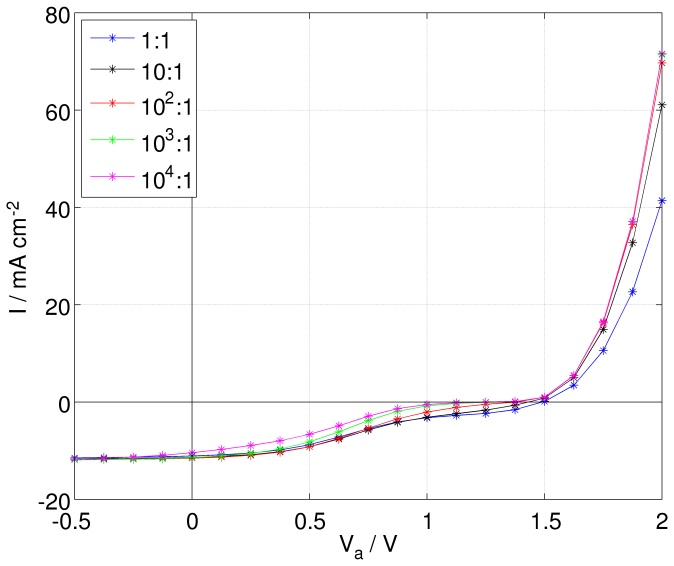

Figure 5.27: I-V characteristic with switch configuration shown in Tab.5.10, for different μ_0 ratios.

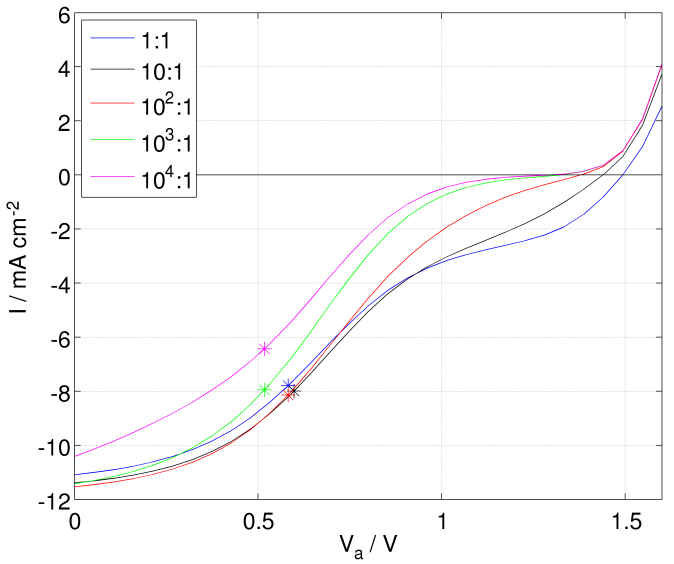

Figure 5.28: I-V characteristic with switch configuration shown in Tab.5.10, for different μ_0 ratios with maximum power points indicated by an asterisk; closer view.

As done already in Sec. 5.1.1.3, we will continue discussing the effect of the mobility change in the inorganic layer, for reasonable ratios, on the I-V curve. Basically, in Fig.

5.27 and Fig. 5.28 we see the same effects as in Fig. 5.8 and Fig. 5.9 combined with the effects already demonstrated for exciton dissociation processes. A remarkable detail is that for $\mu_0^{inorganic} : \mu_0^{organic} = 1 : 1$ the plateau does not correspond to a negligible current. This is due to the mobility effect discussed in Sec. 5.1.1.3, i.e. there is no preferred diffusion direction *a priori*.

Table 5.12: Summary of the calculated values for maximum power point, P_{mpp}, the fill factor, FF, open circuit voltage, V_{oc}, and short circuit current, I_{sc}, for the curves shown in Fig. 5.28.

$\mu_0^{inorganic} : \mu_0^{organic}$	P_{mpp} / W	FF	V_{oc}/ V	I_{sc} / mAcm^{-2}
1 : 1	−45.33	0.272	1.503	−11.091
10 : 1	−47.79	0.188	1.455	−11.396
100 : 1	−47.36	0.295	1.389	−11.538
1000 : 1	−41.13	0.268	1.341	−11.4253
10000 : 1	−33.26	0.244	1.309	−11.414

The open circuit voltages increase with decreasing mobility. However, there is no clear trend in the short circuit current anymore. Therefore, there is also no unambiguous trend in the maximum power points and fill factors, Tab. 5.12, as a function of the mobility in the inorganic layer. This is again due to two different overlapping effects. First, the increase of the absolute short circuit current with increasing mobility due to recombination effects (Sec. 5.1.1.4) and second, the decrease of the absolute short circuit current because of the diffusional effect, discussed in Sec. 5.1.1.3.

5.1.2 Different polymers

In this subsection we will discuss two different calculations for the three different polymers introduced in Sec. 2.3.3, Fig. 2.11. The detailed parameters for these materials are shown in Tab. 4.1. Switch configurations used are as discussed in Sec. 5.1.1.7 and in Sec. 5.1.1.10.

5.1.2.1 Switch setting 7

Table 5.13: Switch setting 7.

switch	status
switchlight	1
switchlambertbeer	1
switchre	1
switchmob	1
switchex	0
switchbraun	0
switchrandom	0

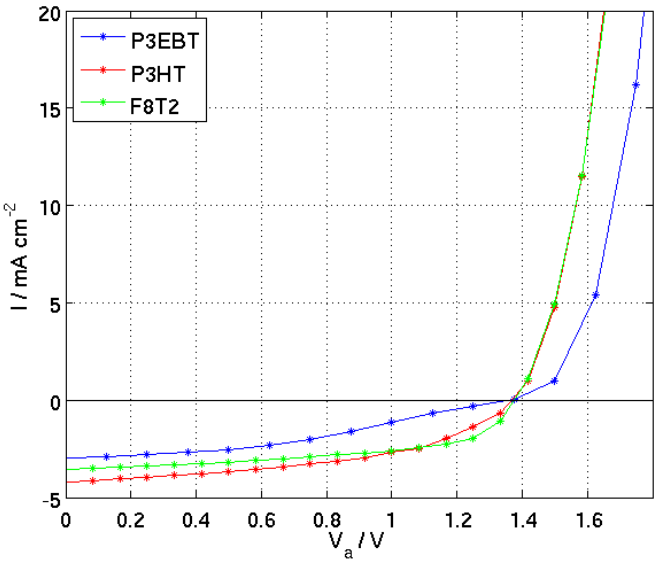

Figure 5.29: I-V characteristic, illuminated case, with switch configuration shown in Tab.5.13 for three different polymers.

The interesting fact, considering these characteristics, is that, although the built-in voltages are not the same for the three different polymers, the open circuit voltage is almost the same for P3HT and F8T2. Thus, the open circuit voltage is not mandatorily almost equal to the built-in voltage. In Tab. 5.14 the built-in voltages, as defined in Fig. 4.2, for the three polymers are summarized.

Table 5.14: Built-in voltages, HOMO and LUMO band off-sets for the P3HT/CIS, P3EBT/CIS and F8T2/CIS systems.

	V_{bi} / eV	ΔE_{HOMO} / eV	ΔE_{LUMO} / eV
P3HT / CIS	1.1	0.4	0.6
P3EBT / CIS	1.5	0.0	0.4
F8T2 / CIS	1.3	0.2	1.6

To comprehend the apparent lack of a systematic offset between V_{bi} and V_{oc}, both the dark (Fig. 5.30) and the illuminated (Fig. 5.29) I-V curve as well as the HOMO/LUMO levels (Tab. 4.1 and Tab. 5.14) require a closer inspection.

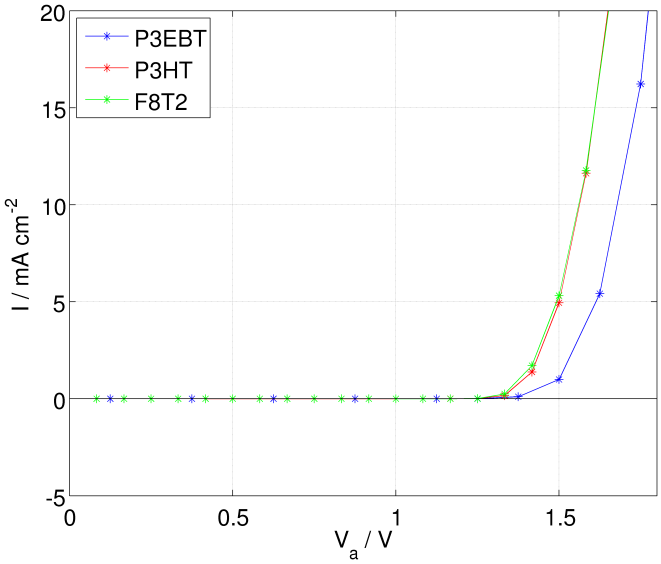

Figure 5.30: I-V characteristic, dark case, with switch configuration shown in Tab.5.13 for three different polymers; dark case.

For the P3EBT / CIS system the open circuit voltage corresponds to the built-in voltage. Actually, the current rises slightly before the built-in voltage due to the diffusion of holes, because of a vanishing HOMO offset between P3EBT and CIS. This effect is also responsible for the plateau discussed in Sec. 5.1.1.3 and was already observed experimentally by Uhrich *et al.* [32]. They measured I-V curves for materials including an energetic barrier for holes in the HOMO level and without this barrier. Uhrich *et al.* detected a plateau in the illuminated curves for vanishing offsets, as predicted by the calculation shown previously (Sec. 5.1.1.3).

For F8T2, the band off-set in the HOMO level is much lower than the one in the LUMO level. In P3HT, the two offsets differ only by 0.2 eV. In all cases, the dark current starts to rise approximately one Volt before the applied voltage is equal to the built-in voltage. For the F8T2 / CIS system it rises shortly before $V_a = 1.4$ V, for P3HT / CIS also shortly before $V_a = 1.4$ V and for P3EBT / CIS shortly after $V_a = 1.4$ V, Fig. 5.30. Thus, the open circuit voltage is approximately equal to the built-in voltage plus the lowest band off-set in the material, because at this point one kind of charge carriers can overcome the barrier.

$$V_{oc} \approx \frac{1}{q} \left[V_{bi} + \min \left(\Delta E_{HOMO}, \Delta E_{LUMO} \right) \right] \tag{5.10}$$

Among the materials chosen in this work, it is always the holes, which can overcome the barrier first. For F8T2 / CIS the band off-set is 0.2 eV and for P3HT it is 0.4 eV, therefore the dark and illuminated I-V curves start to increase at the same voltage although the built-in voltage is not the same. For P3EBT / CIS the HOMO band off-set is 0.0 eV and therefore the built-in voltage more or less equals the open-circuit voltage.

5.1.2.2 Switch setting 10

Table 5.15: Switch setting 10.

switch	status
switchlight	1
switchlambertbeer	1
switchre	1
switchmob	1
switchex	1
switchbraun	1
switchrandom	0

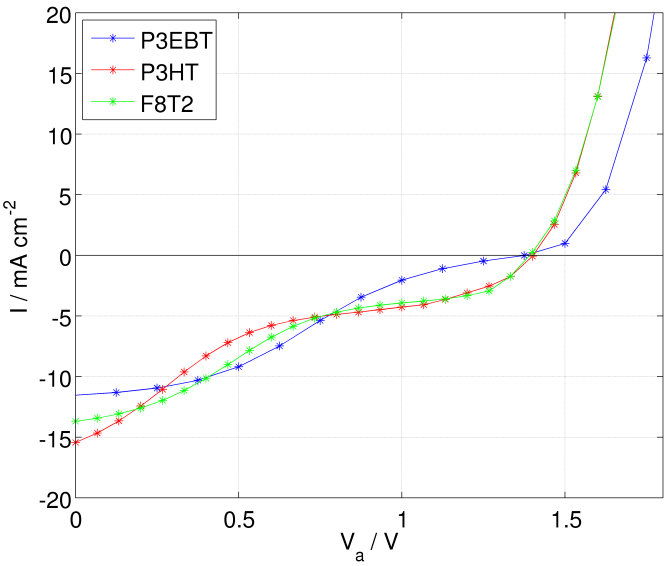

Figure 5.31: I-V characteristic with switch configuration shown in Tab.5.15 for three different polymers.

In Fig. 5.31 one can see the I-V curves for the illuminated case for the three different systems already discussed in the previous subsection but with consideration of exciton motion and field-dependent dissociation rates according to Braun's theory, Eq. (3.42). The interesting fact is that for P3HT / CIS and F8T2 / CIS a current can be observed although the electric field strength reaches a minimum (see Fig. 5.21), while for P3EBT / CIS there is no current. The explanation can be found again in the different HOMO/LUMO off-sets, see Tab. 5.14. For these polymers the HOMO off-set is not zero, thus the holes cannot move freely to the corresponding electrode and there is still a negative current observed. The reason for nearly equivalent open circuit voltages was already discussed in Sec. 5.1.2.1.

5.2 Comb-like interface

In this section we discuss the effects of an interface change, Fig. 5.32, on the generation rates for charge carriers. A detailed study of morphological influences on the I-V characteristic can be found in [2]. Once more, we use the switch settings defined in Sec. 4 as an orientational tool. Also in this section we use the P3EBT / CIS system as the default material configuration. In the third subsection we introduce a new system, i.e. P3HT / PCBM-C61, to study some experimentally obtained photocurrent characteristics.

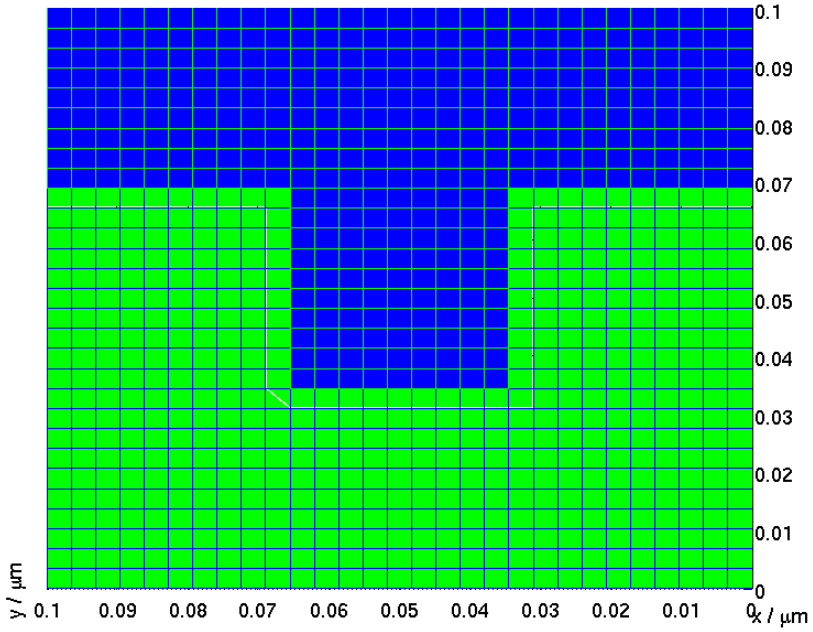

Figure 5.32: Morphology of the active layer for the comb-like interface structure consisting of an acceptor (blue) and a donor (green).

5.2.1 Switch setting 7

Table 5.16: Switch setting 7.

switch	status
switchlight	1
switchlambertbeer	1
switchre	1
switchmob	1
switchex	0
switchbraun	0
switchrandom	0

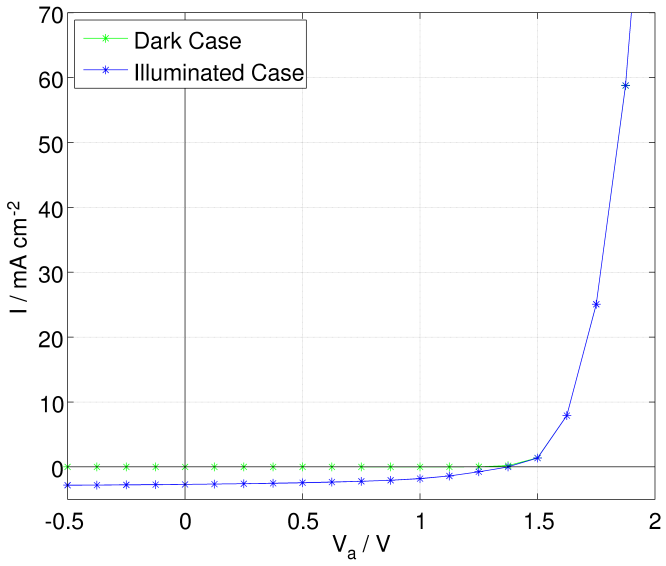

Figure 5.33: I-V characteristic for a comb-like interface structure and switch configuration shown in Tab.5.16. The green curve represents the dark case, i.e. $switchlight = 0$.

Basically, there is not much difference to the I-V curves with a flat interface structure, because the total inorganic area remained the same and we do not have a specific exciton dissociation rate due to the $switchex = 0$ setting. Nevertheless, this example was chosen to study recombination effects. The following three pictures will give an overview on the distribution of potential, electron density, hole density, generation rate and electric field strength at a particular voltage.

Now we will discuss the different profiles given in Fig. 5.34 - 5.36. The electron and hole densities behave perfectly as expected. For a voltage significantly lower than the open circuit voltage (Fig. 5.34), most electrons are in the inorganic region because they cannot move freely due to the LUMO gap between P3EBT and CIS. The holes do not feel a band gap, therefore they are more equally distributed than the electrons. Nevertheless, there are more holes located in the inorganic material because the space charge of the electron attracts them. The higher the applied voltage gets (Fig. 5.35 and Fig. 5.36), the more electrons are attracted by the ITO anode and have the energy to overcome the barrier; thus more electrons can be found in the organic layer. The same holds for holes by neglecting the barrier: the higher the voltage gets the more holes we can find in the inorganic region because they are more attracted to the aluminum cathode. The change of the electric field strength observed from Fig. 5.34 - Fig. 5.36 is due to the potential

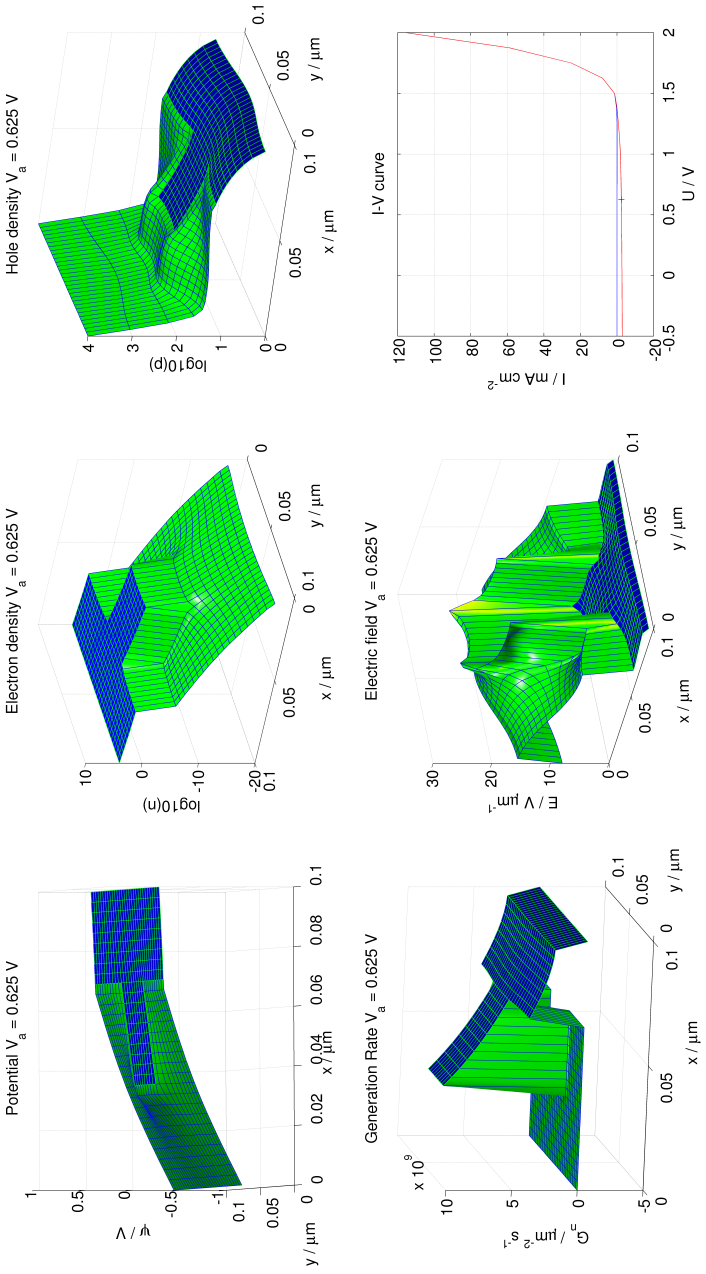

Figure 5.34: Potential, electron density, hole density, generation rate, electric field strength at an applied voltage of $V_a = 0.625$ V indicated in the I-V curve (clockwise).

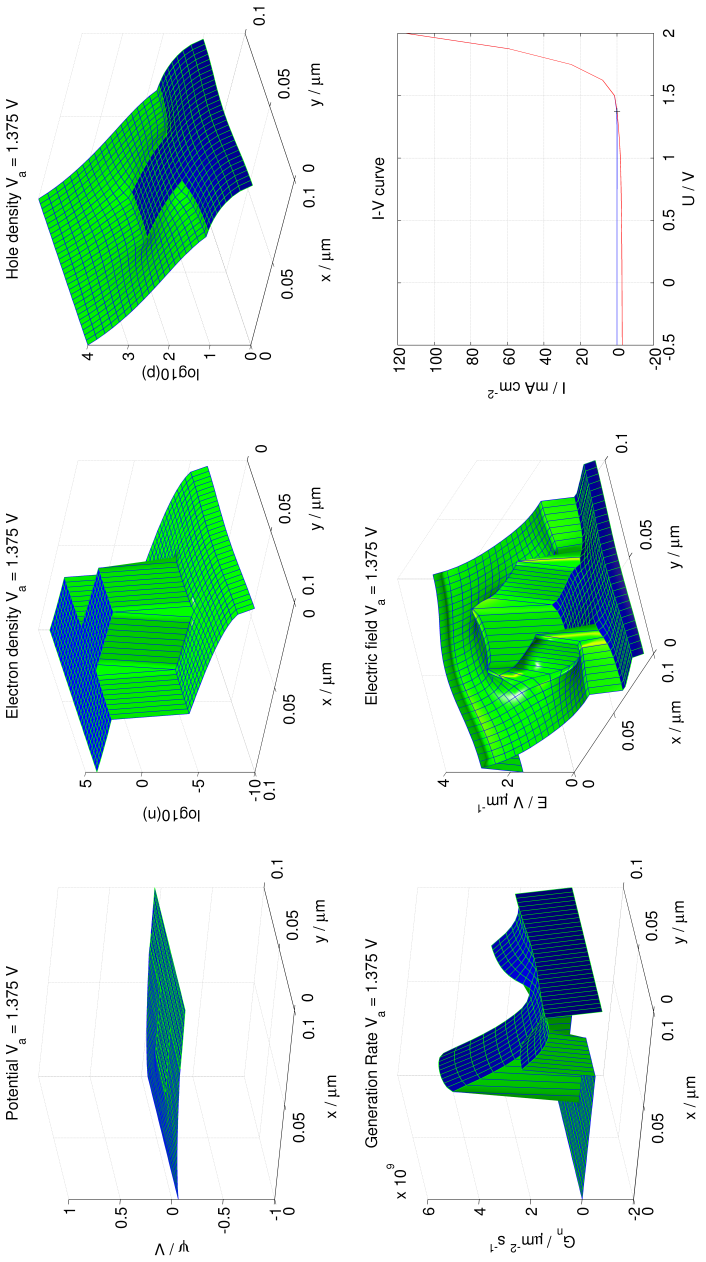

Figure 5.35: Potential, electron density, hole density, generation rate, electric field strength at an applied voltage of $V_a = 1.375$ V indicated in the I-V curve (clockwise).

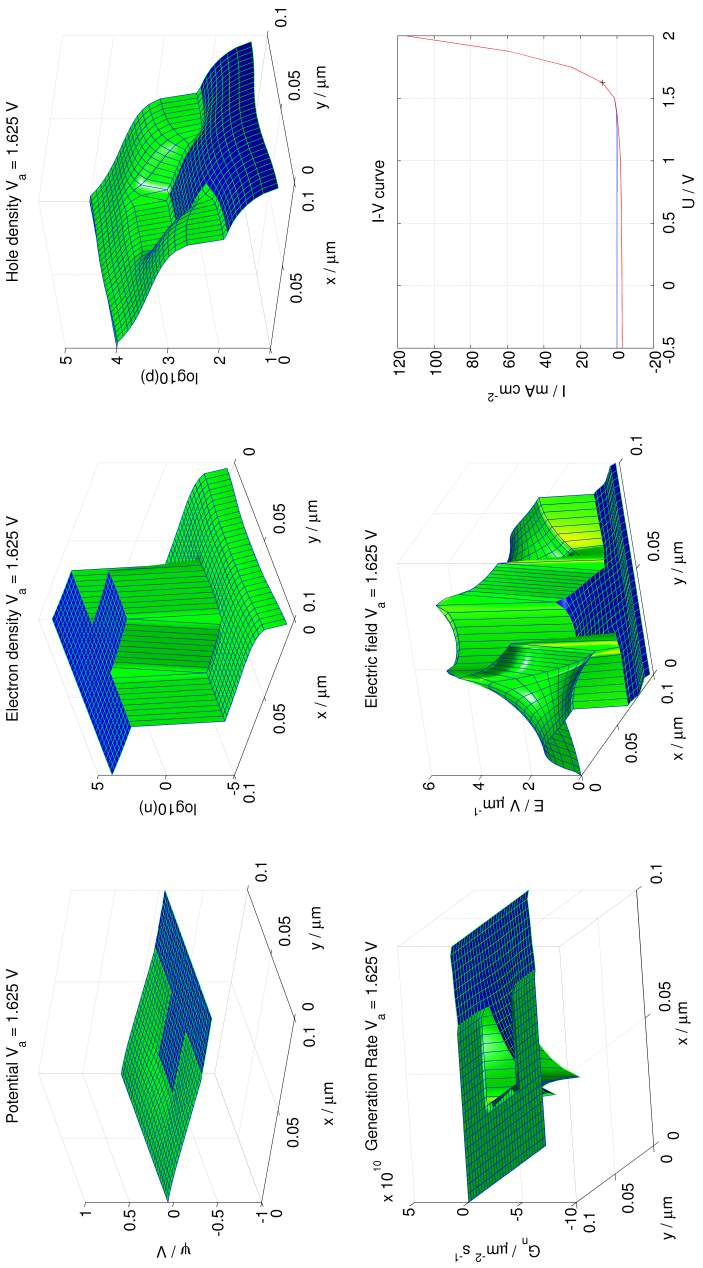

Figure 5.36: Potential, electron density, hole density, generation rate, electric field strength at an applied voltage of $V_a = 1.625$ V indicated in the I-V curve (clockwise).

and charge carrier density change. More interesting is the net generation rate, i.e. Γ_n as defined in Eq. (3.47), see lower left panel in Figs. 5.34 - 5.36. For an applied voltage of $V_a = 0.625$ V, the generation rate is directly related to Lambert-Beer's law, because of the $switchex = 0$ condition. Correspondingly, there are no recombination processes of significant magnitude. By approaching the open circuit voltage, however, we obtain more charge carriers and therefore also the recombination rate increases and deforms the net-generation profile (Fig. 5.35). Finally charge carrier recombination is dominant in comparison to charge carrier generation (Fig. 5.36).

5.2.2 Switch setting 10

Table 5.17: Switch setting 10.

switch	status
switchlight	1
switchlambertbeer	1
switchre	1
switchmob	1
switchex	1
switchbraun	1
switchrandom	0

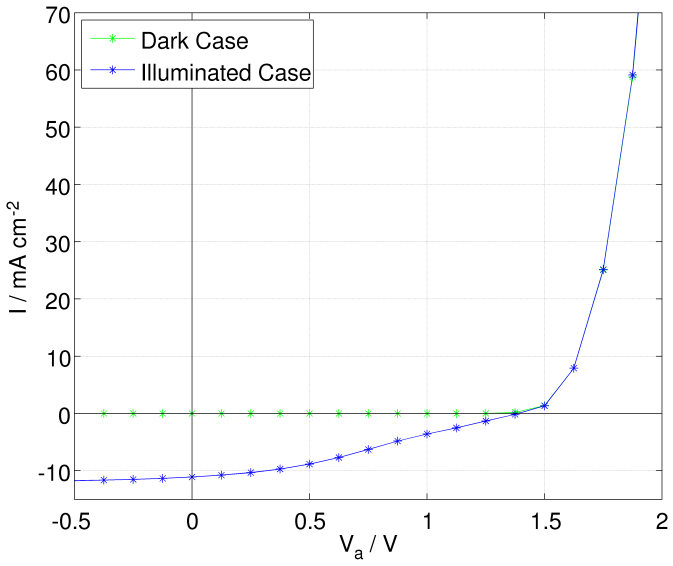

Figure 5.37: I-V characteristic for comb-like interface structure and switch configuration shown in Tab.5.17. The green curve represents the dark case, i.e. $switchlight = 0$.

First of all it has to be mentioned that the difference of the absolute values for the current densities in the negative regime (reverse bias) in comparison to [2] result from the different set of parameters used. Although the HOMO/LUMO levels are set at the same values, there are a couple of assumptions chosen differently, i.e. different mobilities at the contacts, different ϵ_r values and different mobilities for the inorganic region. Furthermore, field-assisted dissociation rates, recombination rates and field-dependent mobilities are considered.

As in the case of the flat interface, it is apparent that at applied voltages in the vicinity of the built-in voltage, i.e. $V_a \approx V_{bi}$, there is a plateau in the I-V characteristic (Fig. 5.37) due to generational and diffusional effects, discussed in previous sections. The interesting details are the investigation of the generation rates in combination with the electric field strength in comparison to the case of a flat hetero-junction. This will be done in detail in Sec. 5.3. At this point we will have a closer view on the coherence of the average netto generation rate, i.e. $\overline{\Gamma}_n = \frac{1}{N} \sum_{i,j} \Gamma^n_{i,j}$ with N denoting the number of grid points, and the I-V curve for the photocurrent, i.e. the difference between illuminated and dark current density, $I_{ph} = I_{ill} - I_{dark}$, Fig. 5.38.

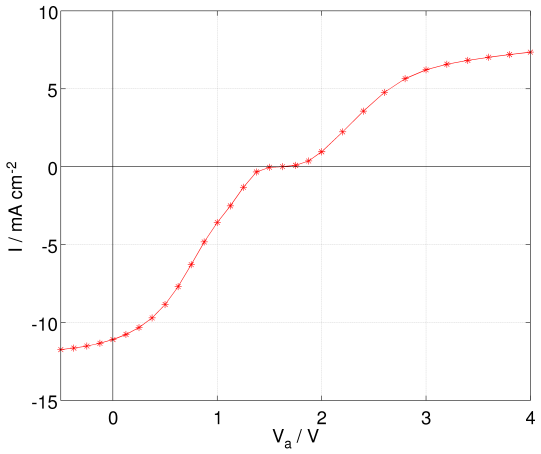

Figure 5.38: Photocurrent for a comb-like interface and switch setting listed in Tab. 5.17.

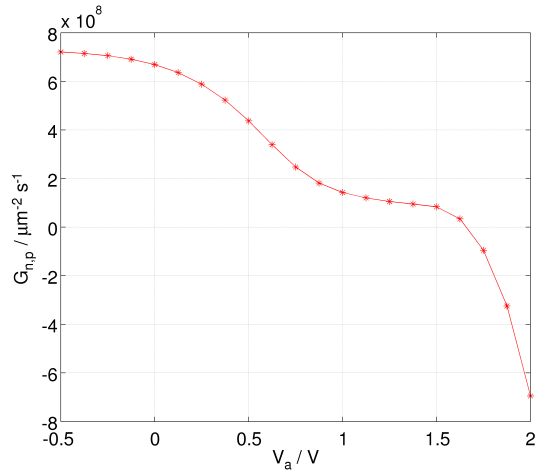

Figure 5.39: Average netto generation rate, $\overline{\Gamma}_n$ for a comb-like interface and switch setting listed in Tab. 5.17.

For negative and positive voltages, the current converges to a constant value. By looking at the generation profile as a function of the applied voltage displayed in Fig. 5.39, one can see that for positive voltages the photo current converges, because the recombination rate dominates the whole generation process. Thus the illuminated current cannot rise faster than the dark current. For the negative regime, the generation reaches a maximum value, thus, there cannot be more current produced by photoinduction. The plateau in the photo current characteristic can be explained by the back diffusion process at the interface and the lower generation rate because of the field-dependence, as already

discussed in Sec. 5.1.

Reducing the plateau to the back diffusion process, i.e. taking the I-V characteristics gained by using the switch-setting of Tab. 5.16 yields the results depicted in Fig. 5.40 and Fig. 5.41.

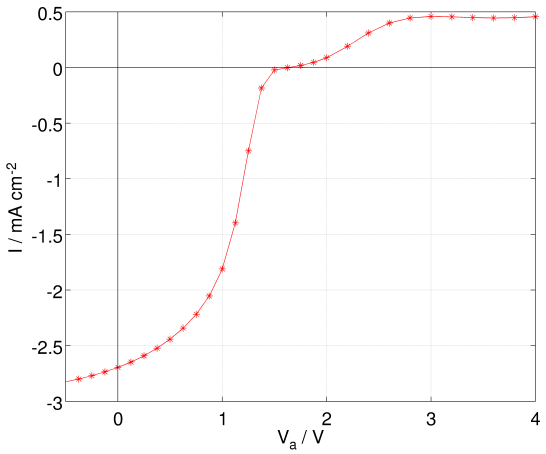

Figure 5.40: Photocurrent for a comb-like interface and switch setting listed in Tab. 5.16.

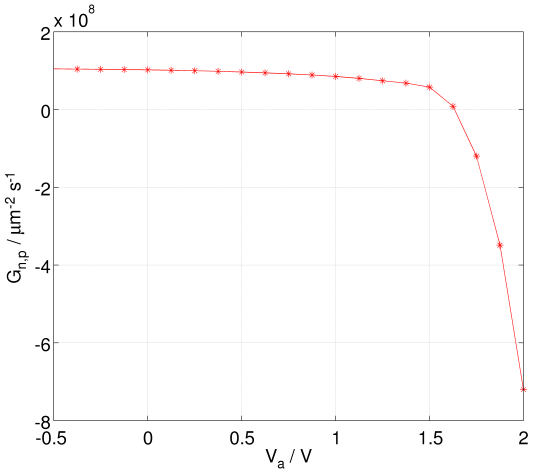

Figure 5.41: Average netto generation rate, $\overline{\Gamma}_n$ for a comb-like interface and switch setting listed in Tab. 5.16.

Comparing the two different theoretically obtained photocurrent characteristics in the Figs. 5.38 and 5.40, i.e. by considering field-assisted exciton dissociation and neglecting it, respectively, could be used as a tool to determine if field-dependent exciton dissocia-

tion rates describe the devices sufficiently well. Of course, it has to be emphasized that results obtained by this procedure have to be treated with exceptional care because, as seen in previous sections, there are a lot of different processes profoundly influencing the shape of the I-V curve, and therefore also the characteristic of the photocurrent.

5.2.3 P3HT / PCBM-C61 solar cell - Flat interface

There are experimentally obtained I-V curves and photocurrent characteristics published by Ooi et al. [34] for the P3HT / PCBM-C61 system, which are assumed to form a planar interface. These curves could already be reproduced by M. Gruber [2]. The author considered a comb-like interface, exciton separation at the interface as well as non-ohmic contacts. In our case, we only consider ohmic contacts and primarily a flat-interface configuration to work out effects solely based on generational processes. Several parameters have to be changed, because we switch from an organic/inorganic system to an organic/organic system. They are used as listed below:

- $\mu_n^A = \mu_n^D = \mu_p^D = \mu_p^A = 10^{-8}\ \mathrm{m^2V^{-1}s^{-1}}$
- PCBM-C61: HOMO/LUMO: -6.10 eV / -3.74 eV
- P3HT: HOMO/LUMO: -5.20 eV / -3.5 eV
- $\epsilon_r^A = \epsilon_r^D = 1$

All additional input parameters are set as in the organic/inorganic solar cell calculations (see Tab. 4.1). In the present case, charge carriers are basically generated only field-dependent, whether in the bulk or at the interface, or by exciton diffusion to the interface.

For the first calculated I-V curve (Fig. 5.42 (a)), field-assisted separation of excitons is not considered, i.e. electrons and holes are only produced at the interface by excitons reaching it within their lifetime. The second curve (Fig. 5.42 (b)) represents the characteristic gained by consideration of field-dependent particle generation. Fig. 5.42 (c) shows the experimentally obtained I-V curve published by Ooi et al., [34].

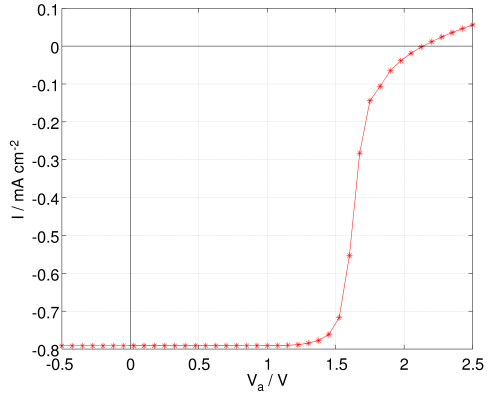

(a) Simulated photocurrent characteristic for the P3HT / PCBM-C61 system by assuming that charge carriers only separate at the interface.

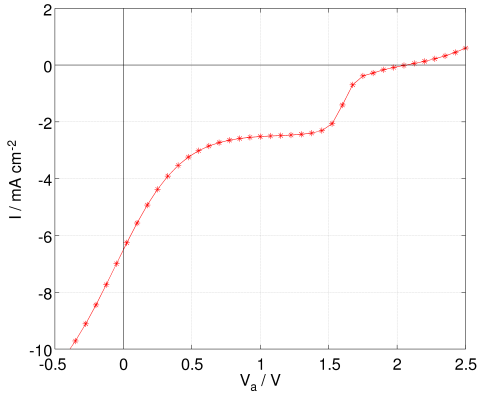

(b) Simulated photocurrent characteristic for the P3HT / PCBM-C61 system by assuming that charge carrier generation is field-dependent.

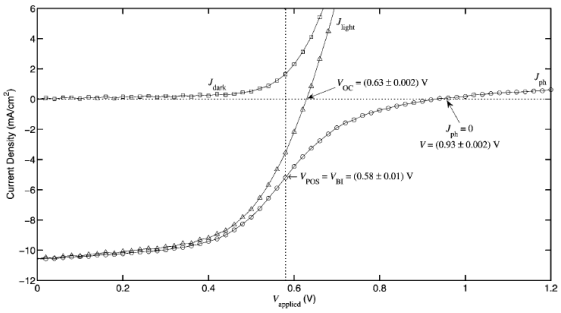

(c) Experimentally obtained I-V curve for P3HT / PCBM-C61 system published by Ooi et al. in [34].

Figure 5.42: Study of different photocurrent characteristics, (a) and (b) were simulated and (c) was experimentally obtained.

As already highlighted, the comparison of experimentally obtained and simulated results has to be treated with exceptional care and without considering non-ohmic contacts. They are responsible for a change of the built-in voltage, which shift the entire characteristic towards lower voltages [2]. However, in the case of Fig. 5.42 there are a couple of remarkable facts which we want to discuss in detail. First, the maximum current observed in the negative regime in Fig. 5.42 (b) is of the same magnitude as the current observed experimentally, Fig. 5.42 (c). In this case almost all excitons dissociate into charge carriers because of the electric field strength induced by the applied voltage. In the case of Fig. 5.42 (a), the current is much lower, because most of the excitons are not able to reach the interface within their lifetime and thus there are fewer charge carriers available for contributing to the current. This indicates that in the experiment almost all

excitons are separated to charge carriers. Nevertheless, it is not clear whether the characteristic plateau in Fig. 5.42 (b) is observed experimentally, because the plotted range around the built-in voltage is not sufficiently large. It could be assumed that there is no plateau because otherwise the absolute value of the current would be lower. Additionally, the experimental current in the positive regime is also in the range of Fig. 5.42 (b) and not in the range of Fig. 5.42 (a). It can be concluded cautiously that in the experiment almost all excitons separate to charge carriers, by comparison with the given current densities in this particular range. Basically there is no significant evidence indicating that charge carrier separation is field-dependent because the separation of excitons can also be tuned by optimizing the interface structure, as shown in [2]. Nevertheless, there is also no evidence indicating that charge carrier separation is not field-dependent at all, because if it is due to the interface no conclusion regarding this point can be made. But it is possible to conclude that charge carrier generation is definitely not dominated by the field-assisted dissociation for a flat interface. Although, interfacial studies can be found in more detail in [2], Fig. 5.43 shows the influence of a comb-like structure on the photocurrent characteristic with consideration of field-assisted dissociation. This additionally substantiates the suspicion that the interface structure of the experimentally measured solar cell is not simply planar.

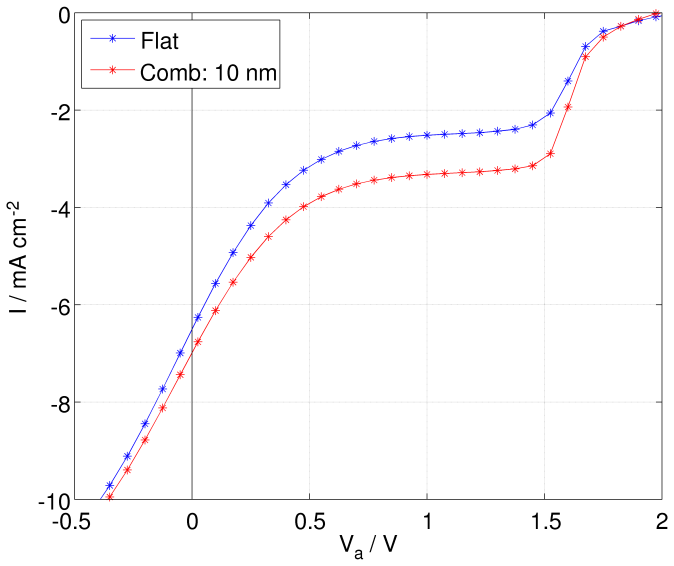

Figure 5.43: Photocurrent characteristic for a P3HT / PCBM-C61 solar cell under consideration of a comb-like structure with a comb-width of 10 nm and field-assisted exciton dissociation rates.

5.3 Generation profiles

In this section we will have a closer look on the generation profiles obtained by the different simulations, for the flat interface as well as for the comb-like structure.

We will begin with generation profiles for the P3EBT/CIS flat system without consideration of field-dependent exciton dissociation to see the impact of recombination effects on a constant generation rate. This was done for field-independent and field-dependent mobilities, because the mobilities influence the recombination rate constant. We will proceed by taking the field-assisted dissociation rate into account and finally conclude by discussing this scenario for a comb-like interface structure. The switch settings once more provide orientation.

5.3.1 Switch Setting 4 - Flat interface

Table 5.18: Switch setting 4.

switch	status
switchlight	1
switchlambertbeer	0
switchre	1
switchmob	0
switchex	0
switchbraun	0
switchrandom	0

These calculations were done with the modified $switchex = 0$ setting as described in Sec. 5.1. At $V_a = -0.5$ V we see a constant generation rate only slightly lowered because of recombination rates, Fig. 5.44 (a). At higher voltages, i.e. $V_a = 1.25$ V, recombination is the dominating process. The generation rate is still large at the interface because there are almost no charge carriers. They move into the inorganic region as soon as they come close to it because of the diffusional effect. Furthermore, it can be seen that the recombination rate is higher in the inorganic region due to higher mobilities, Fig. 5.44 (b). In the positive regime, the recombination dominates the inorganic layer because electrons are collected at the interface and generated holes have to pass the interface on their way to the electrode, Fig. 5.44 (c).

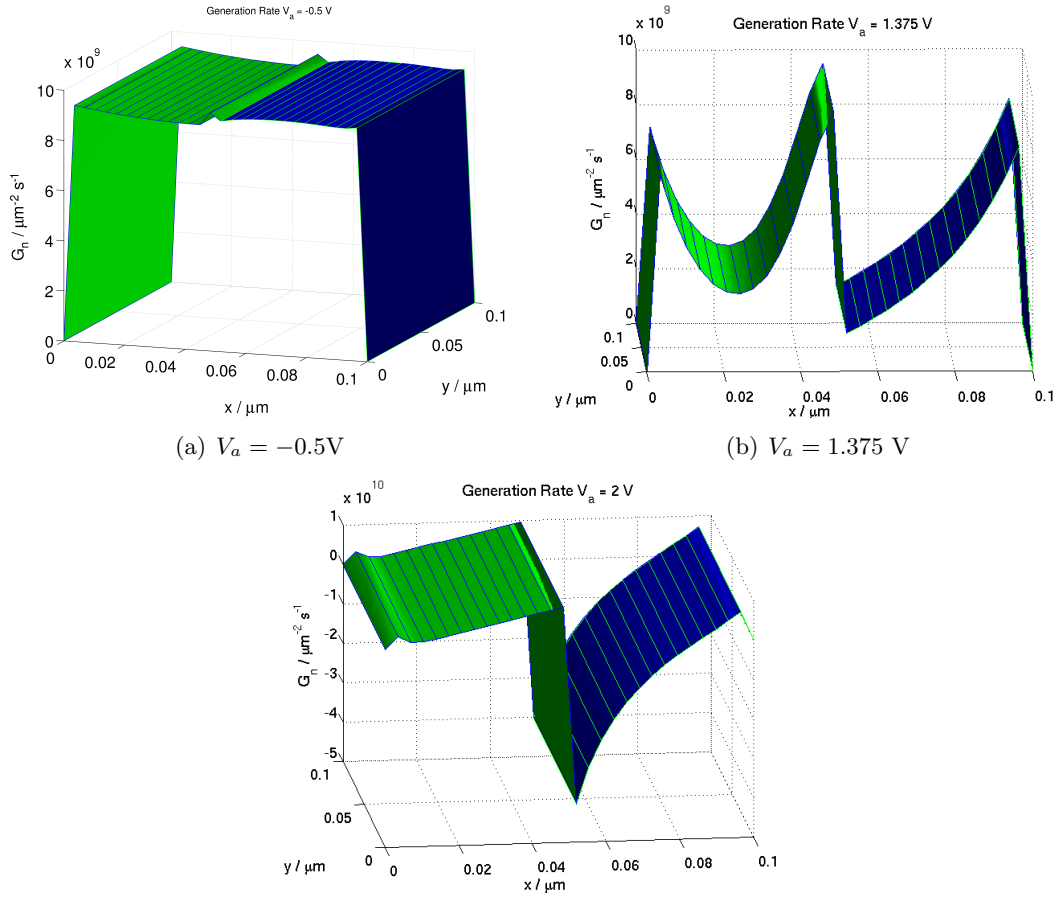

(a) $V_a = -0.5$V

(b) $V_a = 1.375$ V

(c) $V_a = 2.0$ V

Figure 5.44: Generation profiles at different applied voltages for the switch setting listed in Tab. 5.4 and modified *switchex* = 0 condition, Sec. 5.1.1.2.

5.3.2 Switch setting 7 - Flat interface

Table 5.19: Switch setting 7.

switch	status
switchlight	1
switchlambertbeer	1
switchre	1
switchmob	1
switchex	0
switchbraun	0
switchrandom	0

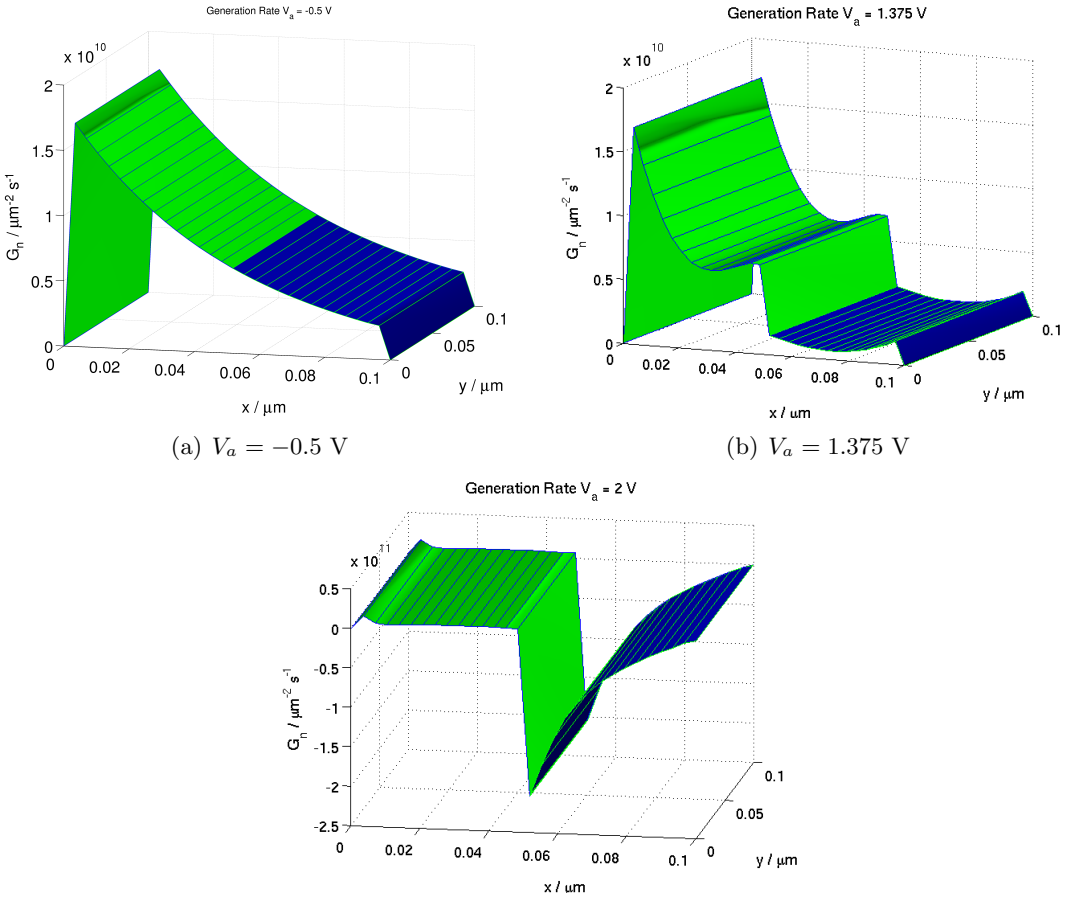

(a) $V_a = -0.5$ V

(b) $V_a = 1.375$ V

(c) $V_a = 2.0$ V

Figure 5.45: Generation profiles at different applied voltages for the switch setting listed in Tab. 5.7 and modified $switchex = 0$ condition, Sec. 5.1.1.2.

The basic features in these generation profiles were already discussed in the section before. Again we discuss three different voltage points. In the first figure, Fig. 5.45 (a) the generation rate is dominated by Lambert Beer's law and almost not influenced by the recombination rate. In the second diagram, Fig. 5.45 (b), recombination effects are responsible for negligible generation of particles in the inorganic layer. Again it is slightly higher at the interface than in the adjacent bulk. At high positive voltages, Fig. 5.45 (c), the generation of particles is almost zero over the device. At the interface in the inorganic region it is even negative, for the same reasons as discussed in the previous section.

5.3.3 Switch setting 9 - Flat interface

Table 5.20: Switch setting 9.

switch	status
switchlight	1
switchlambertbeer	0
switchre	0
switchmob	0
switchex	1
switchbraun	1
switchrandom	0

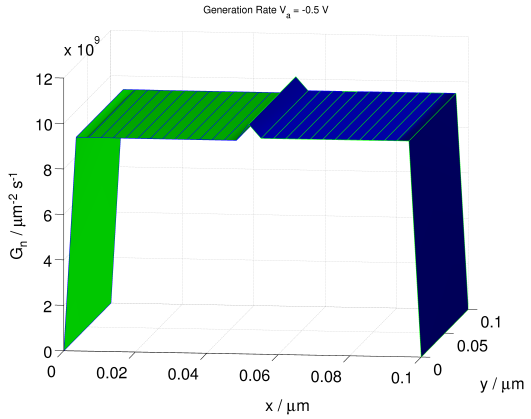

(a) $V_a = -0.5$ V

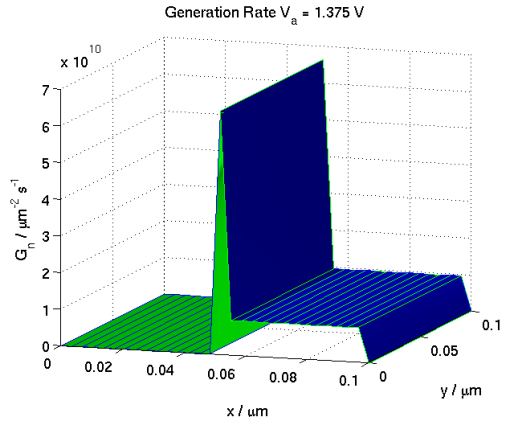

(b) $V_a = 1.375$ V

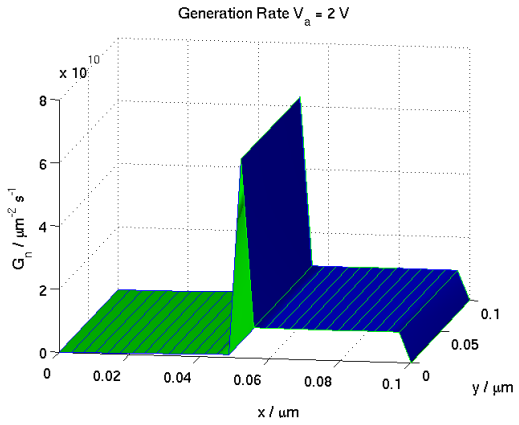

(c) $V_a = 2.0$ V

Figure 5.46: Generation profiles at different applied voltages for the switch setting listed in Tab. 5.9.

In this scenario, we considered field-assisted exciton dissociation according to Braun's model. Furthermore, excitons reaching the organic-inorganic interface separate immediately and light absorbed in the inorganic part also generates electrons and holes directly. However, we still exclude recombination effects to keep the interpretation simple. In the first image we see that the field strength associated to an applied voltage of $V_a = 0.5$ V is sufficiently high to separate almost all excitons in the organic material directly to electrons and holes (Lambert Beer's law is not considered in this particular study). Those excitons which are still intact and reach the interface within their lifetime, separate there, Fig. 5.46 (a). At higher voltages, the field strength is not large enough to separate excitons in the organic layer. Thus, almost all separation takes place at the interface, Fig. 5.46 (b) and (c), as already supposed in Sec. 5.1.1.8.

5.3.4 Switch setting 10 - Flat interface

Table 5.21: Switch setting 10.

switch	status
switchlight	1
switchlambertbeer	1
switchre	1
switchmob	1
switchex	1
switchbraun	1
switchrandom	0

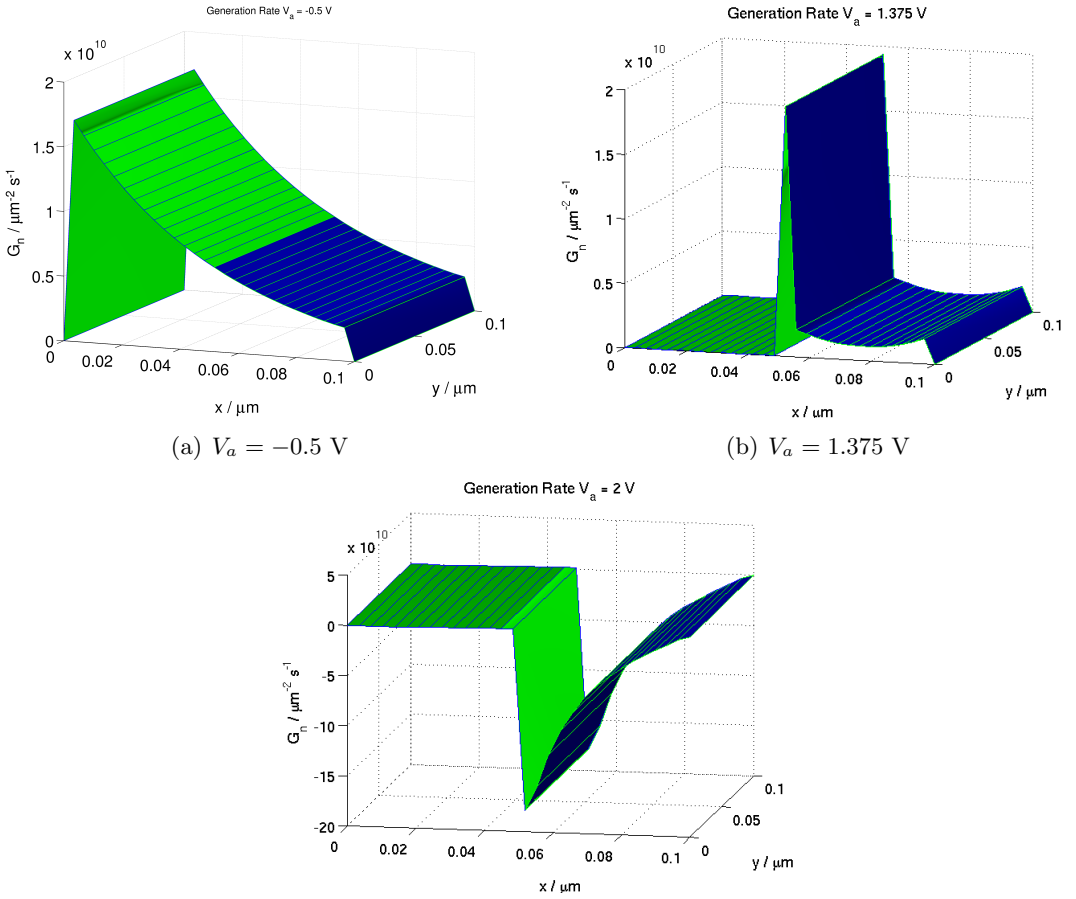

(a) $V_a = -0.5$ V

(b) $V_a = 1.375$ V

(c) $V_a = 2.0$ V

Figure 5.47: Generation profiles at different applied voltages for the switch setting listed in Tab. 5.10.

Considering field-assisted dissociation into charge carriers, bimolecular recombination, field-dependent mobilities and immediate generation of charge carriers in the inorganic layer gives generation profiles exactly as predicted by a combination of the different cases discussed above. At low voltages the field strength is sufficiently high to separate almost all excitons. Approaching the open-circuit voltages yields a generation profile dominated by separation at the interface, while generation in the inorganic layer is lowered by recombination effects. At high voltages the recombination at the interface yields the dominating contribution, Fig. 5.47.

5.3.5 Switch setting 10 - Comb-like interface

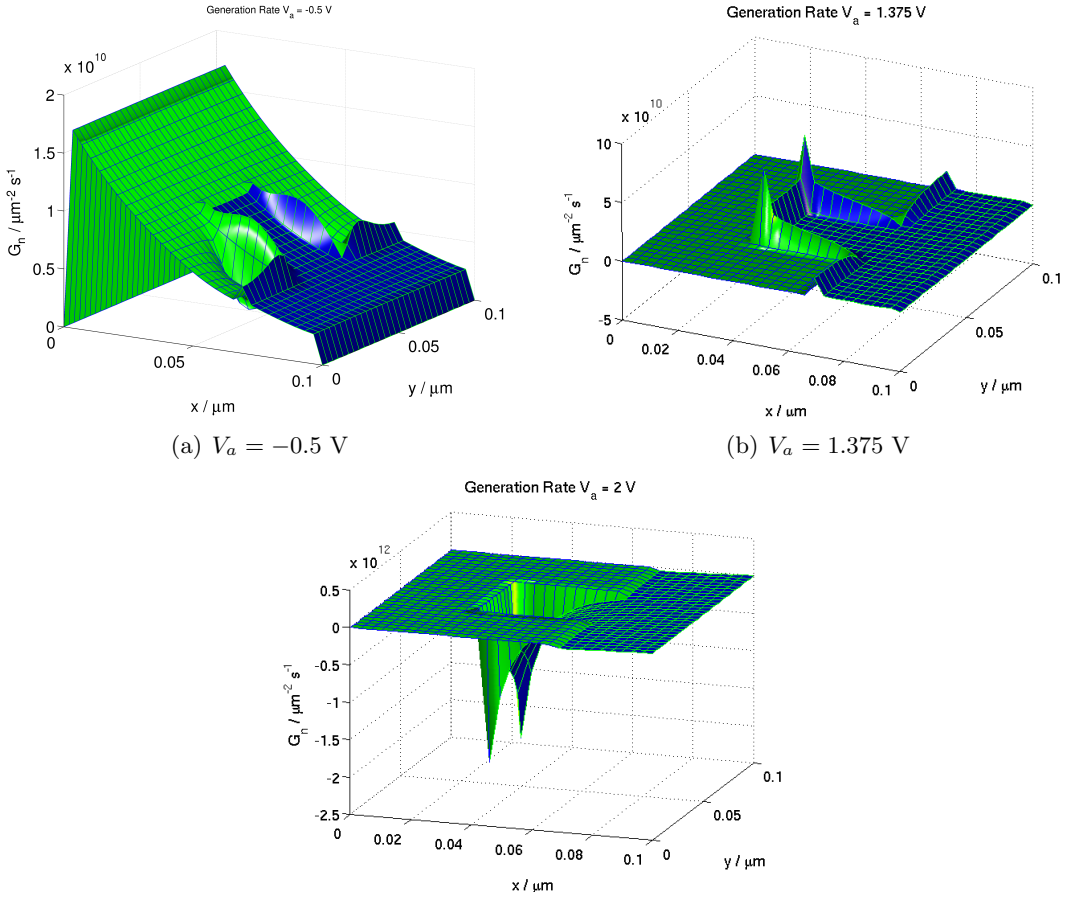

(a) $V_a = -0.5$ V (b) $V_a = 1.375$ V

(c) $V_a = 2.0$ V

Figure 5.48: Generation profiles at different applied voltages for the switch setting listed in Tab. 5.10.

A comb-like interface structure changes the generation profile significantly. At an applied voltage of $V_a = -0.5$ V most excitons are separated field-assisted. But because of locally occurring field strengths and recombination effects, there are excitons left near the interface, Fig. 5.48 (a). The excitons left can diffuse to the interface and dissociate there immediately. At higher voltages, there is almost no field-assisted dissociation seen, except at the points of the comb-like structure where $|\mathbf{E}|$ is still very large. The other charge carriers generated at the interface are due to exciton diffusion. As seen in the previous sections, at an applied voltage of $V_a = 2$ V recombination effects dominate the source-drain term. Again, most charge carriers recombine at the points of the comb

because most particles are generated there and there too the mobilities are very large (field-dependence).Therefore, the recombination rate constant is also very large.

6 Conclusion

The aim of the thesis was to simulate and investigate the influence of exciton generation and charge carrier recombination effects on the I-V characteristics of hetero-junction photovoltaic devices. To achieve this goal, a program to simulate organic-inorganic solar cells by using a two-dimensional drift-diffusion transport model was developed. The model equations are based on field-assisted dissociation rates, Langevin- and Koster-type recombination rates as well as field-dependent mobilities of the Poole-Frenkel form. The main conclusion of this work is that, although it is still not clear whether excitons dissociate field-dependently or not, there are several characteristic features in I-V curves that have been identified and shown to arise from this property. It is expected that these features will be able to be observed experimentally in the future.

7 Acknowledgments

I would like to acknowledge and express my gratitude to my advisors Ao. Univ.-Prof. DI Dr. Ferdinand Schürrer, Dipl.-Phys. Dr.rer.nat. Karin Zojer and Univ.-Doz. DI Dr. Gregor Trimmel. Without their supervision, advice and support this work would never have been completed. Furthermore I would like to thank the *'Christian Doppler Pilotlabor für Nanokomposit-Solarzellen'* and the *'Ferderal Ministry of Economy, Family and Youth'* for the financial support and the whole group of Ao. Prof. F. Schürrer and Univ.-Doz. G. Trimmel for the helpful suggestions. Especially I want to thank my simulation partner Manni for the important and also funny and relaxing discussions during the work.

Moreover, I want to thank my whole family for their support during my studies. Finally, I want to thank all my friends for the great time we spent together. You know who you are! Last but not least: a big thank you to all the guys from the *'Bügelbrett-Stammtisch'*. Bügeln forever!

Bibliography

[1] Reyes-Reyes M., Kim K., Carroll D.L., *Appl. Phys. Let.*, **87**, 2005, 083506

[2] Gruber M., Diploma Thesis: *Investigation of Morphology Effects on the Performance of Organic Solar Cells and Hybrid Cells by Two-Dimensional Drift-Diffusion Simulations*, TU Graz, 2009

[3] Rath T., PhD Thesis: *Synthesis and Characterization of Nanocrystalline Semiconductiong Materials for Nanocomposite Solar Cells*, TU Graz, 2008

[4] Buxton G.A., Clarke N., *Modelling Simul. Mater. Sci. Eng.*, **5**, 2007, 13-26

[5] Koster L.J.A., PhD thesis: *Device physics of donor/acceptor-blend solar cells*, 2007, University of Groningen, The Netherlands

[6] Braun C.L., *J. Chem. Phys.*, **80**, 1984, 4157-4161

[7] Onsager L., *J. Chem. Phys.* **2**, 1934, 599-615

[8] Gregg B.A., Hanna M.C. *J. Appl. Phys*, **93**, 2003, 3605-3614

[9] Soga T. (editor). *Nanostructured Materials for Solar Energy Conversion*, Elsevier, Amsterdam, The Netherlands, 2006

[10] Tang C.W., *Appl. Phys. Lett.*, **48**, 1986, 183

[11] Kallmann H., Pope M., *J. Chem. Phys.*, **30**, 1959, 585

[12] Sze S.M.,*Semiconductor Physics - Physics and Technology*, Wiley & Sons Inc., Hoboken, New Jersey, 2002

[13] wikipedia, *http://en.wikipedia.org/*

[14] *http://rredc.nrel.gov/solar/spectra/am1.5/*

[15] Dierschke F., Grimsdale A.C., MÃ$\frac{1}{4}$llen K., *Macromol. Chem. Phys.*, **205**, 2004, 1147-1154

[16] Babel A., Jenekhe S.A., *J. Am. Chem. Soc.*, **125**, 2003, 13656-13657

[17] Schwoerer M., Wolf H.C., *Organic Molecular Solids*, Wiley-VCH, Weinheim, 2007

[18] Chaing C.K.,Fincher jr.C.R.,Park Y.W.,Heeger A.J., Shirakawa H., Louis E.J., Gau S.C., MacDiarmid A.G., *Phys. Rev. Lett.*, **39**, 1977, 1098

[19] Brabec C.J., Sariciftci N.S., Hummelen J.C., *Adv. Funct. Mater.*, **11**, 2001, 15-26

[20] Rupprecht L., *Conductive Polymers and Plastics in Industrial Applications*, Plastic Design Library, Norwich, New York, 1999

[21] Little W.A., *Phys. Rev. A*, **6**, 1964, 1416-1424

[22] Trimmel G., Institute of Chemical Technology of Materials, TU Graz, private communications

[23] Karlin S., *A first Course in Stochastic Processes*, Academic Press, New York, New York, 1966

[24] Assadi A., Svensson C., Wilander M., Inganas O., *Appl. Phys. Lett.*, **53**, 1988, 195-198

[25] Bässler H., *Phys. Stat. Sol. B*,**175**, 1993, 15-56

[26] Seki K., Tachiya M., *Phys. Rev. B*, **65**, 2001, 014305

[27] Nelson E., *Dynamical Theories of Brownian Motion*, Mathematical Notes, Princeton University Press, Princeton, New Jersey, 1967

[28] Jordan P.C., *Chemical Kinetics and Transport*, Plenum Press, New York, 1981

[29] Possanner S., Diploma Thesis: *Drift-Diffusion Simulations of Charge Transport in Organic Field-effect Transistors*, TU Graz, 2008

[30] Abramowitz M., Stegun I.A., *Handbook of Mathematical Formulas*, Dover Publications, New York, 1964

[31] Scharfetter D.L., Gummel H.K., *IEEE-Trans. Elec. Dev.*, **16/1** (1969), 64-77

[32] Uhrich C., et al., *J. Appl. Phys.*, **104**, 2008, 043107

[33] Deibel C., Wagenpfahl A, Dyakonov V., *Phys. Stat. Sol. (RRL)*, **2**, 2008, 175-177

[34] Ooi Z.E., et al., *J. Mat. Chem.*, **18**, 2007, 1644-1651